EXPERIMENTAL IMPLEMENTATION OF A NEW DURABILITY / ACCELERATED LIFE TESTING TIME REDUCTION METHOD

by

IGOR BASESKI

A dissertation submitted in partial fulfillment of the
requirements for the degree of

DOCTOR OF PHILOSOPHY IN MECHANICAL ENGINEERING

2021

Oakland University
Rochester, Michigan

Doctoral Advisory Committee:

Zissimos P. Mourelatos, Ph.D., Chair
Michael Latcha, Ph.D.
Dorin Drignei, Ph.D.
Xia Wang, Ph.D.

*To all of my family, friends and co-workers who have supported me along this journey,*

*and to God for giving me the blessing and opportunity to finish.*

*To my wife Ellie, for her inspiration as a dedicated and passionate supporter*

## ACKNOWLEDGMENTS

First and foremost, I would like to express my sincere gratitude to my adviser, Dr. Zissimos P. Mourelatos for his dedication and guidance since I began pursuing my Master's Degree. His passion for his work, dedication to his students, integrity, wisdom and work ethic have been a significant source of inspiration during these years of research at OU.

I would also like to thank all the members of my committee, Dr. Michael Latcha, Dr. Dorin Drignei, and Dr. Xia Wang for their suggestions and feedback, as well as for the help they provided whenever needed.

Special thanks to my co-workers at Ground Vehicle System Center (GVSC) whose collaboration and hard work have introduced me to new ideas, insights and opportunities.

Igor Baseski

ABSTRACT

EXPERIMENTAL IMPLEMENTATION OF A NEW DURABILITY / ACCELERATED LIFE TESTING TIME REDUCTION METHOD

by

Igor Baseski

Adviser: Zissimos P. Mourelatos, Ph.D.

Fatigue can be defined as a cyclic degradation process resulting in a failure at lower stress levels than the ultimate load. Fatigue reliability is defined as the probability that a structure will perform its intended function throughout its lifetime without any fatigue failure. Durability testing aims to predict fatigue damage in order to estimate the remaining useful life (RUL) based on fatigue. The latter is a useful metric in design for life-cycle cost. The objective of this research is to develop a new durability time reduction method to experimentally estimate the fatigue life of a vehicle component or system with accuracy using a short duration test.

We assume that the loading random process (e.g. terrain configuration) is stationary and ergodic so that a single time trajectory can quantify the loading statistics. For the single time trajectory of the load process, we measure the corresponding output stress trajectory at a specified location on the structure. The latter is cycle counted using the 4-point rainflow counting algorithm. The cycle counting identifies all signal (stress) peaks and valleys using a peak picking algorithm and uses them to identify the range of all individual fatigue damage cycles and the time they occur based on a chosen fatigue

damage model. Using this information (range of each cycle and the time it occurs), we build a synthetic signal exhibiting the same fatigue damage cycles in the sequence they occur in the actual stress signal. The sequence can be important in order to properly account for the cumulative damage accumulation. Finally, based on the fact that the cycle damage is independent of the time it occurs, we compress the synthetic signal so that its Power Spectral Density (PSD) does not exceed an upper limit dictated by the durability equipment. This proposed durability approach achieves therefore, the same cumulative damage with the original signal in a much shorter testing time. We demonstrate the new durability approach with two examples, and validate it experimentally using a commonly used Belgian block terrain excitation on the suspension coil spring of a military HMMWV (High Mobility Multi-purpose Wheeled Vehicle).

TABLE OF CONTENTS

TABLE OF CONTENTS—Continued



x

TABLE OF CONTENTS—Continued

LIST OF TABLES

LIST OF FIGURES

LIST OF ABBREVIATIONS

| | |
|---|---|
| PSD | Power Spectral Density |
| MCS | Monte Carlo Simulation |
| ATC | Aberdeen Test Center |
| DFD | Drive File Development |
| DT | Developmental Test |
| GSL | Generic Stress Life |
| OT | Operational Test |
| PM | Program Manager |
| RLDA | Road Load Data Acquisition |
| RPC | Remote Parameter Control® |
| T&E | Test and Evaluation |
| VDS | Vehicle Durability Simulator |
| $\alpha$ | Current crack length |
| $a_f$ | Final crack length at failure |
| $n_i$ | Number of cycles per stress level i |
| $s_i$ | Stress level |
| $N_{f,i}$ | Number of cycles the specimen will fail under stress Si |
| $D$ | Cumulative damage |
| $\nu_0$ | Mean up-crossing rate |

| | |
|---|---|
| $A$ | Coefficient from the S-N curve |
| $m$ | Fatigue strength coefficient |
| $\sigma_x^2$ | Variance of the underlying Gaussian process |
| $\alpha$ | Irregularity factor |
| $R(T)$ | Fatigue reliability |
| $T_L$ | Fatigue life |
| DOF | Degree of freedom |
| FRF | Frequency response function |
| $H(\omega)$ | Frequency response function |
| $\omega_n$ | Natural frequency |
| $S_m$ | Mean stress |
| $S_a$ | Stress amplitude |
| $d$ | Wire diameter |
| $C$ | Spring index |
| $\tau$ | Shear stress |
| $D$ | Coil diameter |
| $v$ | Vehicle speed |

# CHAPTER ONE

# INTRODUCTION

To meet increasing competition, reduce the cost of testing, get products to market in the shortest possible time, and satisfy demanding customer expectations, industry is turning to sophisticated methods and techniques of testing. Many of today's products are capable of operating under extremes of environmental stress and for thousands of hours without failure. Traditional test methods are no longer sufficient to identify design weaknesses or validate life predictions.

Accelerated testing and durability testing are approaches for obtaining more information from a given test time than would normally be possible. There are many ways to perform accelerated or durability testing. One of them is by using a test environment that is more severe than that experienced during normal equipment use. Since higher stresses are used, accelerated/durability testing must be approached with caution to avoid introducing failure modes that will not be encountered in normal use. Accelerating factors used, either individually or in combination, include more frequent power cycling, higher vibration levels, high humidity, severe temperature cycling, or higher temperatures.

A different approach to perform accelerated or durability testing is to use computer simulation to obtain all necessary information for increasing our confidence that the product will be reliable as simulated/tested.

The differences between these two approaches are significant and include the underlying assumptions upon which the test is based, the models utilized in constructing the test, the test equipment and chambers used the way in which the test itself is conducted, and the manner in which the resulting data is analyzed and interpreted.

The experimental estimation of reliability which the accelerated life testing approach provides, is extremely difficult due limited obtainable resources to perform a lot of tests, limited existing field data, and required long-duration data to capture performance degradation through the vehicle's lifecycle. Using simulations instead of tests, is usually not practical because of the required high fidelity of predictions.

Engineering components are often subjected to complicated states of stress and strain in which the three principal stresses are non-proportional or their directions change during a loading cycle. These conditions very often occur at geometric discontinuities such as notches or joint connections. In addition, the loading applied to the component may be of varying amplitude. Fatigue under these conditions, termed variable amplitude multiaxial fatigue, is an important design consideration for reliable operation and optimization of engineering components and structures.

This Chapter presents a brief introduction of the importance of fatigue life analysis in engineering and provides a brief history leading to today's diversification of many theories on fatigue of metals. The Chapter also highlights improvements to some of the most important sources of uncertainty in fatigue forecasting, related to the quality and selection of fatigue damage models and to forecasting of fatigue failure.

## 1.1 The Need to Forecast Fatigue Life

Early documented fatigue studies were in support of commercial activities such as mining, steel-work or transportation - steam ships, trains and horse coaches. The dominant objective was robust engineering to avoid catastrophic accidents with loss of life. Today, the objective is similar. It just increases many-folds the need for robust and reliable design to respond to increased economic interests in mobility, production, consumption, or preservation of resources. For example, Ref. [1] provides a collection of over 125,000 engineering materials in its database. At the same time, transport by vehicle in U.S.A., as reported by the U.S. Department of Transportation for 2016 [2] was 6.2 billion air miles and 3,174 billion highway miles. Based on these numbers, it is easy to understand that the engineering effort to achieve both safety and optimality is tremendous. Under-design results in static or fatigue failure and can have major implications, from worst cases involving loss of human life, to lesser effects where failure of mass-produced components results in loss of reputation and business activity. On the other hand, over-design can be significantly damaging if it results in, for example, non-competitive products or overuse of resources. An optimally performing product must be sufficiently robust to never experience unexpected failures, and reliable in order to maintain functionality at all times. Optimality goals must be achieved with inexpensive designs with accounting for variability in materials, manufacturing and functionality. Durability in engineering, specifically for fatigue performance, has never been an easy task.

Despite progress in material development, production, testing, metrology and computational abilities, the study of fatigue does not yet have a simple solution to align the physical phenomena of material failure under cyclic loading to the fundamental laws of physics. In practice, the complexity of the fatigue problem remains overwhelming without an easy solution using a simple set of rules or procedures. As described next, the historical account of the evolution of fatigue in engineering is only an attempt to highlight some among many pivotal moments and researchers from a massive body of literature. Most of the cited works still influence current research.

Ever since the works in [3-6] established fatigue of materials as a formal engineering problem, the scientific community showed an intense interest in improving fatigue forecasting. Interestingly, the most current research in fatigue is not far from the problems formulated and studied by early pioneers in the field. Woler [7], well known for the development of S-N curves, as noted in [8], can also be credited to have implicitly introduced the concept of scatter. Palmgren [9], a well-known researcher on linear and nonlinear damage accumulation, presented the use of fatigue reliability when specifying a B10-fatigue life. Basquin [10], introduced the log-log regression for the S-N curve and offered a method to numerically quantify fatigue properties in terms of an exponential equation coefficient and exponent. By the beginning of the XIX century fatigue was established as a scientific study with options to account for material cyclic properties and to calculate some reliability features.

The next step in the evolution of fatigue of metals, extending to today's research, can be attributed to associating metallurgical and fatigue observations. Ewing and Humfrey [11] described the slip band phenomenon in fatigue-damage evolution. Polanyi [12] followed by Orowan [13] introduced the microstructural dislocation theories. Concurrently, few important concepts are dominant in the literature such as the notch effect [14], damage accumulation [9, 15-17], cycle counting [18, 19], statistical scatter of the cyclic-strength of materials [20] and variable amplitude loading conditions [21].

For these new-at-the-time theories, the hypothesis of cyclically-loaded metal plasticity becomes a formal subject. In 1962, the fundamental work of Tavernelli and

Coffin [22], and Manson [23], introduced the log-log regression model relating fatigue life to plastic strain where plastic deformation was hypothesized to be responsible for fatigue damage. This was a trend-defining work in fatigue analysis since it spurred research attempting to unify the fatigue phenomena and scientific observations providing therefore, the foundation to stress-strain modeling accounting for plasticity in fatigue life. Neuber [24,] Topper [25], followed by Molsky-Glinka [26], and the energy density model of Smith, Watson and Topper [27] for example, provided the foundation to energy models such as the energy model in [28], and the definition of damage type as a function of damage fraction [29, 30]).

Indeed, the science of metals fatigue spans over 180 years of research and many of the theories proposed along the way are actively implemented in engineering calculations of fatigue life.

## 1.2 Uncertainty Sources in Fatigue Damage Modeling

The forecasting of fatigue life is distinctively influenced by the quality of inputs. Commonly in discussing fatigue modeling and the various inputs to a fatigue non-linear system (Figure 1.1), it is assumed that the fatigue life forecasting is strictly subject to uncertainty from the stochasticity of the input variables and processes. It must also be acknowledged that the fatigue nonlinear system is a choice among a set of fatigue rules and models whose selection depends on how the engineer attempts to fit his/her best theoretical knowledge and past experiences.

Given the theory-crowded field of fatigue with many models attempting to define a given fatigue phenomenon, the selection of the fatigue model is in itself a source of uncertainty.

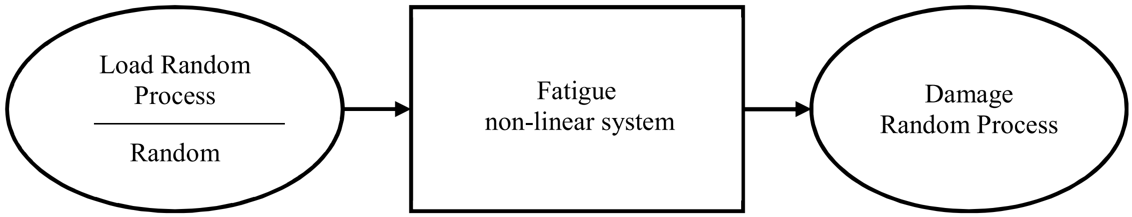


Figure 1.1 Schematic of a fatigue nonlinear system

Specifically, when the source of error is the poor accuracy of the mathematical model in describing the fatigue phenomenon, two circumstances are identified: an erroneous fatigue model is selected while a correct one exists, or only inaccurate models are available. Although the latter may yield reasonable results for specific cases and may become popular, their mathematical description is departing from the observed fatigue phenomenon.

## 1.3 Loading Random Process

Efforts to evaluate fatigue life uncertainty due to random loading exist since the early years of documented fatigue. At first, the scope was to quantify the quality of steels [7, 9]. Erker [31] identified the significant effect of the load random process to the fatigue life of mechanical components and pioneered the concept of load scatter, and the work in [32] tested white noise as input load. Many of the early constraints in evaluating the uncertainty in fatigue life from a load random process can be attributed to limitations of test machines which were relying on simple controls, insufficient onboard computing capacity and insufficient memory to model or store data. More recently, it was reported [33, 34] that variability in loading and material properties, data uncertainty due to measurement errors, and modeling uncertainty are still major sources of uncertainty in forecasting fatigue life. Metrologic or physical errors leading to variability of material definition or loading will not be discussed in this work. Instead, this research concentrates on developing and qualifying a new method to forecast fatigue life if a load random process is available only over a short period of time.

## 1.4 Fatigue to Failure Testing

To experience fatigue failure, a vehicle must travel more than 100k miles for example, corresponding to 4000 hours of operation for a 25 mph speed. The challenge however, is that this is type of testing is practically difficult to perform for 4000 hours because of its long duration. Another challenge is that an actual terrain profile is almost impossible to obtain. In addition, it varies for each vehicle. Figure 1.2 shows a simple schematic of a vehicle excited by rough terrain which is a common excitation source for durability studies.

Because the actual terrain profile cannot be obtained for a vehicle, it is common in practice to use a composite (synthetic) road profile of measured ground profiles (Belgian blocks, Kofa gravel, etc.) for approximately 1/3 of the desired warranty miles. Under this condition, durability tests can be performed in the laboratory. The test time reduction in this case can be approximately 25%, if the road profiles are compressed.

As we mentioned, durability proving ground testing takes too long. Also, the environment and the driver play a significant role (Figure 1.2). The conventional durability laboratory testing provides more control of the environment and the execution of the test is shorter (Figure 1.3). The state-of-the-art enhanced durability laboratory testing uses techniques to remove non-damaging sections (red portions in Figure 1.4) and accelerate testing by approximately 25%.


Figure 1.2 Vehicle on rough terrain

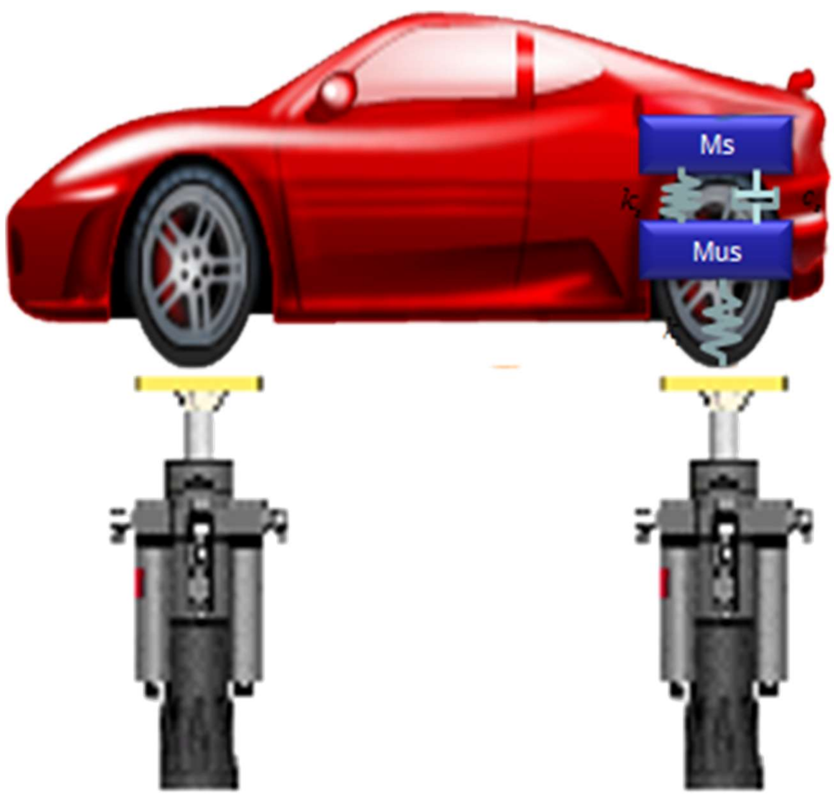


Figure 1.3 Durability laboratory testing

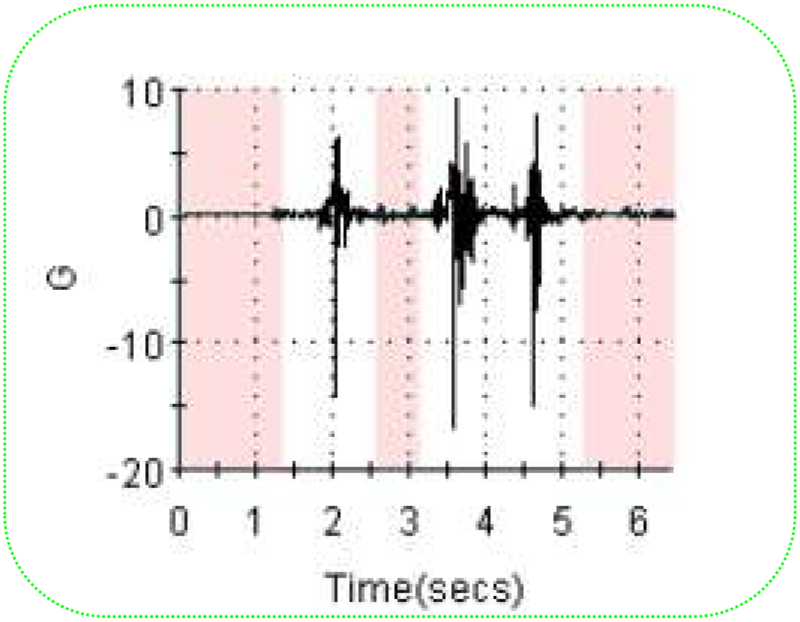


Figure 1.4 Road data reduction

## 1.5 Accelerated Life Testing (ALT)

Accelerated Life Testing (ALT) design is used to predict the product reliability under nominal stress level in a reasonable timeframe [35]. The product is tested in stress conditions higher than the nominal ones and then a stress-life relationship is used in order to obtain the reliability at the operating conditions. Experimental data of life are collected at the higher stress level and these are then used to predict the product reliability at the nominal stress level. Assumptions on the stress-life relationship and the life distribution at the elevated stress levels are commonly made.

Because the experimental data might not be enough and financial restrictions impose further difficulties in the testing process new ALT methodologies have been developed. Efforts to integrate ALT design with reliability analysis using computational models have been reported [36]. For instance, Dorp and Mazzuchi [37] developed a general Bayesian inference model for ALT design by assuming that the failure times at each stress level are exponentially distributed. They also developed a general Bayes–Weibull inference model for ALT by assuming the failure times follow Weibull distribution [38].

Elsayed and Zhang [39] developed a multiple-stress ALT model to overcome the limitation of traditional ALT models that only focus on a single stress. Zhang and Meeker [40] presented Bayesian methods for ALT planning with one accelerating variable and discussed how to obtain the optimal testing plan. Lee and Pan [41] studied the parameter estimation method of step-stress ALT (SSALT) model. Voiculescu et al. [42] studied the Arrhenius–Exponential model of ALT techniques using the maximum likelihood (ML) and Bayesian methods. Even though many methods have been developed and studied, most of these methods purely depend on testing data and make assumptions about the life distribution and stress–life relationship. Physics-informed computational models, however, are seldom considered during ALT design.

In this dissertation, the framework of a new ALT methodology is established as an extension of the proposed durability approach where commonly used assumptions on the stress-life relationship and the life distribution are lifted.

## 1.6 Dissertation Objectives

Below are the two main objectives of this research:

1. Develop a new durability test method with a much shorter duration compared to the current state-of-the-art method. The new method should estimate the required short testing time and also provide a synthetic

displacement load profile of approximately equal fatigue cumulative damage with an actual test. The synthetic profile should be used to execute the durability test.

2. Validate experimentally the proposed durability test method using the state-of-the-art durability equipment of the US Army's Ground Vehicle Systems Center (GVSC).

The developed methods will have wide practical applications in structural reliability, accelerated testing, design for lifecycle cost, preventive maintenance strategies, and fatigue reliability, among others.

# CHAPTER TWO

# LITERATURE REVIEW

## 2.1 Fatigue of Metals

The fatigue community often agrees that stress-based fatigue analysis is generally proper to analyze materials subject to dominant elastic response under cyclic loading conditions. Strain-based fatigue theories axiomatically describe fatigue damage as a function of plastic strain. While stress-based models are simply correlating the material cyclic stress response to fatigue life, strain-based models introduce phenomenological explanations relating material plastic response under cyclic-loading conditions to fatigue damage. Energy-based theories can be viewed as an evolution of the strain-based theories. Correlating the elastic and plastic energy in the material during each load-cycle to damage, the energy-based models attempt to relate fatigue to the fundamental law of conservation of energy.

Lastly, the category of multi-scale or mesoscopic plasticity models such as Dang Van’s criterion states that crack nucleation in slip bands occurs at the most unfavorable oriented grains subject to plastic deformation even if the macroscopic stresses are elastic. The multi-scale models find application to materials under cyclic-loading with high-cycle or infinite life response. These models can be considered a hybrid-evolution of stress and strain-based theories.

In the following, we provide a brief introduction to the theoretical support for strain-based fatigue, and a description of fatigue models which is limited to selection of models and various theories of fatigue modeling.

### 2.1.1 Strain-based Fatigue

Central to fatigue analysis is a damage model. The damage model equates combinations of stresses and strains as functions of regressed monotonic and cyclic material properties to predict fatigue damage. For damage models, if the input load is a random process, the output is a random fatigue damage process. In addition to the fatigue damage models (Figure 2.1), other fatigue theories are integrated in the fatigue non-linear system. They can be categorized by their scope as follows:

1. Constitutive theories such as material laws, regressed monotonic or cyclic material models, stress or strain formulations from the Cauchy's stress or strain tensor components.
2. Corrective theories such as corrections for elastic-plastic behavior, mean stress effects, surface roughness effect, and non-proportional loading conditions, among others.
3. Procedures or best practices for cycle counting methods, correct computational sequences, etc.
4. Stress- and strain-based models commonly applied to fatigue life predictions.

The stress-based fatigue model to predict fatigue life to failure is regarded as the traditional method and it is widely used since it requires less expensive testing for material characterization. Strain-based fatigue is a relatively newer method and enables exploring the relationship between material response to complex cyclic loading, and fatigue damage and damage accumulation. Strain-based fatigue damage models are mentioned here due to their presumed ability to model various fatigue physical phenomena.

Strain-based fatigue models use three fundamental assumptions. The first assumption is that only plastic strain produces fatigue damage. The second assumption relating to the concept of equivalent local strain illustrated in Figure 2.2, is that the fatigue life spent to crack nucleation and small crack growth in a notch component is the same as on a test specimen under identical strain conditions [43].

Applicable to both monotonic or cyclic loading conditions, the third assumption is that the total strain range is the sum of the elastic and plastic strain ranges. In Figure 2.3, the elastic and plastic strain ranges are plotted on a fully reversed stress-strain hysteresis loop where the loop is symmetric following Mashing hypothesis [44] without deteriorating effects (e.g. [45, 46]).

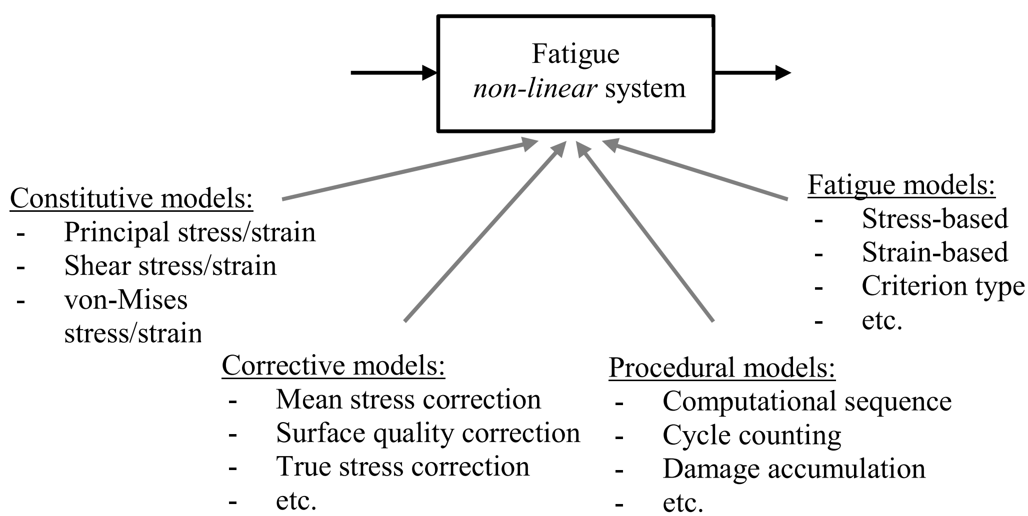


Figure 2.1 Components of fatigue non-linear system

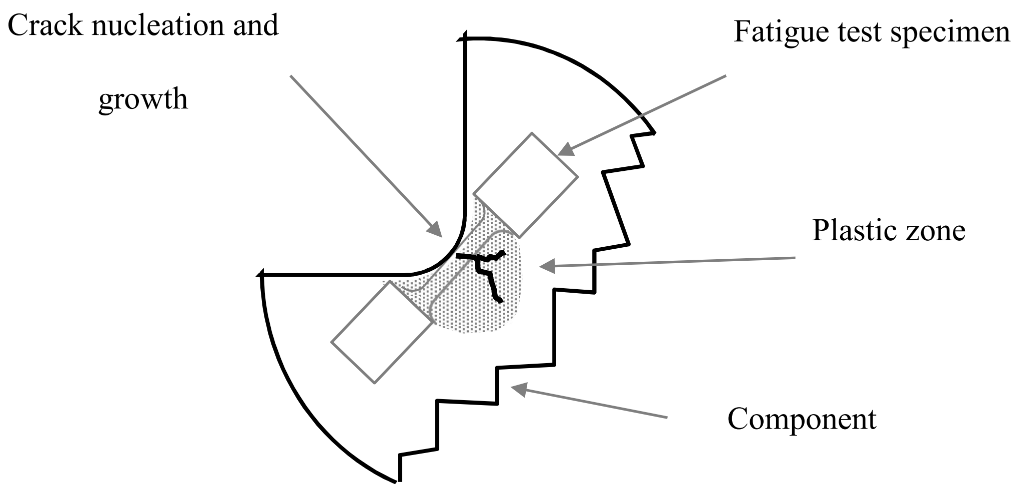


Figure 2.2 Concept of equivalent local strain

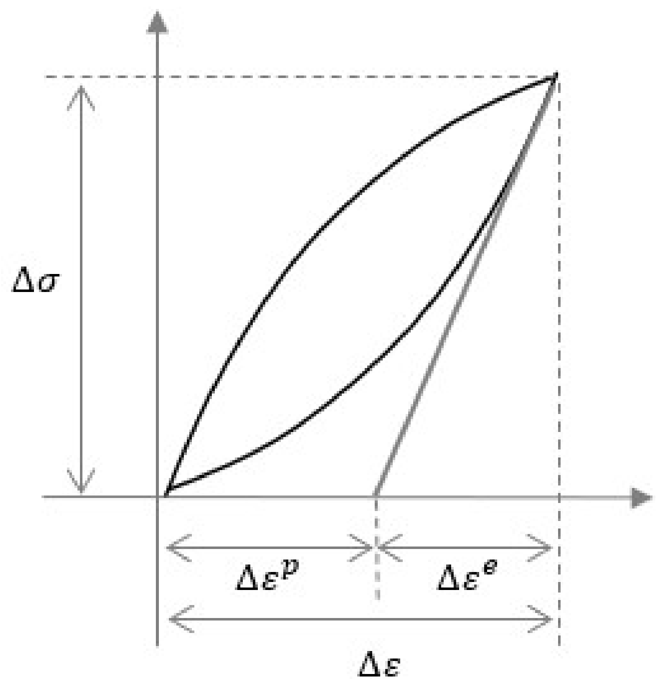


Figure 2.3 Elastic and plastic strain in a stress-strain hysteresis loop

The foundation of cyclic-plasticity in strain-based fatigue has been discussed and reviewed many times. In the following, the strain-based fatigue theory is approached from a perspective of input variable main effects and interaction effects.

For the monotonic loading of a material, the governing mathematical expression for total strain is the sum of elastic, $\varepsilon^e$, and plastic strain, $\varepsilon^p$, [43]:

$$\varepsilon = \varepsilon^e + \varepsilon^p \tag{2.1}$$

The form of the equation implies that the total strain is a function of the monotonic elastic and plastic strain main effects with no interactions. The elastic strain can be further defined as a function of the main effects and interaction effect between stress, $\sigma$, and Young modulus, $E$, as

$$\varepsilon^e = \frac{\sigma}{E} \tag{2.2}$$

The plastic strain, fitted by a curve in the stress-strain space is described by the main effects and interaction effects of stress, $\sigma$, monotonic hardening coefficient, $K$, and monotonic hardening exponent, $n$, as

$$\sigma = K(\varepsilon^p)^n \tag{2.3}$$

Combining the elastic and plastic strain expressions from Equations (2.2) and (2.3), Ramberg-Osgood [47] completed the analytical relationship between monotonic strains and material parameters that can be regressed from monotonic physical testing of the material as

$$\varepsilon = \varepsilon^e + \varepsilon^p = \frac{\sigma}{E} + \left(\frac{\sigma}{K}\right)^{\frac{1}{n}} \tag{2.4}$$

Equation (2.4) models the total monotonic strain as a function of main effects and interactions between the material stress response under load and its elastic and plastic properties with no interactions between elastic and plastic strains. Therefore, no interactions are presented between the material elastic properties and the hardening behavior.

Similarly, the cyclic strain developing in metals during a load cycle is assumed to maintain the additive property described in Equation (2.1) with the Ramberg-Osgood equation modified for the cyclic stress-strain stabilized response as

$$\varepsilon_a = \varepsilon_a^e + \varepsilon_a^p = \frac{\sigma}{E} + \left(\frac{\sigma}{K'}\right)^{\frac{1}{n'}} \tag{2.5}$$

where $\varepsilon_a$ is the strain amplitude, $\varepsilon_a^e$ is the elastic strain amplitude, $\varepsilon_a^p$ is the plastic strain amplitude, $K'$ is the cyclic strength coefficient, $n'$ is the cyclic strain hardening exponent and E is the monotonic Young modulus.

### 2.1.2 Fatigue damage models

Equation (2.5) describes the total strain response of a material under cyclic loading conditions as a function of the main effects and interaction effects of stress amplitude and Young modulus, stress amplitude, strain hardening coefficient and exponent. Applied to fatigue, the problem evolves to equating the cyclic elastic and plastic strain as a function of fatigue damage or fatigue life measured in reversals. At the macro-scale, the elastic behavior has been described by Basquin's Equation [48] where the fatigue life to failure (i.e. reversals, $2N_f$) results from main effects and interaction effects of cyclic elastic strain, Young modulus, fatigue strength coefficient, $\sigma_f'$, and strength exponent $b$ as

$$\varepsilon_a^e = \frac{\sigma_f'}{E}\left(2N_f\right)^b \tag{2.6}$$

Similarly, in the Manson-Coffin equation [49, 50], the fatigue life is described by the main effects and interaction effects of cyclic plastic strain, fatigue ductility coefficient, $\varepsilon_f'$, and exponent, $c$, as

$$\varepsilon_a^p = \varepsilon_f'\left(2N_f\right)^c. \tag{2.7}$$

Therefore, the strain-life approach to fatigue life estimation aggregates the cyclic elastic and plastic strains [51], and fatigue damage is a result of macro-scale cyclic elastic and plastic main effects with no interaction between elasticity and plasticity, i.e.

$$\varepsilon_a = \frac{\sigma_f'}{E}\left(2N_f\right)^b + \varepsilon_f'\left(2N_f\right)^c \tag{2.8}$$

For instance, if a ratio between elastic strain and plastic strain is defined as:

$$\varepsilon_a^e \big/ \varepsilon_a^p = \frac{\sigma_f'}{E}\left(2N_f\right)^b \Big/ \varepsilon_f'\left(2N_f\right)^c \tag{2.9}$$

the form of the equation implies that besides the main effect of elastic strain and plastic strain, there is an interaction effect between the two. Equation (2.9) is commonly used in strain-based fatigue analysis to determine the transition life by setting $\varepsilon_a^e \big/ \varepsilon_a^p = 1$.

The strain-life curve of Equation (2.8) is the foundation of macro-scale strain-based fatigue models attempting to describe the fatigue phenomenon more accurately. Still, to establish Equation (2.8) in accordance with the assumption of strain-based fatigue theory that only cyclic-plasticity produces fatigue damage, it must be assumed that macro-scale cyclic elastic strain does contain amounts of meso- or micro-scale plastic strains, and there are no other main effects and interactions. In this case, the Manson-

Coffin Equation (2.7) is sufficient to perform fatigue analysis. As a result, a multitude of complex models are developed to better describe fatigue damage.

### 2.1.3 Competing fatigue damage models

To determine which of competing models is the most appropriate for a particular application, the state-of-the-art fatigue theory is first investigated. An important aspect is to first categorize fatigue damage using quantifiable stages. For example, crack nucleation, accounting for most of the fatigue life for steel, short and long crack growth influences stages I and II respectively, and the final fracture. While crack nucleation is typically driven by shear stress, small and long crack growth as well as the final fracture are rather determined by a complex combination of loading conditions, accumulated damage and the material response to the fluctuating loads.

References [52 - 55], using AISI 304 stainless steel, Inconel 718 and normalized SAE1045, have provided a comprehensive set of observations to the fatigue damage phenomena. They observed, as shown in Figure 2.4 for Inconel under fully reversed axial loading conditions and in Figure 2.5 for SAE1045 steel under fully reversed torsional loading conditions, that fatigue damage modes occurring during crack nucleation and crack growth stages are indeed dependent on the instantaneous damage fraction, and material and loading conditions. Moreover, they revealed, as illustrated by comparing Figures 2.4 and 2.5, that each material exhibits a different fatigue damage mode depending on the damage fraction and loading conditions. Therefore, using a unique set of fatigue models and theories across materials, loading conditions and damage fractions may be incorrect.

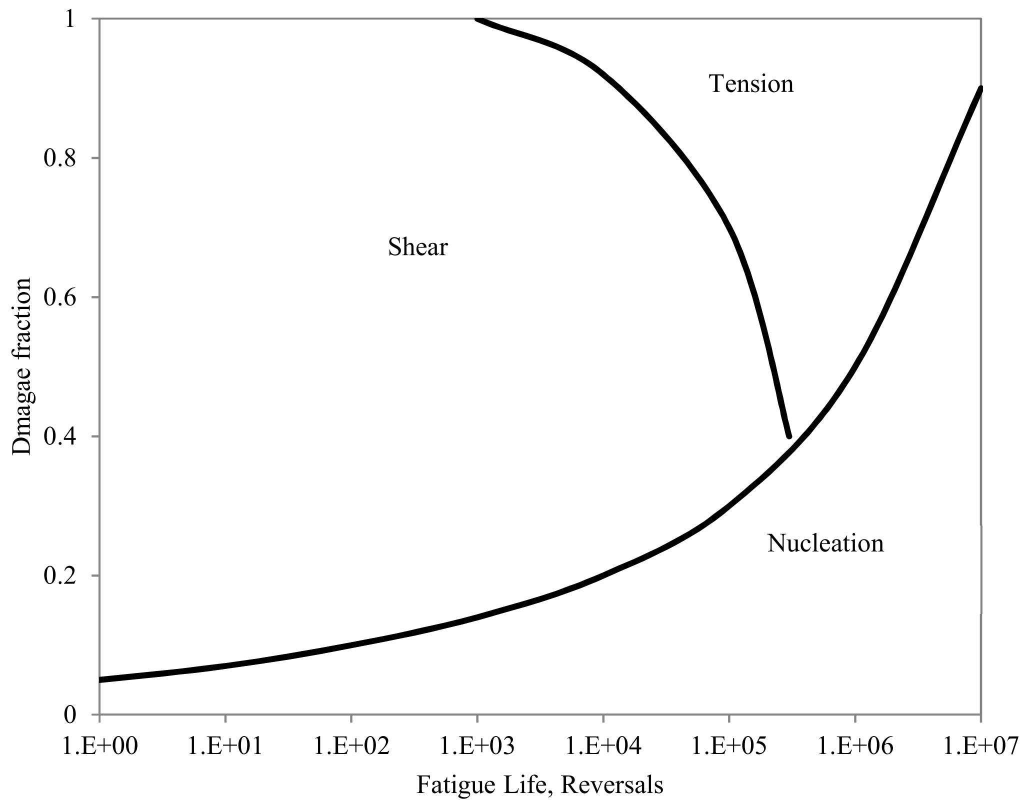


Figure 2.4 Damage mode for Inconel 718 under fully reversed axial load

Next, the state-of-the-art fatigue models are reviewed and compared to viable alternatives. For steel, Socie [52] proposed partitioning the fatigue life domain in three regions, A, B and C based on observed dominant fatigue damage mode. Fatigue damage models are also associated with each region. For region A, the Fatemi and Socie critical-plane model [56], (Equation 2.10), is selected since both nucleation and small crack growth is dominated by the shear damage mode. The model describes the main effect of the cyclic maximum shear strain and the interaction effects of the cyclic maximum shear strain, normal stress, and cyclic yield strength to predict early micro-yielding at crack nucleation sites. It is stated as

$$\frac{\gamma_{max}}{2}\left(1 + k_{FS}\frac{\sigma_{n,max}}{\sigma_y'}\right) = \left[\frac{\tau_f'}{G}\left(2N_f\right)^{b_0} + \gamma_f'\left(2N_f\right)^{b_0}\right] \tag{2.10}$$

where $\gamma_{max}/2$ is the maximum shear strain amplitude, $\sigma_{n,max}$ is the normal stress, $\sigma_y'$ is the cyclic yield strength, $k_{FS}$ is Fatemi-Socie material constant, $\tau_f'$ is the shear fatigue strength coefficient, $\gamma_f'$ is the shear fatigue ductility coefficient, $b_0$ is the shear fatigue strength exponent, and G is the monotonic shear modulus.

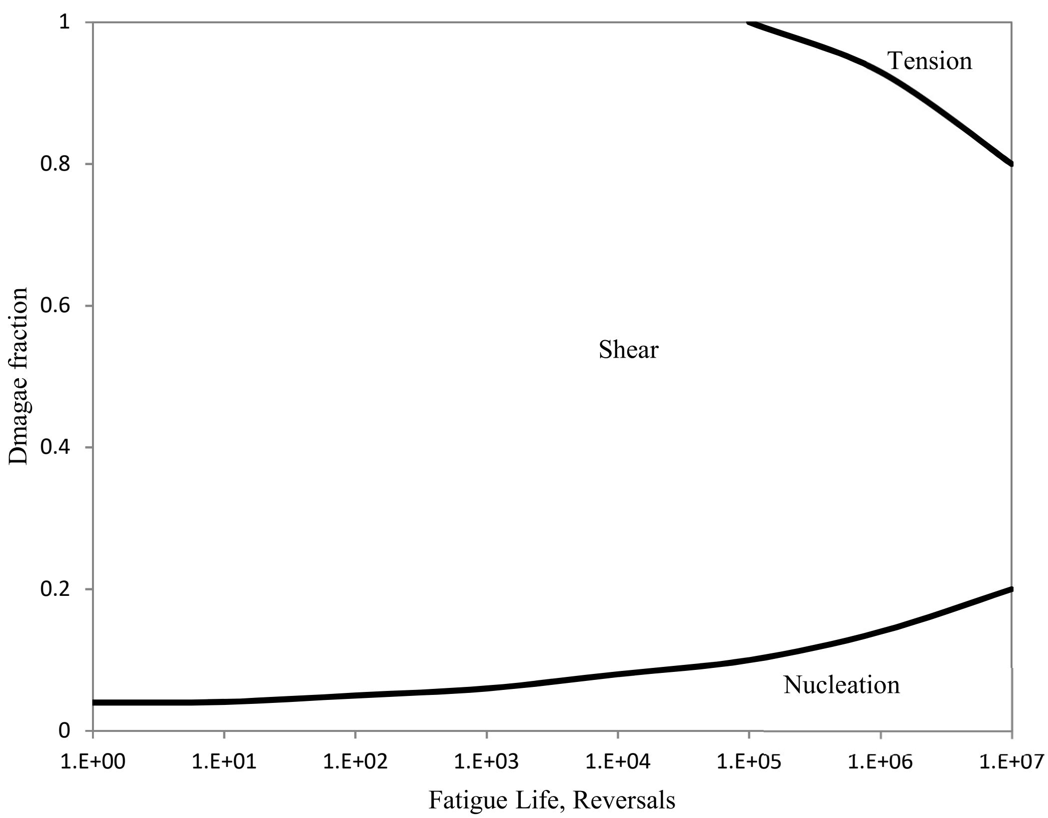


Figure 2.5 Damage mode for SAE1045 under fully reversed torsional load

In its long-form, Equation (2.10) is written for the axial cyclic parameters using the plastic and elastic Poisson ratios, $\nu_e,\ \nu_p$, as

$$\frac{\gamma_{max}}{2}\left(1+k_{FS}\frac{\sigma_{n,max}}{\sigma_y'}\right)=\left[(1+\nu_e)\frac{\sigma_f'}{E}\left(2N_f\right)^b+\left(1+\nu_p\right)\varepsilon_f'\left(2N_f\right)^c\right]\times\ldots$$
$$\ldots\times\left[1+k_{FS}\frac{\sigma_f'}{2\sigma_y'}\left(2N_f\right)^b\right] \tag{2.11}$$

Competing with Equation (2.10) or Equation (2.11), Liu [57] proposed a critical plane based virtual energy bi-model with equations for tensile and shear damage modes. Based on Socie's observation that crack nucleation and growth in presence of aggressive plastic damage is dominated by the shear damage mode, Liu's model for the shear damage mode can be a viable alternative. It is expressed as

$$\Delta W_{II}=(\Delta\tau\Delta\gamma)_{max}+\Delta\sigma_n\Delta\varepsilon_n=4\frac{\left(\tau_f'\right)^2}{G}\left(2N_f\right)^{2b_0}+4\tau_f'\gamma_f'\left(2N_f\right)^{b_0+c_0} \tag{2.12}$$

where $(\Delta\tau\Delta\gamma)_{max}$ is the maximum of the product between shear stress and strain ranges and $\Delta\sigma_n\Delta\varepsilon_n$ is the product between stress and strain ranges normal to the plane defined by $(\Delta\tau\Delta\gamma)_{max}$.

For region B [52], small crack growth is dominated by the tensile damage mode. Because of this, the maximum principal strain and stress in the direction of the maximum principal strain formulation of Smith-Watson-Topper [58] energy density method for fatigue damage was proposed. It implicitly considers main effects and interaction effects of axial stress and strain and is stated as

$$\varepsilon_{1,a}\sigma_{N,max}=\frac{{\sigma_f'}^2}{E}\left(2N_f\right)^{2b}+\sigma_f'\varepsilon_f'\left(2N_f\right)^{b+c} \tag{2.13}$$

where $\varepsilon_{1,a}$ is maximum principal strain and $\sigma_{N,max}$ is the stress coplanar to the maximum principal strain.

Liu's [57] critical plane based virtual energy model for tensile damage mode can also be considered as an alternative fatigue model for region B where the main effects and the interaction effects of axial stress and strain are dominant to fatigue damage. It is described as

$$\Delta W_I = (\Delta\sigma\Delta\varepsilon)_{max} + \Delta\tau\Delta\gamma = 4\frac{(\sigma_f')^2}{E}(2N_f)^{2b} + 4\sigma_f'\varepsilon_f'(2N_f)^{b_0+c_0} \tag{2.14}$$

where $(\Delta\sigma\Delta\varepsilon)_{max}$ is the maximum of the product between axial stress and strain ranges and $\Delta\tau\Delta\gamma$ is the product between shear stress and strain ranges normal to the plane defined by $(\Delta\sigma\Delta\varepsilon)_{max}$ .

Region C [52] is typically defined by fatigue cracks nucleating at multiple sites and then connecting due to accumulated damage during the fatigue life. Socie [52] determined that a maximum shear stress combined with a crack closing or opening effect from the normal stress to the maximum shear stress plane [59] is suitable. The model (Equation 2.15)

$$\frac{\tau_{max}}{2} + k_{FS}\sigma_{n,max} = \tau_f'(2N_f)^b \tag{2.15}$$

where $\tau_{max}/2$ is the maximum shear stress amplitude, implies that the main effects of the cyclic maximum shear stress and normal stress to the maximum shear stress plane, and with no interaction effects, is descriptive to the fatigue mechanism.

For region C, as defined in [52], ranging from long- to infinite fatigue life with no observable macroscopic cyclic plastic strain damage, simple stress type models can be viable choices.

For each crack nucleation and crack growth region various stress- and strain-based fatigue models have been proposed and many could be deemed descriptive of a fatigue mechanism. The presented fatigue models are well-researched and they are competing with each other in terms of applicability.

# CHAPTER THREE

# FUNDAMENTALS OF FATIGUE DAMAGE

Predicting fatigue damage for structural components subjected to variable loading conditions is a complex issue. The first, simplest, and most widely used damage model is the linear damage. This rule is often referred to as Miner's rule [17]. However, in many cases the linear rule often leads to non-conservative life predictions. The results from this approach do not consider the effect of load sequence on the accumulation of damage due to cyclic fatigue loading. Since the introduction of the linear damage rule many different fatigue damage theories have been proposed to improve the accuracy of fatigue life prediction. A comprehensive review of many fatigue damage approaches can be found elsewhere [56].

## 3.1 Fatigue Reliability

Fatigue failure is a cumulative event due to cyclic loading. The damage $d$ is the ratio of the current crack length $\alpha$ to the final crack length $\alpha_f$ at failure. The following, experimentally verified, Manson-Halford model

$$d = \frac{\alpha}{\alpha_f} = \frac{1}{\alpha_f}\left[\alpha_0 + \left(\alpha_f - \alpha_0\right)\left(\frac{n}{N_f}\right)^{\alpha_f}\right] = \left(\frac{n}{N_f}\right)^{\frac{2}{3}N_f^{0.4}} \tag{3.1}$$

provides the incremental damage $d$ after $n$ cycles at a constant amplitude cyclic load (e.g. stress) which fails the specimen in $N_f$ cycles. The initial crack length $\alpha_0$ is assumed negligible compared to the experimentally determined $\alpha_f = \left(\frac{n}{N_f}\right)^{\frac{2}{3}N_f^{0.4}}$ for commonly used materials. To simplify the nonlinear Manson-Halford model of Equation (3.1), the following linear damage Palmgren-Miner damage model [60] is common

$$d = \frac{n}{N_f} \tag{3.2}$$

To use the damage models of Equations (3.1) and (3.2), we first count (or estimate) the number of cycles $n_i$ at stress level $S_i$ and use the material *S-N* curve to calculate the number of cycles $N_{f,i}$ the specimen will fail under the cyclic load $S_i$. Model (3.1) or (3.2) is then used to calculate the incremental damage $d_i$. The cumulative damage $D$ is calculated by summing up the incremental damage $d_i$ over all load (stress) levels $i$ as

$$D = \sum_{i} d_i \tag{3.3}$$

For a zero-mean stationary random stress signal and under the very strong assumption of a narrow-band random process, the linear damage model

$$D = \sum_{i} d_i = \sum_{i} \frac{n_i}{N_{f,i}} \tag{3.4}$$

provides the following expected damage [60]

$$E(D) = \frac{\nu_0 T}{A} \int_{0}^{\infty} s^m f_s(s) ds \tag{3.5}$$

where $\nu_0$ is the mean up-crossing rate, $T$ is the signal duration, $A$ and $m$ are coefficients of the S-N curve $\left(N_f \cdot S^m = A\right)$ and $f_s(s)$ is the PDF of the peak stress ($S$) level. The distribution $f_s(s)$ is used for cycle counting under the narrow-band assumption (existence of a negative stress trough equal in magnitude with a positive stress peak to form a load cycle). It should be noted that $D$ is a random variable and its range of values (e.g., 95th percentile minus 5th percentile) can be wide. Thus, the expected value $E(D)$ may be of limited practical significance.

It can be shown that for a zero-mean, Gaussian, narrow-band process (e.g., harmonic process with constant frequency and random amplitude), $f_s(s)$ is Rayleigh distributed as

$$f_s(s) = \frac{s}{\sigma_X^2} \, exp\left(-\frac{s^2}{2\sigma_X^2}\right) \tag{3.6}$$

where $\sigma_X^2$ is the variance of the underlying Gaussian process $X(t)$. In this case, the linear damage model of Equation (3.5) yields [60]

$$E(D) = \frac{\nu_0 T}{A}\left(\sqrt{2}\sigma_X\right)^m \Gamma\left(\frac{m}{2}+1\right) \tag{3.7}$$

For a zero-mean, Gaussian, wide-band process with irregularity factor $\alpha = \frac{\nu_0}{\nu_p}$ (ratio of zero up-crossing frequency to peak frequency), the distribution $f_s(s)$ is provided by the following Rice formula [61]

$$f_s(s) = (1-\alpha^2)\frac{1}{\sqrt{2\pi(1-\alpha^2)}\sigma_X} \cdot exp\left(-\frac{s^2}{2(1-\alpha^2)\sigma_X^2}\right)$$

$$+\alpha\Phi\left(\frac{\alpha}{\sqrt{1-\alpha^2}} \cdot \frac{s}{\sigma_X}\right)\frac{s}{\sigma_X^2} \cdot exp\left(-\frac{s^2}{2\sigma_X^2}\right) \tag{3.8}$$

and is plotted in Figure 3.1. Note that peaks occur below $s=0$ if the process is not narrow band $(\alpha < 1)$. This is not physically realizable because it violates the cycle counting assumption.

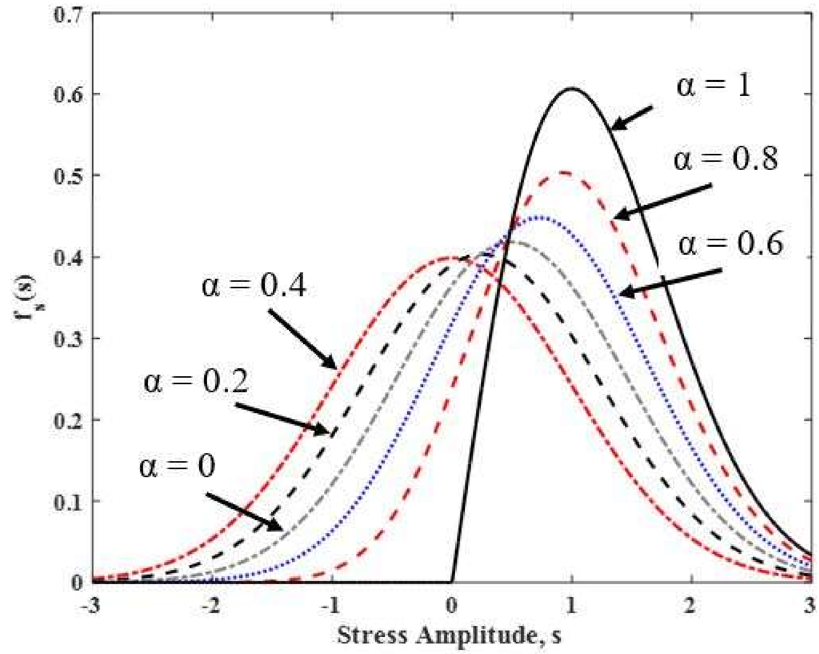


Figure 3.1 Rice PDF of peak stress for different values of $\alpha$

The following Powell distribution of peak stresses

$$f_s(s) = \frac{\frac{d}{d_s}({\nu_s}^+)}{\nu_p} \tag{3.9}$$

does not depend on the Gaussian assumption. However, it cannot be used for cycle counting unless we assume a narrow band process. In Equation (3.9), ${\nu_s}^+$ is the up-crossing rate for stress level $s$ and $\nu_p$ is the peak frequency. Both ${\nu_s}^+$ and $\nu_p$ can be calculated numerically for a non-Gaussian distribution [62].

Dirlik [63] has developed an empirical peak stress distribution using Monte Carlo simulations and rainflow cycle counting as a weighted average of an exponential and two Rayleigh distributions. Dirlik's peak stress distribution is considered more accurate compared to Equations (3.6) or (3.8) for wide-band processes [63]. However, it can only be used to estimate the expected (not the actual) cumulative damage as in Equation (1.6).

Fatigue failure occurs if $D$ is greater than one ($D > 1$). The fatigue life $T_L$ is random because of 1) randomness of the input (represented by a provided spectrum), 2) inherent variability of the test component (material properties, dimensions, etc.), and 3) uncertainty in the definition of the S-N curve (randomness of $m$ and $A$ coefficients). The fatigue reliability $R(T)$ at time $T$ is defined as the probability that $T_L$ is greater than $T$; i.e.,

$$R(T) = Pr(T_L > T) \text{ or } R(T) = Pr(D < 1). \tag{3.10}$$

## 3.2 S-N Curve

Well before a microstructural understanding of fatigue processes was developed, engineers had developed empirical means of quantifying the fatigue process and designing against it. Perhaps the most important concept is the S-N diagram (Figure 3.2), in which a constant cyclic stress amplitude S is applied to a specimen and the number of loading cycles N until the specimen fails is determined. Millions of cycles might be required to cause failure at lower loading levels, so the abscissa in usually plotted logarithmically.

In some materials, notably ferrous alloys, the S-N curve flattens out eventually, so that below a certain endurance limit $\sigma_e$ failure does not occur no matter how long the loads are cycled. Obviously, the designer will size the structure to keep the stresses below $\sigma_e$ by a suitable safety factor if cyclic loads are to be withstood. For some other materials such as aluminum, no endurance limit exists and the designer must arrange for the planned lifetime of the structure to be less than the failure point on the S-N curve.

Statistical variability is troublesome in fatigue testing. It is necessary to measure the lifetimes of perhaps twenty specimens at each of ten or so load levels to define the S-N curve with statistical confidence. It is generally impossible to cycle the specimen at more than approximately 10 Hz (inertia in components of the testing machine and heating of the specimen often become problematic at higher speeds) and at that frequency it takes 11.6 days to reach 107 cycles of loading. Obtaining a full S-N curve is obviously a tedious and expensive procedure.

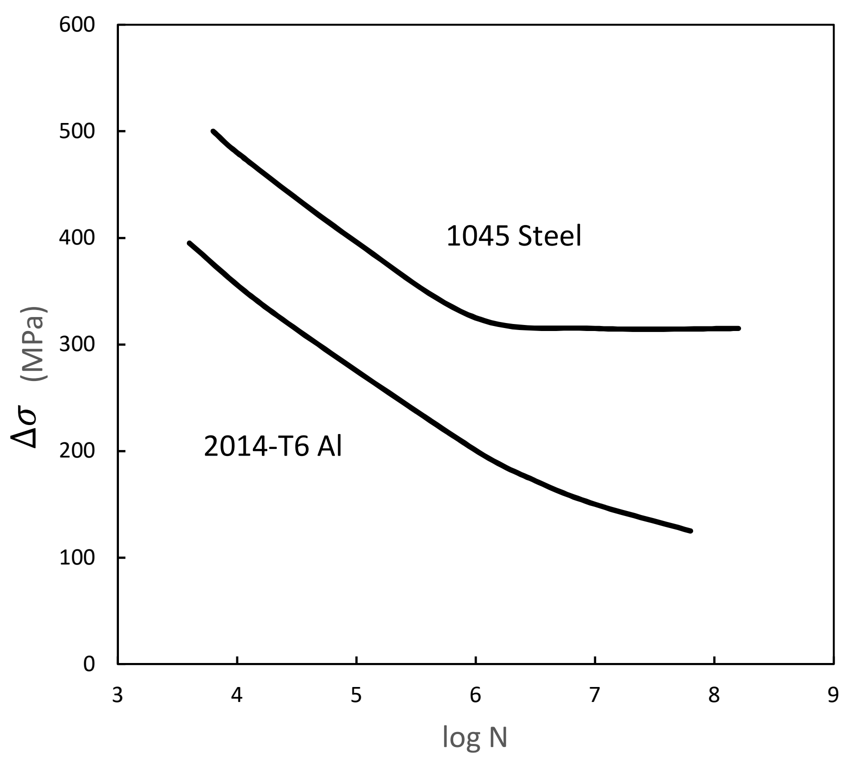


Figure 3.2 S-N curves for aluminum and low-carbon steel

At first glance, the scatter in measured lifetimes seems very large, especially given the logarithmic scale of the abscissa. If the coefficient of variability in conventional tensile testing is usually only a few percent, why do the fatigue lifetimes vary over orders of magnitude? It must be remembered that in tensile testing, we are measuring the variability in stress at a given number of cycles (one), while in fatigue we are measuring the variability in cycles at a given stress. Stated differently, in tensile testing we are generating vertical scatter bars, but in fatigue they are horizontal (Figure 3.3). Note that we must expect more variability in the lifetimes as the S -N curve becomes flatter, so that materials that are less prone to fatigue damage require more specimens to provide a given confidence limit on lifetime.

In high-cycle fatigue, the material performance is commonly characterized by an S-N curve, also known as a Wöhler curve (Figure 3.4). This is a graph of the magnitude of a cyclic stress (S) against the logarithmic scale of cycles to failure (N).

S-N curves are derived from tests on samples of the material to be characterized (often called coupons) where a regular sinusoidal stress is applied by a testing machine which also counts the number of cycles to failure. This process is sometimes known as coupon testing. Each coupon test generates a point on the plot though in some cases there is a runout where the time to failure exceeds that available for the test (censoring). Analysis of fatigue data requires techniques from statistics, especially survival analysis and linear regression.

The progression of the S-N curve can be influenced by many factors such as corrosion, temperature, residual stresses, and the presence of notches.

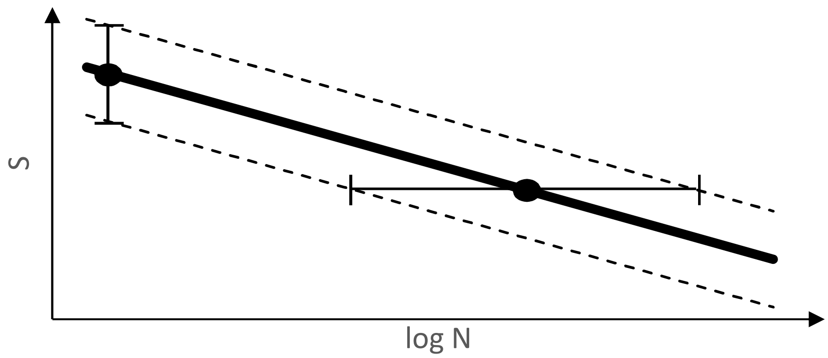


Figure 3.3 Variability in fatigue lifetimes and fracture strengths

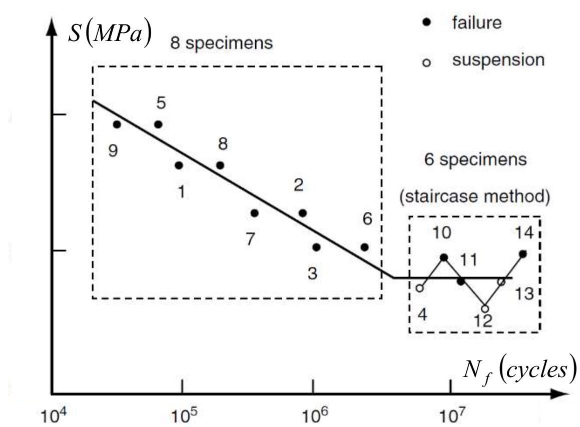


Figure 3.4 Wöhler curve

## 3.3 Effect of Mean Load

Of course, not all actual loading applications involve fully reversed stress cycling. A more general sort of fatigue testing adds a *mean stress* $\sigma_m$ on which a sinusoidal cycle is superimposed, as shown in Figure 3.5. Such a cycle can be phrased in several ways, a common one being to state the alternating stress $\sigma_{alt}$ and the *stress ratio* $R = \sigma_{min}/\sigma_{max}$.

For fully reversed loading, $R = -1$. A stress cycle of $R = 0.1$ is often used in aircraft component testing, and corresponds to a tension-tension cycle in which $\sigma_{min} = 0.1\sigma_{max}$.

A very substantial amount of testing is required to obtain an S-N curve for the simple case of fully reversed loading, and it will usually be impractical to determine whole families of curves for every combination of mean and alternating stress.

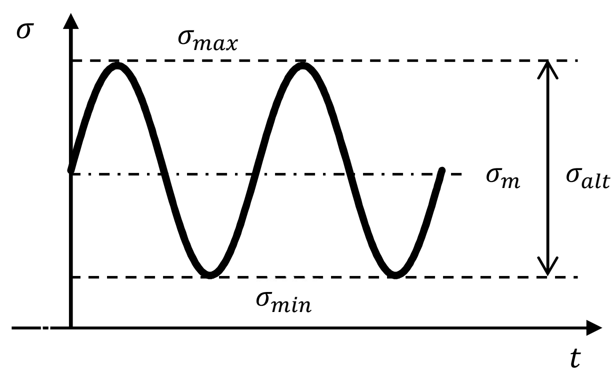


Figure 3.5 Simultaneous mean and cyclic loading

There are different models to correct for the mean stress effect. One of them for example, is the Goodman diagram (Figure 3.6) where a graph is constructed with mean stress as the abscissa and alternating stress as the ordinate, and a straight “lifeline" is drawn from $\sigma_e$ on the $\sigma_{alt}$ axis to the ultimate tensile stress $\sigma_f$ on the $\sigma_m$ axis. Then for any given mean stress, the endurance limit - the value of alternating stress at which fatigue fracture never occurs - can be read directly as the ordinate of the lifeline at that value of $\sigma_m$. Alternatively, if the design application dictates a given ratio of $\sigma_e$ to $\sigma_{alt}$, a line is drawn from the origin with a slope equal to that ratio. Its intersection with the lifeline then gives the effective endurance limit for that combination of $\sigma_f$ and $\sigma_m$.

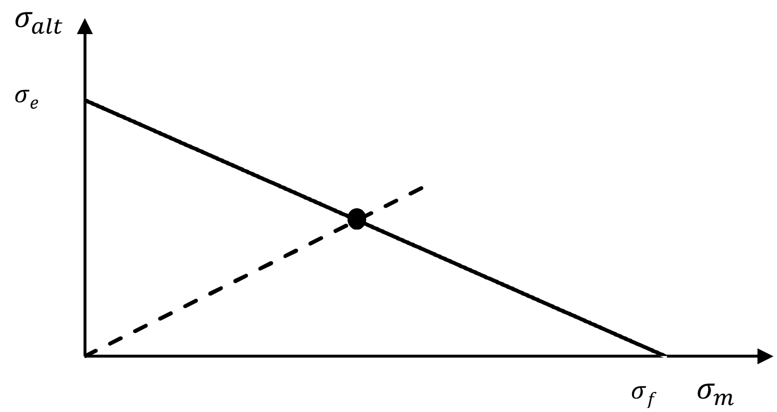


Figure 3.6 Illustration of Goodman diagram

## 3.4 Miner's Rule

When the cyclic load level varies during the fatigue process, a cumulative damage model is often hypothesized. To illustrate, take the lifetime to be $N_1$ cycles at a stress level $\sigma_1$ and $N_2$ at $\sigma_2$. If damage is assumed to accumulate at a constant rate during fatigue and a number of cycles $n_1$ is applied at stress $\sigma_1$, where $n_1 < N_1$ (Figure 3.7), then the fraction of lifetime consumed will be $n_1 < N_1$. To determine how many additional cycles the specimen will survive at stress $\sigma_2$, an additional fraction of life (Figure 3.7) will be available such that the sum of the two fractions equals one

$$\frac{n_1}{N_1} + \frac{n_2}{N_2} = 1 \tag{3.11}$$

Note that absolute cycles and not log cycles are used here. Solving for the remaining cycles permissible at $\sigma_2$

$$n_2 = N_2\left(1 - \frac{n_1}{N_1}\right) \tag{3.12}$$

The generalization of this approach is called Miner's Law, and can be written as

$$\sum \frac{n_i}{N_i} = 1 \tag{3.13}$$

where $n_i$ is the number of cycles applied at a load corresponding to a lifetime of $N_i$ .

The Miner's “law" should be viewed like many other material “laws," as a useful approximation, quite easy to apply, that *might* be accurate enough to use in design. But damage accumulation in fatigue is usually a complicated mixture of several different mechanisms, and the assumption of linear damage accumulation inherent in Miner's law should be viewed skeptically. If portions of the material's microstructure become unable to bear load as fatigue progresses, the stress must be carried by the surviving microstructural elements. The rate of damage accumulation in these elements then increases, so that the material suffers damage much more rapidly in the last portions of its fatigue lifetime. If on the other hand, cyclic loads induce strengthening mechanisms such as molecular orientation or crack blunting, the rate of damage accumulation could drop during some part of the material's lifetime. Miner's law ignores such effects, and often fails to capture the essential physics of the fatigue process.

It should also be noted that almost all available fatigue data for design purposes is based on constant-amplitude tests. In practice, however, fatigue stress is typically of variable amplitude or random.

Chapter 2 provides a comprehensive review of the models that have been proposed to predict fatigue life in components subject to variable-amplitude stress using constant-amplitude data to define fatigue strength. Yet the original model, a linear damage rule originally suggested by Palmgren [9] and developed by Miner [17], maintains its popularity principally because of its simplicity. Moreover, the engineering profession has not been convinced that any of the other more refined model will consistently outperform Miner's rule. As a result, Miner's rule is specified in almost every design code world-wide.

In the following development of Miner's rule, it is assumed that the stress process can be described by discrete events (stress cycles) and that a spectrum of amplitudes of stress cycles can be defined. Such a spectrum will lose any information on the applied sequence of stress cycles that may be important in some cases. It is also assumed that a constant-amplitude $S-N$ curve is available, and this curve is compatible with the definition of stress; that is, at this point there is no explicit consideration or the possibility of mean stress.

Figure 3.7 illustrates a stress spectrum described as a sequence of constant-amplitude blocks, each block having stress amplitude $S_i$ and the total number of applied cycles $n_i$. The constant-amplitude $S-N$ curve is also shown. Consider the first block having stress level $S_1$. From the $S-N$ curve, we note that the number of cycles to failure at this level is $N_1$. But only $n_1 < N_1$ cycles are applied (assuming no failure). Therefore, we can define a fractional damage $n_1/N_1$, Clearly, failure would occur if this fraction exceeds unity. This suggests that we can define a fractional damage at each stress level

$n_i/N_i$ and define a total damage as the sum of all the fractional damages over a total of $k$ blocks,

$$D = \sum_{i=1}^{k} \frac{n_i}{N_i} \tag{3.14}$$

The event of failure is then determined if

$$D \geq 1 \tag{3.15}$$

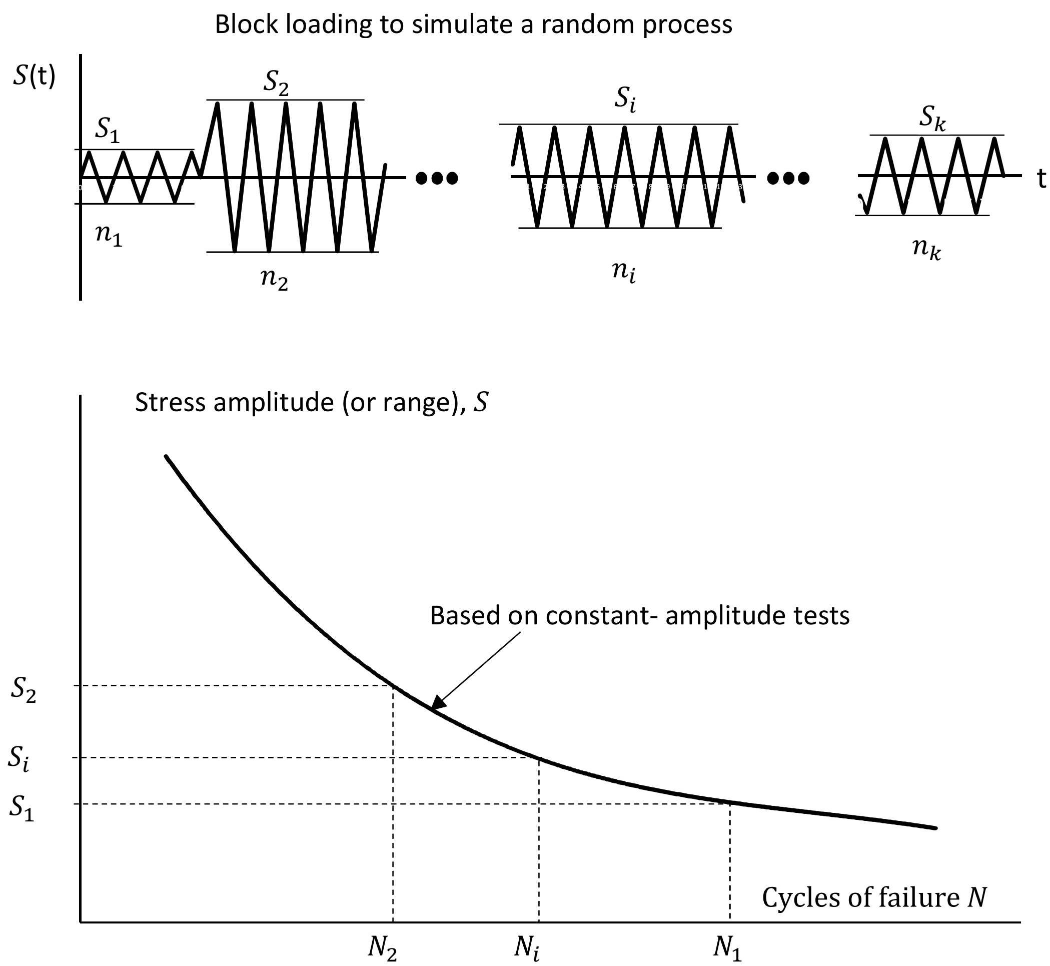


Figure 3.7 Illustration of Miner's rule

## 3.5 Damage to Failure

Structural components are frequently subjected to complex time histories of stress for which the prevalent mode of failure is fatigue. Fatigue analysis is driven by the sequence of maxima *(peaks)* and minima *(valleys)* in the stress-time history. In particular, the distance *b* between a peak and the following valley (or vice versa), and the mean value between them are of interest. However, two consecutive peaks (or valleys) cannot define a fatigue, in general. For this reason, fatigue cycles must be obtained using a suitable cycle counting method. The most used counting method is the rainflow algorithm which determines all fatigue cycles. For that, a peak $p$ and a valley $v$, that may not be consecutive, are properly extracted from the stress-time history by an empirical procedure and the corresponding range $r = (p - v)/2$ and mean $m = (p + v)/2$ values are determined. Subsequently, the cumulative fatigue damage is calculated using a fatigue model (see Chapter 2).

In the design of structures subjected to random loading, such as terrain excited vehicle vibrations, a realistic description of the actual working stress can be obtained only in a statistical way by modelling the corresponding irregular stress-time history as a random process. In these cases, the most important problem for fatigue analysis is the determination of the statistical distribution of fatigue cycles classified by the range $r$ and the mean $m$.

The sequence of peaks and valleys in the time records of a random loading process depends on the distribution of energy over frequency, which is characterized by the power spectral density (PSD). Usually, a stationary random process is called *broad-band* (or *wide-band*) if its PSD has significant values over a wide range of frequencies, whereas a process with the opposite property is defined as *narrow band.* Narrow band and broad band processes exhibit different dynamic behavior in the time domain. In narrow band processes, the peaks and valleys arc almost symmetrically with respect to the mean level of the process, whereas, in wide-band processes, consecutive peaks and valleys can occur without a mean level crossing. The relationship between the statistical distributions of peaks and the shape of the PSD has been theoretically addressed for both narrow-band and wide-band processes, whereas the relationship between the distribution of the heights and, consequently, of the fatigue cycles has been theoretically explained only for the narrow-band case.

For wide-band processes, the distribution of fatigue cycles can be obtained in the time domain by applying an appropriate cycle counting algorithm to a statistically representative number of sample realizations of the stress history (time trajectories) which are obtained experimentally or theoretically if the random process is characterized mathematically using KL expansion, for example.

The following section describes the rainflow algorithm in detail.

### 3.5.1 Rainflow Counting Algorithm (Wide or Narrow-band)

The rainflow-counting algorithm reduces a spectrum of varying stress into an equivalent set of simple stress reversals. The method successively extracts the smaller interruption cycles from a sequence, which models the material memory effect seen with stress-strain hysteresis cycles. This simplification allows the fatigue life of a component to be determined for each rainflow cycle using for example, Miner's rule to calculate the fatigue damage, or a crack growth equation to calculate the crack increment.

The rainflow counting algorithm was first developed by Matsuiski and Endo [18]. The algorithm is compatible with stress-strain hysteresis cycles. When a material is cyclically strained, a plot of stress against strain shows loops forming from the smaller interruption cycles. At the end of the smaller cycle, the material resumes the stress-strain path of the original cycle, as if the interruption had not occurred. The closed loops represent the energy dissipated by the material.

In principle, range counting includes counting of all successive load ranges, including small load variations occurring between adjacent larger ranges. It might be thought that small load variations can be disregarded in view of a negligible contribution to fatigue damage. However, a fundamental counting problem arises if a small load variation occurs between larger peak values.

The most commonly used rainflow algorithm is the four-point cycle counting rule using four consecutive points in a load-time history to determine whether a cycle is formed. The algorithm has been adopted in SAE and ASTM standards. Figure 3.8 illustrates the principle using two possible cycles counted in a nominal stress-time history and the corresponding local stress–strain response. One cycle is a hanging cycle in (a) and the other is a standing cycle in (b). The four consecutive stress points ($S_1, S_2, S_3, S_4$) define the inner ($\Delta S_1 = |S_2 - S_3|$) and the outer stress range ($\Delta S_0 = |S_1 - S_4|$). If the inner stress range is less than or equal to the outer stress range ($\Delta S_1 \leq \Delta S_0$), and the points comprising the inner stress range are bounded by (between) the points of the outer stress range, the inner cycle from $S_2$ to $S_3$ is extracted, the two inner points are discarded, and the two outer points ($S_1$ and $S_4$) are connected to each other. Otherwise, no cycle is counted, and the same check is done for the next four consecutive stress points ($S_2, S_3, S_4, S_5$) until all data of the discretized signal are considered.

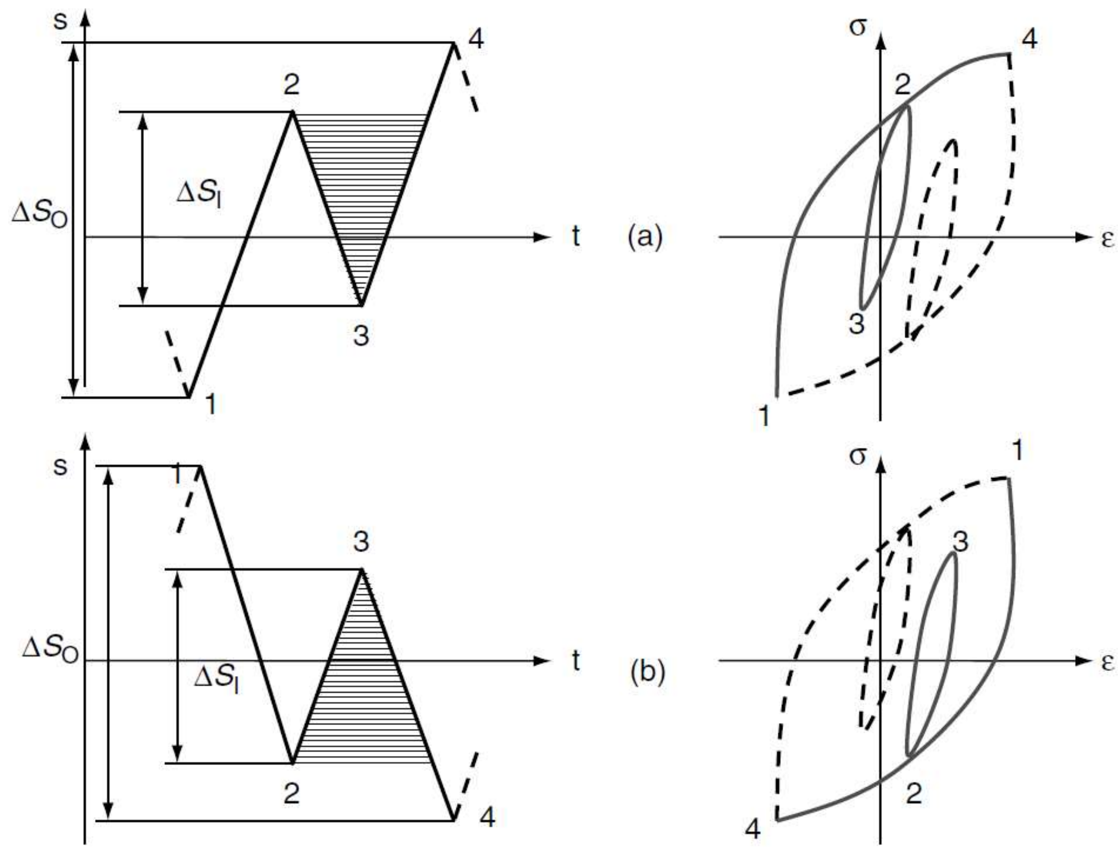


Figure 3.8 Principle of four-point rainflow cycle counting algorithm

Unlike the three-point rainflow cycle counting method, this technique does not guarantee that all data points will form closed cycles. The remaining data points that cannot constitute a cycle form the so-called *residue*. With this difference, the three-point rainflow counts can still be derived from the four-point counting as follows:

1. Extract the cycles and the residue, based on the four-point counting method
2. Duplicate the residue to form a sequence of [residue + residue]
3. Apply the same rainflow technique to the sequence of [residue + residue]
4. Add the newly extracted cycles to the original cycles

Both rainflow cycle counting methods lead to an identical range–mean rainflow matrix.

There are some unique features of the four-point cycle counting method. First, it is very easy to use in conjunction with as-recorded data acquisition and data reduction, because it does not require rearrangement of the load-time history. Second, it can be easily implemented for cycle extrapolation and load-time history reconstruction. Finally, the four-point cycle counting method is very generic, because the three-point rainflow matrix can be deduced from the four-point rainflow matrix and its residue.

Below, we present an example of using the four-point rainflow cycle counting method to determine the number of cycles in the load-time history of Figure 3.9.

First, we check the load-time history to ensure that it contains only the peaks and valleys. Then we apply the four-point rainflow cycle counting method to every four consecutive load points in the history. The first cycle is formed from -3 to 1.8 and the two data points are extracted. A new load-time history is generated by connecting the point before 5 and the point after -3 to each other. This is illustrated in Figure 3.19(a). The same process is carried out until the second cycle from 4.2 to 0.6 is identified as shown in Figure 3.19(b). The process continues until we run out of points as shown in Figures 3.19(c), (d) and (e). Finally, the four-point rainflow residue signal is shown in Figure 3.19(f).

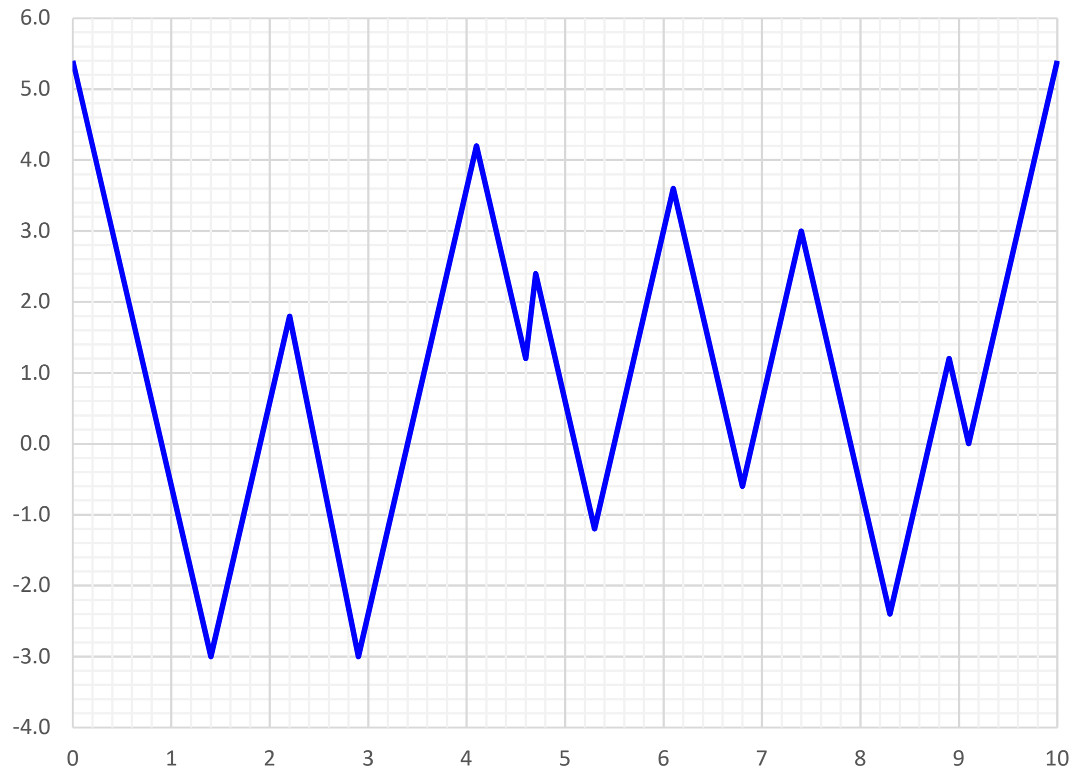


Figure 3.9 Example of a service load-time history

Then, we form the double residue signal of Figure 3.20 and apply again the four-point algorithm on it (see Figures 3.20(a) to 3.20(c)). Figure 3.21 shows the last remaining points (three in number).

After all damage cycles are identified, we can present the cycles using a peak to valley count (Tables 3.1) or equivalently a from - to rainflow matrix (**Error! Reference source not found.**).

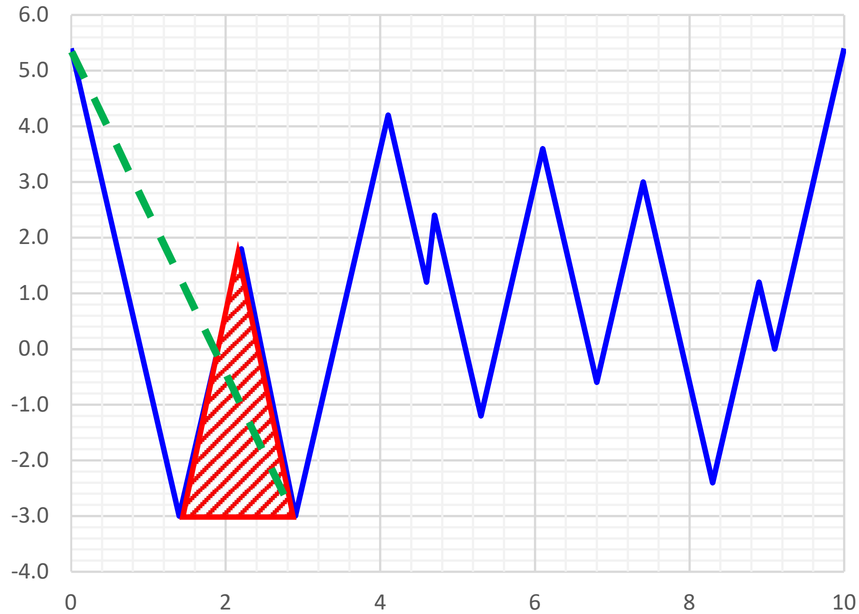


Figure 3.19(a) Extracted cycle from -3.0 to 1.2

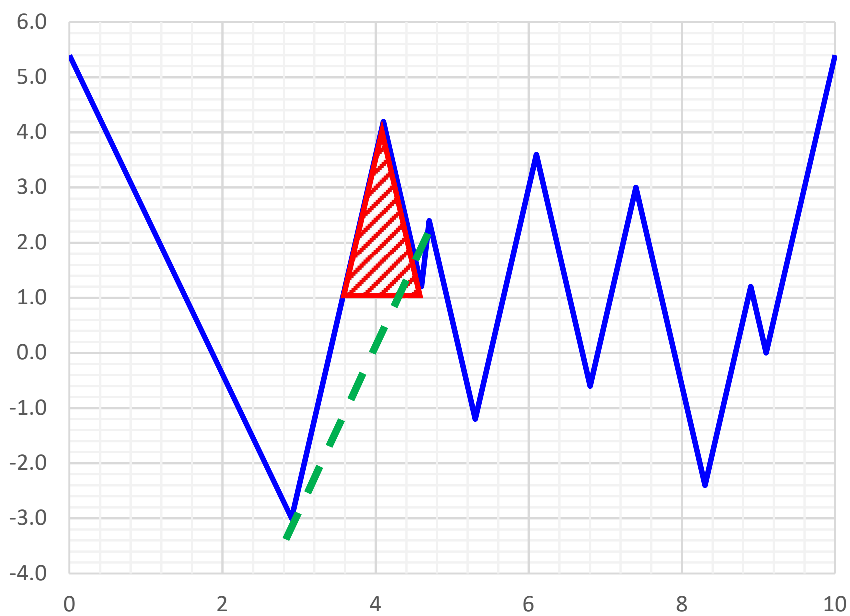


Figure 3.19(b) Extracted cycle from -4.2 to 2.6

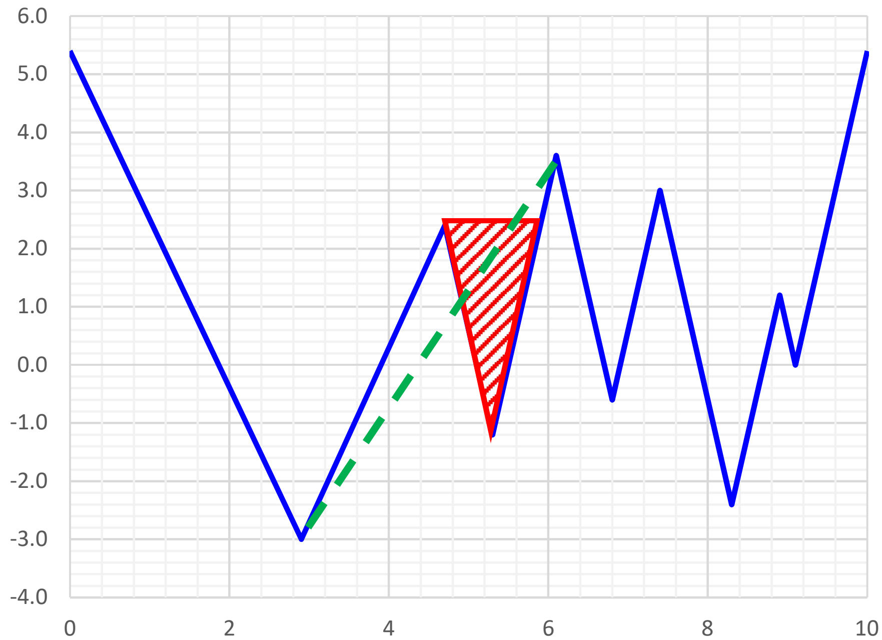


Figure 3.19(c) Extracted cycle from 2.4 to -1.2

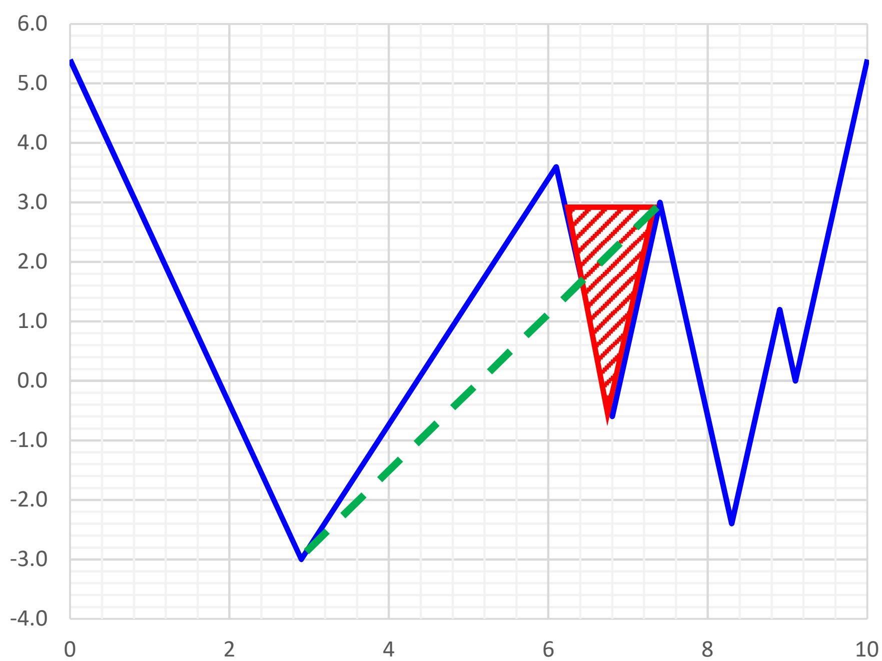


Figure 3.19(d) Extracted cycle from 3.6 to -0.6

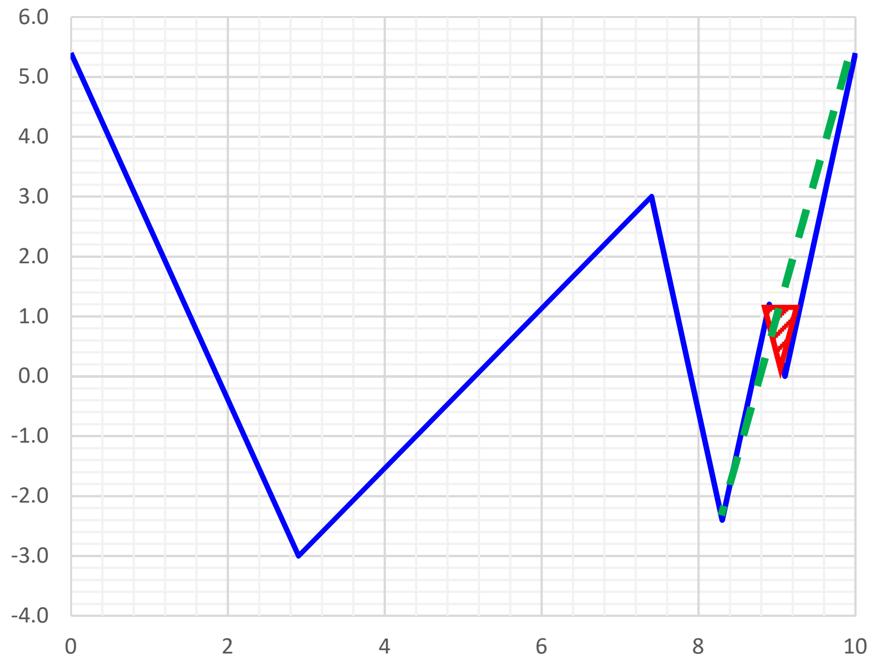


Figure 3.19(e) Extracted cycle from 1.2 to -0.0

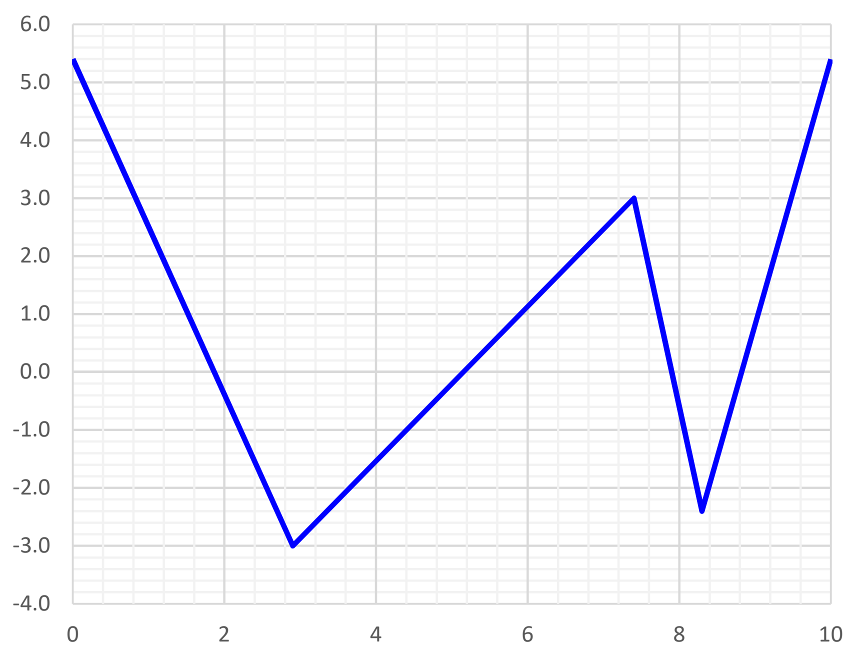


Figure 3.19(f) Residue signal


Figure 3.20 Double residue signal

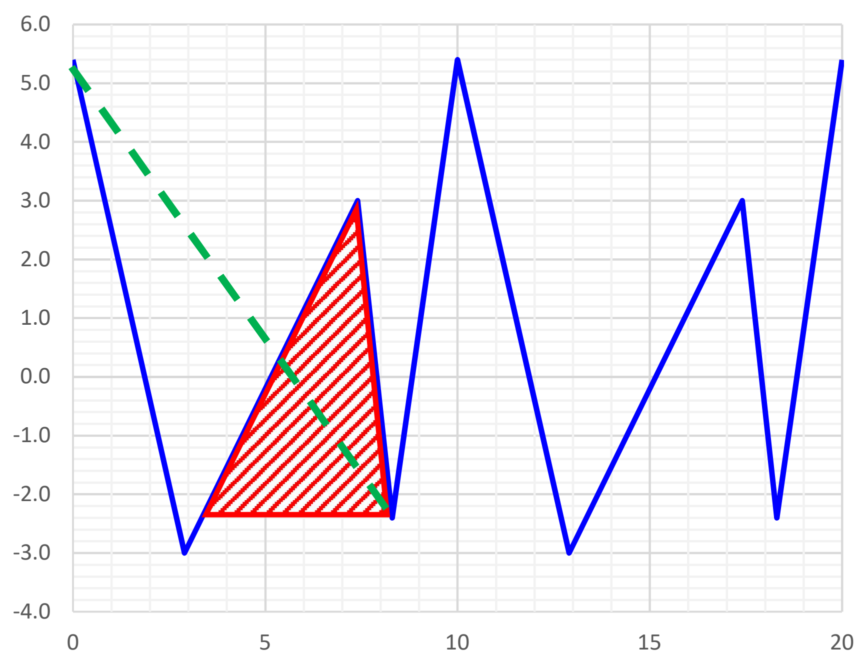


Figure 3.20(a) Extracted cycle from -3.0 to 3.0

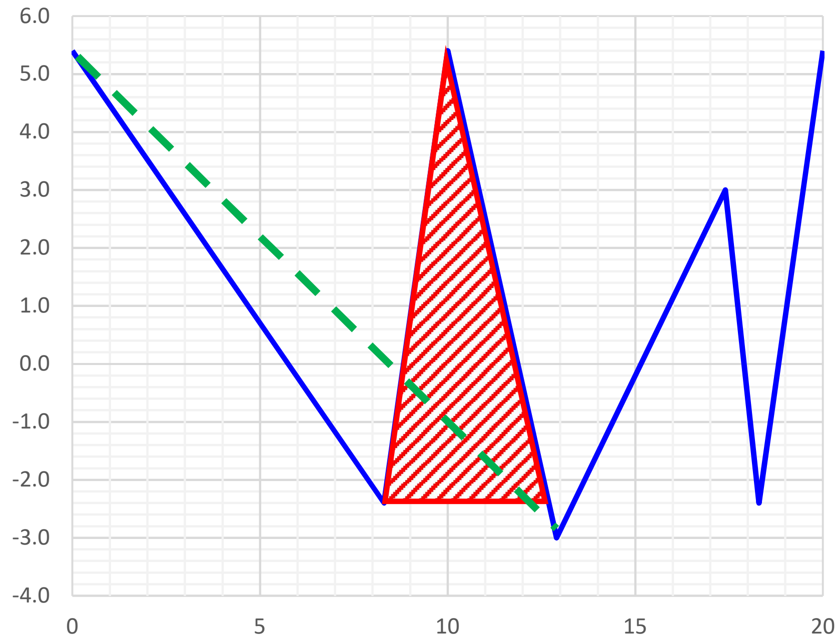


Figure 3.20(b) Extracted cycle from -2.4 to 5.4

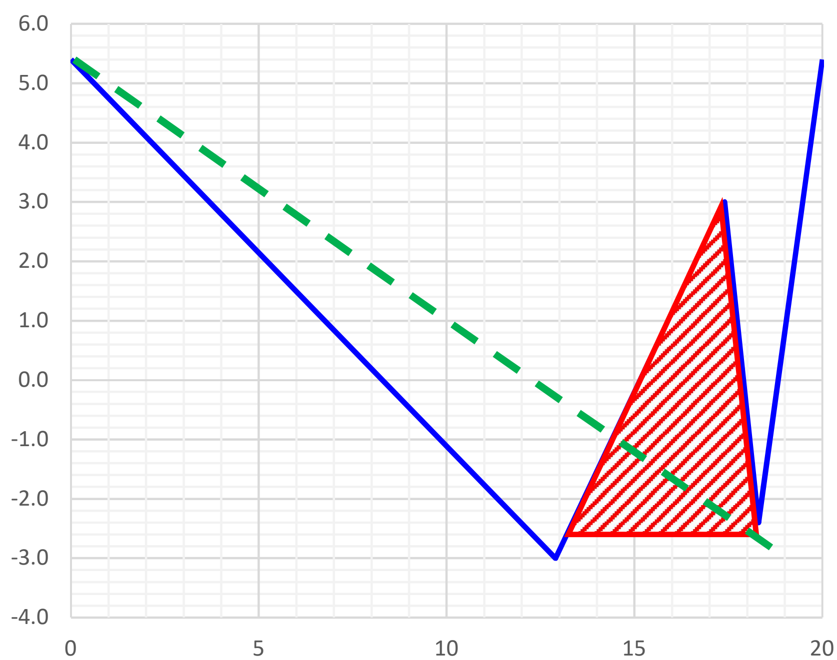


Figure 3.20(c) Extracted cycle from -3.0 to 3.0

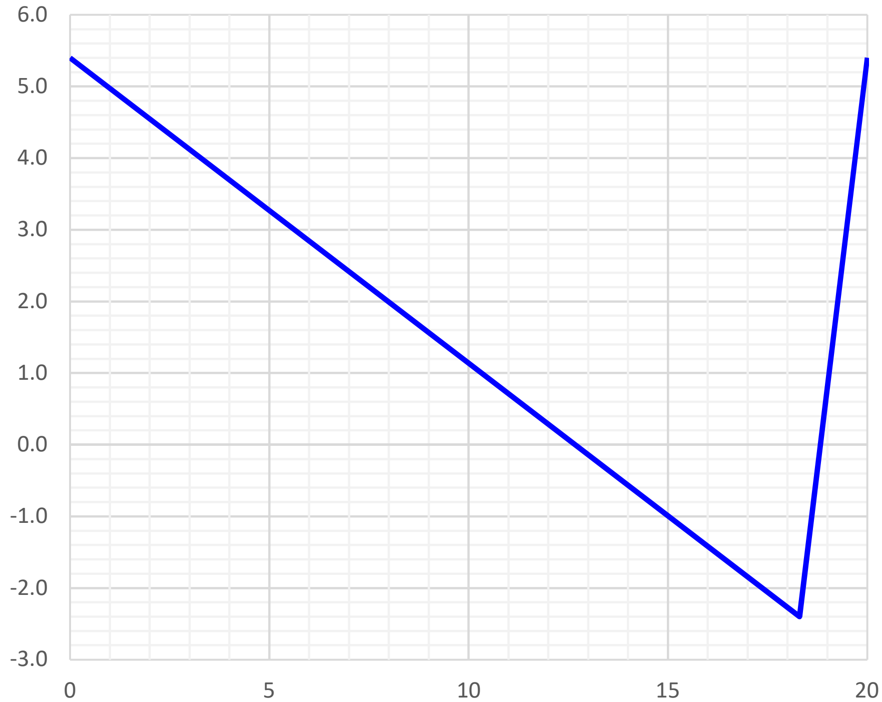


Figure 3.21 Remaining last three points

3.5.2 Peak Picking

To predict the life of a component subjected to a variable load history, cycle counting methods are applied to reduce the complex history into a number of events that can be compared to the available constant amplitude test data [18]. The conventional rainflow algorithms do not need however, all data points of the discretized signal. Instead, they use only the signal extreme points (peaks and valleys). Thus, before we use the rainflow algorithm, a "peak picking" algorithm is run to identify all peaks and valleys and form a synthetic signal by simply connecting subsequent peaks and valleys (as well as valleys and peaks) with a straight line. The hypothetical example of Figure 3.9 shows such a synthetic signal after peak picking.

To identify the peaks and valleys, we simply scan the discretized signal using three points at a time. If the value of the middle point is the maximum (minimum) among the three, the point corresponds to a peak (valley). Figure 3.22 shows a schematic of a hypothetical signal where all peaks (points 1 and 15) and valleys (points 9 and 21) are identified.

Table 3.1 Tabulated results from peak-valley counting

| Peaks/Valleys | Counts |
|---|---|
| -3.0 | 2 |
| 1.2 | 1 |
| 1.8 | 1 |
| 2.4 | 1 |
| 3.6 | 1 |
| 4.2 | 1 |
| 5.4 | 1 |

Table 3.2 Tabulated results using from - to counting matrix

| | | To | | | | | | | | | | | |
|---|---|---|---|---|---|---|---|---|---|---|---|---|---|
| | | -3.0 | -2.4 | -1.2 | -0.6 | 0.0 | 1.2 | 1.8 | 2.4 | 3.0 | 3.6 | 4.2 | 5.4 |
| From | -3.0 | | | | | | | 1 | | 2 | | | |
| | -2.4 | | | | | | | | | | | | |
| | -1.2 | | | | | | | | | | | | |
| | -0.6 | | | | | | | | | | | | |
| | -0.0 | | | | | | | | | | | | |
| | 1.2 | | | | | 1 | | | | | | | |
| | 1.8 | | | | | | | | | | | | |
| | 2.4 | | | 1 | | | | | | | | | 1 |
| | 3.0 | | | | | | | | | | | | |
| | 3.6 | | | | 1 | | | | | | | | |
| | 4.2 | | | | | | 1 | | | | | | |
| | 5.4 | | | | | | | | | | | | |

### 3.5.3 Variable Amplitude Loading Block

The road a vehicle is driven on provides a variable load history which is captured using proper instrumentation. Because the actual road profile for a particular vehicle is unknown, a test profile is obtained by running the vehicle over a test track. The time history of the load is very distinct for different testing profiles such as Belgian blocks, smooth road, etc.

With modern data acquisition systems, the sampling rate is very high resulting in thousands of discrete points per second for a profile. Even if the event for a profile is only 10 seconds long for example, the data acquisition system may record somewhere between 20,000 to 100,000 data points.

Figure 3.23 shows data points from two repeated events. It is common practice to repeat a similar signal many times to represent a certain number of miles, assuming a known vehicle speed, the durability test must be performed on. This assumes that the repeated signal is stationary and long enough to capture the stationary behavior.

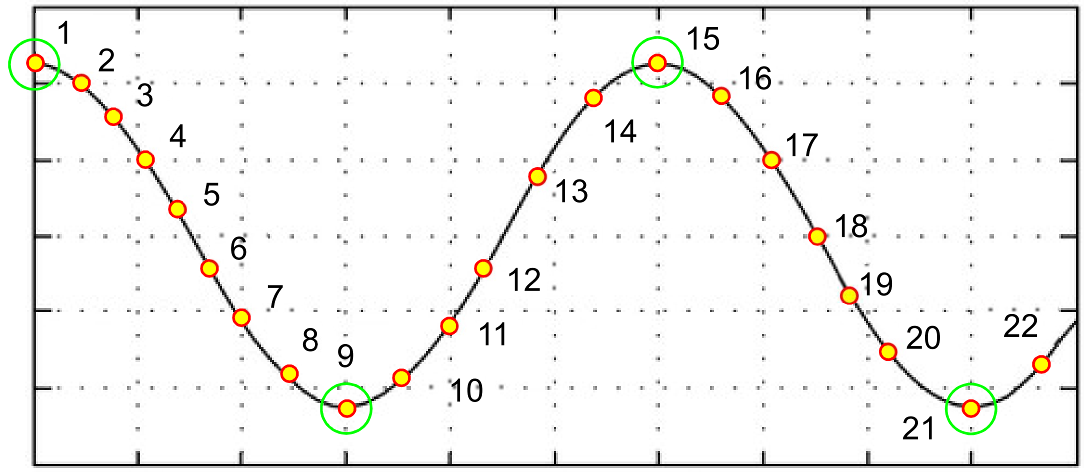


Figure 3.22 Schematic of peak picking

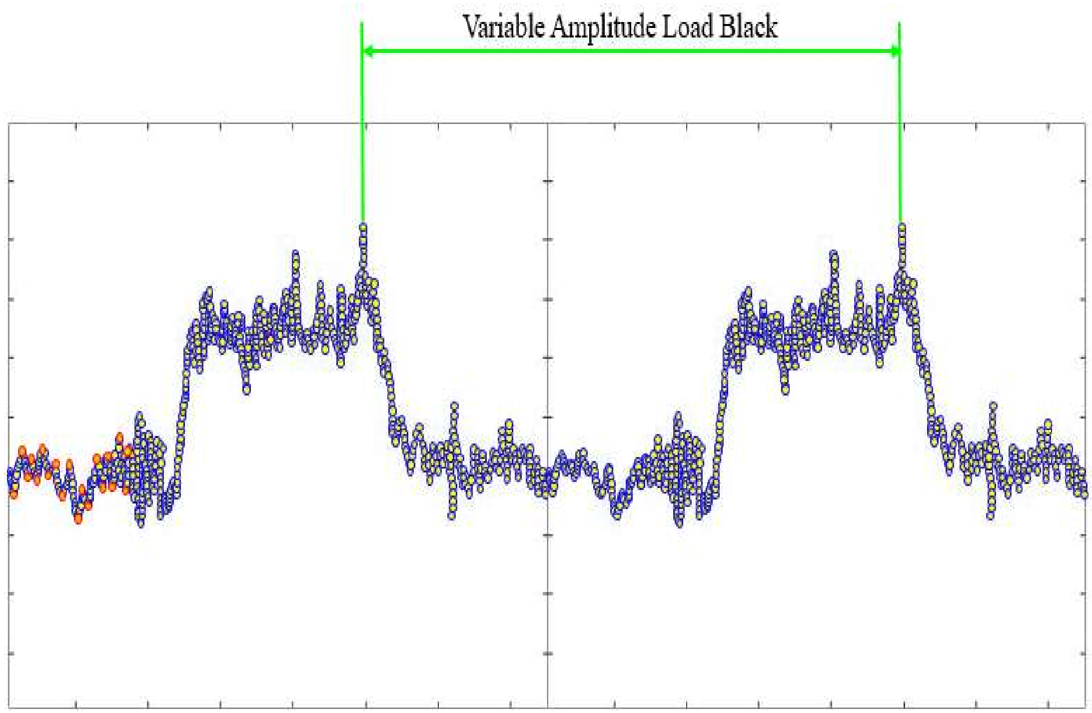


Figure 3.23 Variable amplitude load block

# CHAPTER FOUR

# PHYSICAL SIMULATION

Physical simulation of vehicles and components involves the exact reproduction of the thermal and mechanical processes in the laboratory that the material is subjected to in the actual fabrication or end use. The full vehicle or a component of it can be used in the simulation following the same thermal and mechanical profile that it would in the field. Depending on the capabilities of the machine performing the simulation, the results can be extremely useful and the results can be readily transferred from the laboratory to a full-size production process.

A physical simulation test is usually performed on the Shock Test Evaluation Machine (STEM) of Figure 4.1. The STEM is used to determine the ability of shock absorbers or struts to withstand the dynamic stresses produced by transient waveforms. The machine can be utilized to perform testing routines in both durability and performance modes. A key characteristic of the STEM, exemplifying its one-of-a-kind nature, is its ability to achieve a velocity of up to 5 meters per second at 20 kip.

## 4.1 Specimen Setup

In this research we use a HMMWV suspension spring (Figure 4.2) as a demonstration component. It was chosen because the spring experiences failures in the field. On the simulation table of the STEM, a quarter-car fixture was designed and used to restrain the suspension spring. The latter was instrumented with three strain gauges to measure the change of strain over time at critical locations. A load cell was installed

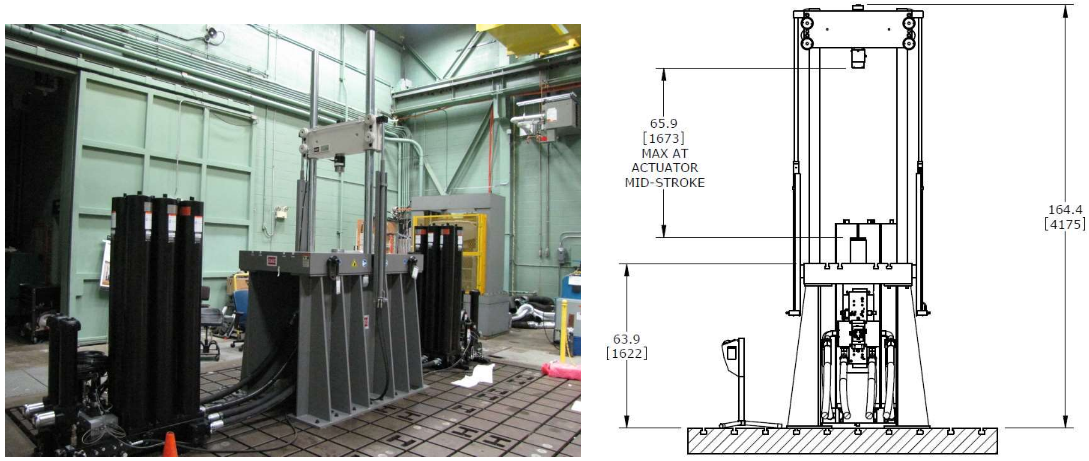


Figure 4.1 Shock Test Evaluation Machine (STEM)

Figure 4.2 HMMWV suspension spring

between the actuator and the spindle of the quarter-car fixture to capture the load history profile. The road profile input was carefully controlled for reproduction purposes.

Below are some basic equations for the coil spring and the calculation of its first natural frequency. The direct shear stress $\tau$ can be calculated as

$$\tau = \frac{F}{A} \tag{4.1}$$

where $F$ is the shear force and $A$ is the cross-sectional area. The torsional shear stress $\tau_T$ is

$$\tau_T = \frac{T\,r}{J} + \frac{F}{A} \tag{4.2}$$

where $T$ is the torque, $r$ is the radius to outer surface and $J$ is the polar second moment of area. If the spring index $C$ is

$$C = \frac{D}{d} \tag{4.3}$$

where $D$ is mean coil diameter and $d$ is wire diameter, the shear correlation factor $K_s$ is

$$K_s = \frac{2C + 1}{2C} \tag{4.4}$$

so that Equation (4.1) becomes

$$\tau = K_s \frac{8FD}{\pi d^3} \tag{4.5}$$

Figure 4.3 shows a schematic of the spring including some of its important quantities.

Based on the HMMWV suspension spring dimension and material properties (Table 4.1), the resonance frequency is

$$f_{res} = \frac{d}{9D^2 n_t}\sqrt{\frac{G}{\rho}} = \frac{0.0325}{9 \cdot 0.1453^2 \cdot 5}\sqrt{\frac{8^{10}}{7650}} = 110.625\ Hz \tag{4.6}$$

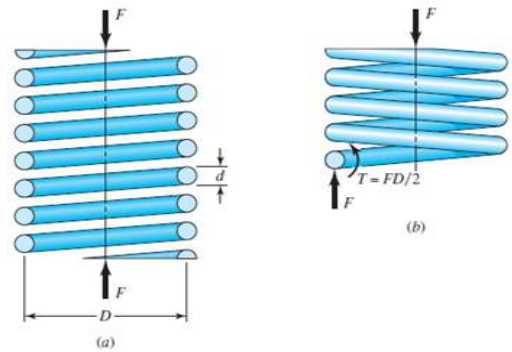


Figure 4.3 Spring definition (a) axially load helical spring (b) free body diagram showing that the wire is subjected to direct shear and torsional shear

Table 4.1 Material properties of the spring

| Property | P355NL1 | Description |
|---|---|---|
| YS | 205.2 | Yield Strength (MPa) |
| UTS | 568 | Ultimate Tensile Strength (MPa) |
| Sf' | 840.5 | Fatigue Strength Coefficient (MPa) |
| b | -0.0808 | Fatigue Strength Exponent |

Figure 4.4 shows the test bench of a quarter car using the coil spring. The test bench is instrumented with:

1. a strain gauge to measure strain on the spring
2. thermocouples to monitor the temperature of the shock which is controlled with an air amplifier for shock cooling
3. a Linear Variable Differential Transformer (LVDT) for spring displacement
4. a LVDT for wheel displacement, and
5. a load cell to measure load on the wheel.

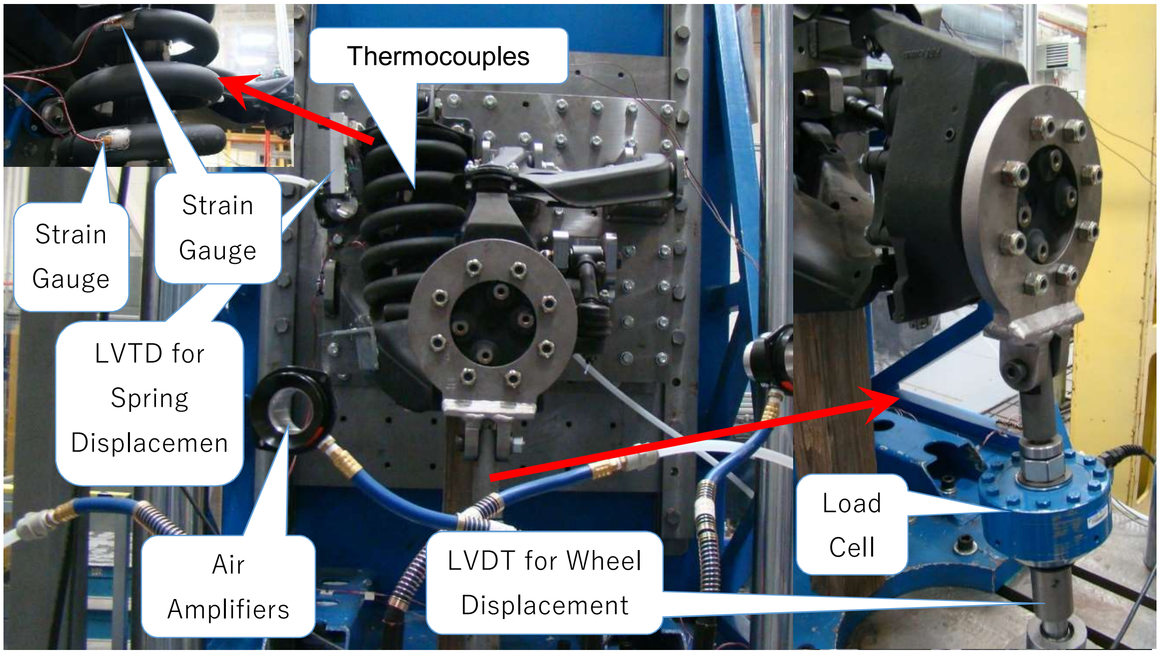

Figure 4.4 Schematic of the test rig for a quarter car

## 4.2 Physical Simulation Process

In order to perform physical simulation (experimental testing) on the test equipment, we follow a six-step process as highlighted in Figure 4.5. Below is a brief overview of the six-step physical simulation process.

**Step #1 - Record Road or Service Data:** In the first step, the simulation input data must be identified and collected (recorded). To record the road data, transducers are placed on the component and/or vehicle at sites different from the locations of input forces. These transducers measure acceleration, strain, or displacement. The field or service history data is measured in either analog FM tape format or digital format. Typically, the number of transducers used for data acquisition exceeds the number of control channels on the simulator because a correlation must be performed in order to properly reproduce the target signal. If a specific vibration profile is of interest, the service data is generated using Matlab or any other software to reproduce the vibration time history profile.

**Step #2 - Transfer, Analyze and Edit Data:** After the data is recorded and digitized, we transfer it to a computer for analysis and editing. During the transfer process, it may be necessary for the data to be converted to a proper format in order to be accepted by the software used in data analysis. The latter is performed in order to identify if the recorded data is of proper quality and all channels are synchronized. Subsequently, we edit the data to shorten the test time by removing the time history parts which are not of interest.

Below are some examples of data removal and editing. When a vehicle moves from a particular road course profile to another the data during the transition is removed because it does not represent the specific test course. Any time the vehicle must stop for service or at the specific check point of inspection all relevant data must be removed. We must also look for unrealistic amplitudes indicating spikes.

If a car is equipped with vertical spindle accelerometers, the front wheel must hit the “piece of wood” event before the rear wheel when driving forward. In the event of acceleration and brake, the breaking force and acceleration are considered positive backwards. The brake moment is considered negative for a braking event. Also, it is very important to identify resonances and energy levels at different frequencies and understand their effect on specimen dynamics. Based on the rig capabilities, control modes and frequencies of interest decide what frequency range must be reproduced. Based on this analysis filter settings are determined.

**Step #3 - Measure the system Frequency Response Function (FRF):** The FRF characterizes a linear dynamic system in the frequency domain by providing the magnitude and phase of the response to a unit amplitude input. For a steady-state sinusoidal input, the FRF magnitude describes the ratio of the output amplitude to the input amplitude. The magnitude indicates the "gain" in the vibration system. The objective of generating the FRF is to provide a stable approximation of the test system at each frequency. To accomplish this task, a random signal is generated with a wide spectrum, while remaining as close to the operating range as possible, to approximate the test system at each frequency. The response information is used to calculate the system model.

**Step #4 - Estimate/calculate the initial drive signal:** In this step, we use the experimentally obtained system model from Step 3 and the desired (target) response time history from Step 2 to estimate an initial drive signal.

**Step #5 – Obtain drive signal iteratively:** Because the test system which includes the mechanical fixturing, hydraulics, and test specimen is in general nonlinear and may have some inherent cross coupling, a suitable drive signal is achieved using an iterative process. We repeatedly measure the error between the actual and the desired time history responses and use this information to correct subsequent drive files. The result is a drive signal that produces the desired response when used to command the test system.

**Step #6 - Test for durability:** The drive signal representing the road surface defines the entire durability test. Multiple drive files can be created to define the test and for building nested sequences. For example, if the system needs more cooling when playing out a file, we can set up digital output channels to turn cooling on and off. Then, at the beginning of the file, we can turn on cooling, and at the beginning of the next file, we can turn off cooling.

In this research, we did not use real road profile data from the field. Instead, a signal was generated from a Gaussian random process with a specified Power Spectral Density (PSD). The signal was imported in the "RPC Pro" simulation tool and was configured for simulation. The "Analyze Pro" application of "RPC Pro" provides all necessary features to analyze and edit profile data. With a capability to view the time history of individual channel recordings and generate a histogram of the data using available standard plotters we checked if the data used was what was intended. In this research, we used five different profiles with identical amplitude and RMS values. By displaying multiple time histories simultaneously, we were able to obtain the correlation between profiles.

## 4.3 Measurement of System FRF

It is important to check for sharp reversals in phase or amplitude which indicate a system (or specimen) resonance or an insensitive transducer to input at those frequencies or amplitudes. This can be achieved by exciting the specimen through the frequency in question and visually checking for unusual motion and/or transducer problems. (Figure 4.6).

The effect of noise must be also considered (Figure 4.7). Its presence in the FRF can indicate a number of conditions including backlash and loose bolts or fittings. If the noise is predominantly of high frequency, reshaping the white noise drive with a smaller exponent value usually reduces it.

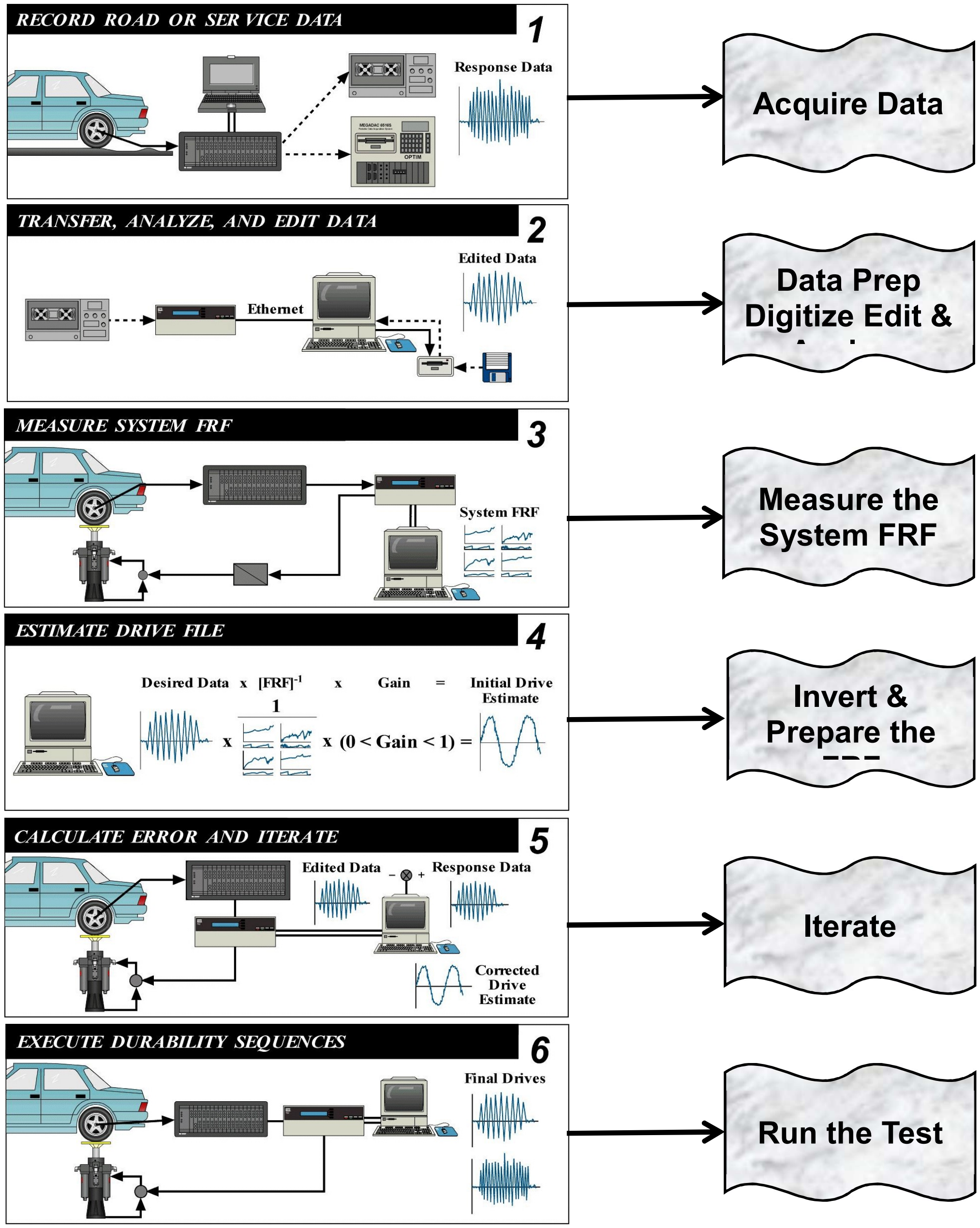


Figure 4.5 Overview of physical simulation process

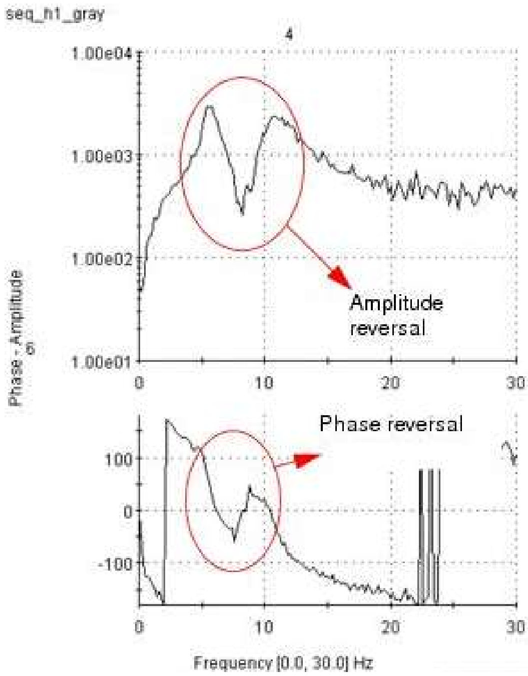


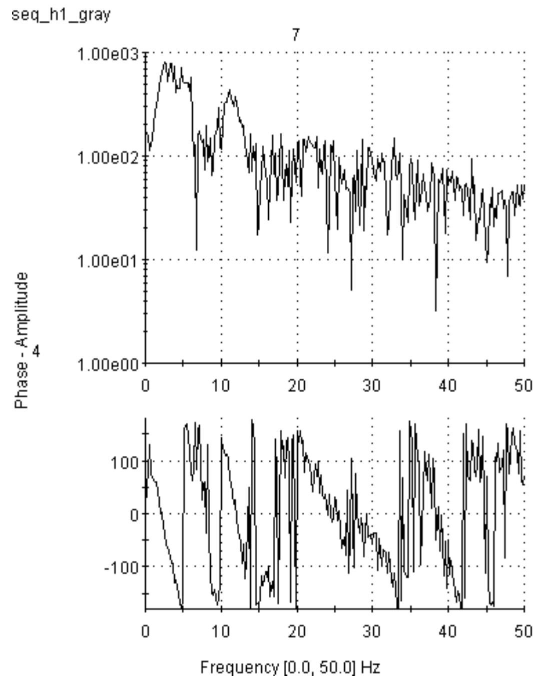


Figure 4.6 Sharp reversal in phase

Figure 4.7 Noise effect from loose bolts

Transducer polarities can be verified by examining the FRF phase at the DC frequency line (Figure 4.8). If the test system applies a positive load into the test specimen, and the phase is zero at the DC line, then the transducer polarity is also positive. If the FRF is 180 degrees at the DC frequency line, then the transducer reads negative as the load is applied.

FRF elements for similar transducers and transducer locations should also have similar amplitude and phase. For example, the vertical acceleration transducers should look similar for the left and right side of the test system (Figure 4.9). FRF data from similar testing can also be useful for comparison. In the case of Figure 4.9 for example, instrument 1 indicates the FRF for the left vertical acceleration channel and instrument 2 indicates the FRF for the right vertical acceleration channel.

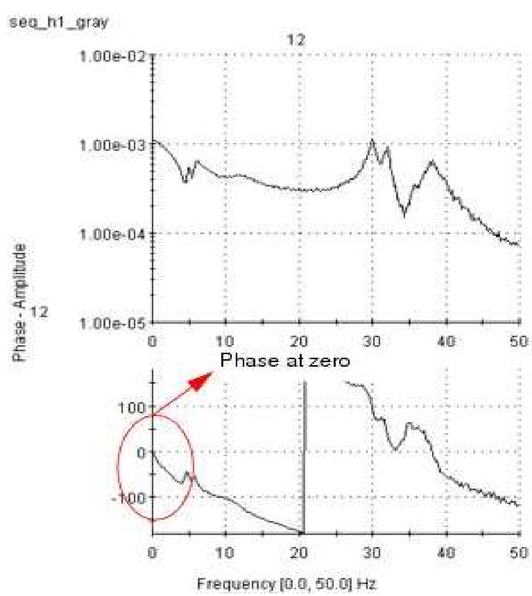


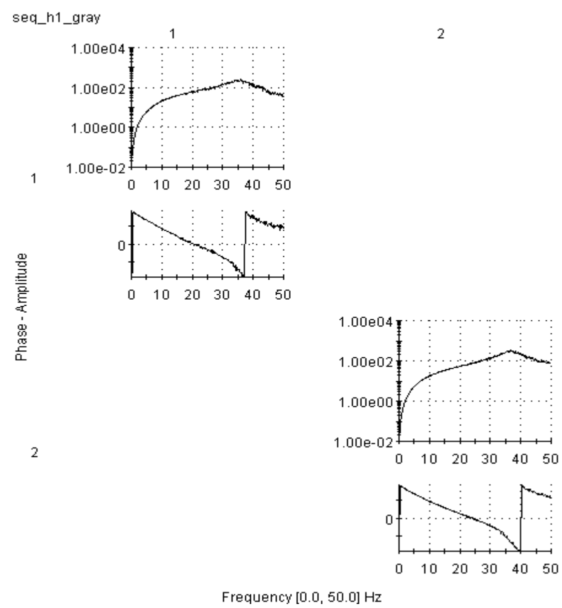


Figure 4.8 Transducer polarities

Figure 4.9 Symmetry test

The coherence bandwidth of the signal should be also checked (Figure 4.10). It represents a statistical measurement of the range of frequencies over which the channel can be considered "flat", or in other words the approximate maximum bandwidth or frequency interval over which two frequencies of a signal are likely to experience comparable or correlated amplitude fading. The partial and multiple coherence of each channel should be high. A recommended value for partial coherence is at least 0.5. A recommended value for multiple coherence is at least 0.7. In the example of Figure 3.10, the partial coherence plot shows a problem at approximately 10 Hz. The multiple coherence plot also shows 10 Hz as a possible problem region.

Inspection of the inverse FRF in addition to the forward FRF, is also very important because singularities which only appear in the inverse FRF, can cause problems. In the example of Figure 4.11, the forward FRF has good characteristics while the inverse FRF is noisy. We must also examine the off diagonal elements of the FRF to determine if there is excessive crosstalk between various drive and response channels. Crosstalk can be also indicated in the time history response. In the example of Figure 4.12, two channels of a sequential FRF time history response are shown. At the top plot, there is minimal crosstalk (very little content other than for the channel being excited). The second channel shows a noticeable increase in crosstalk.

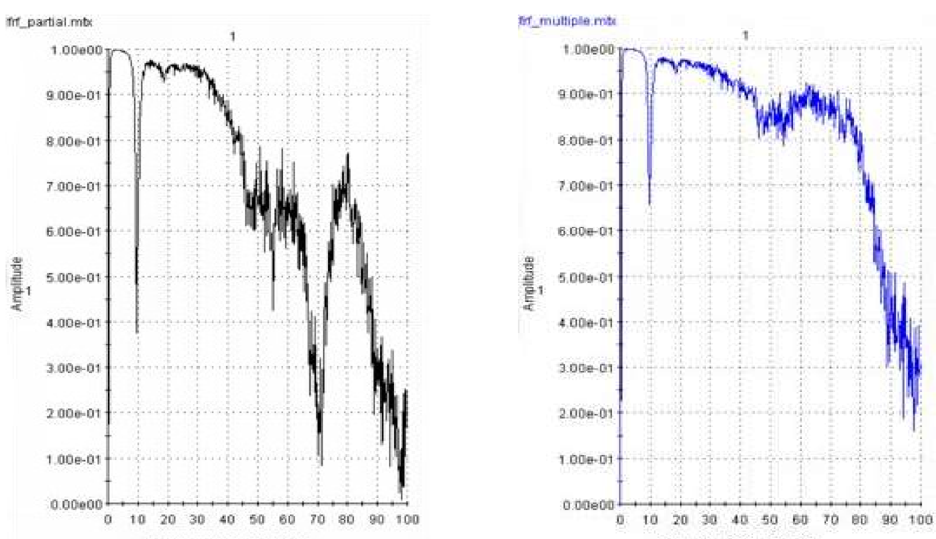


Figure 4.10 Coherence

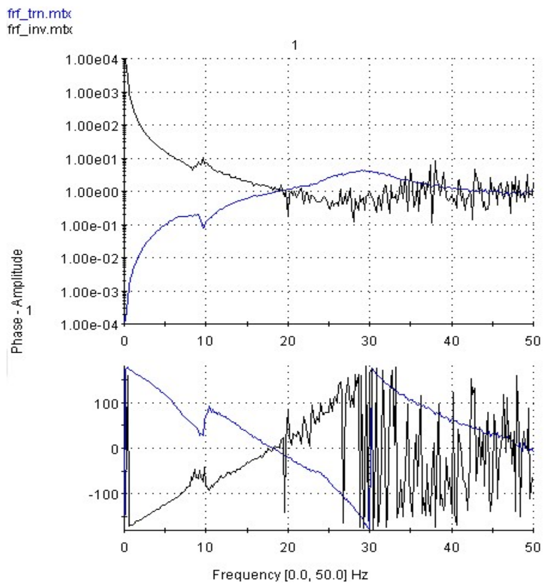


Figure 4.11 Inverse FRF

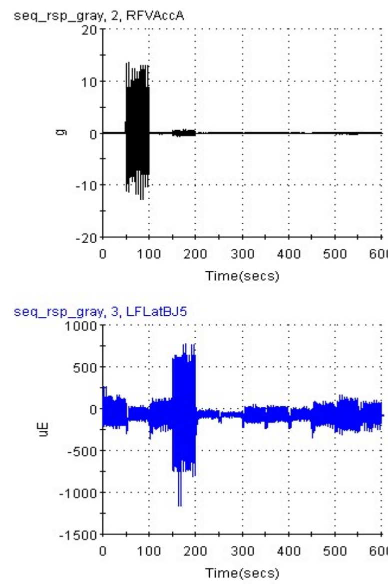


Figure 4.12 Crosstalk

## 4.3.1 Estimation / Calculation of Initial Drive Signal

The estimation (calculation) of the initial drive signal is performed by multiplying the inverted FRF from the system model with the response time history. The resulting signal is the initial drive signal for the iteration process. Multiplication is a technique that takes a time-varying signal and plays it through the FRF mathematically. The resulting signal, with specified gain values applied, is the initial drive estimate (initial drive signal/file) (Figure 4.13).

| | | | | | | |
|---|---|---|---|---|---|---|
| Desired Data | **X** | inverted FRF | **X** | Gain | = | Initial Drive Estimate |

Figure 4.13 Calculation of the initial drive signal

The first drive can also be called the linear drive estimate. It is based on the inverted linear FRF and the desired response data. If the system is perfectly linear, and we use a gain of one, the linear drive estimate would give the correct response. However, all systems have some amount of nonlinearity. Because the linear estimate is an initial guess, the drive must be modified during iterations to get the correct response from the rig.

4.3.2 Iteration Process

Because the test system is nonlinear and may have some inherent cross correlation, iterations must be performed until a desired drive signal is achieved. The iteration process repeatedly measures the error between the actual and the desired time history responses and uses this information to correct subsequent drive files. The result is a drive signal that produces the desired response when used to command the test system. Figure 4.14 shows an overview of the iteration process. The steps below are followed:

1. The initial drive estimate is executed on the simulator and the achieved response is collected (recorded). The system response is usually called the achieved response. During iterations, the data acquisition system sends out the linear drive estimate and at the same time, automatically collects the response from the rig.
2. The response error is calculated. The difference between the desired and the achieved response is calculated by subtracting the achieved from the desired.
3. A drive correction is calculated. The response error and the inverted FRF are used to calculate a correction for the drive signal. The error signal is multiplied by a gain before the drive correction is calculated. The iteration

may become unstable if too much error is used. For this reason, the gain is usually less than 1.0.

4. The drive estimate is modified by adding the correction to the initial drive estimate.
5. Iterations are repeated until the desired drive signal is achieved. To avoid damaging the test system, the maximum amplitudes of each new drive file must be checked before sending it to the test system.

| | | | | | | | | |
|---|---|---|---|---|---|---|---|---|
| Desired Data [G's] | - | Recorded Responses [G's] | = | Error | X | (GAIN:0-1) | = | Corrected Drive Estimate |

Figure 4.14 Iteration Process

4.3.2.1 Tools for Convergence

The RMS of the error signal is the most common tool to judge about the convergence of iterations. It indicates how large the difference is between the desired and achieved responses. If the iterations are converging, the RMS of the error signal becomes smaller and smaller. Note that the RMS does not indicate where the error is occurring or how severe it is.

The RMS of the error signal will be the same if the desired and achieved responses do not match around zero or around maximum peaks. An RMS plot as function of number of iterations shows how well the system is converging and is helpful when selecting iteration gains. An optimal gain gives a fast convergence. If the gain is too high, the iterations converge fast, but the response becomes unstable and the iterations start to diverge. It is important to use gains that give the same convergence for all channels. At the end of the iterations, the RMS error stabilizes at a value, and we observe very little change from one iteration to the next. An increasing RMS from the error signal shows that the iterations diverge. One reason for divergence can be that the gain is too high, but there can also be other factors.

If there are problems during iterations, the auto-spectral density of the error signal can indicate the problem frequencies. Problem frequencies can also be identified by overlaying the desired and achieved auto-spectral densities.

A peak error occurs when the desired and achieved responses do not match at a peak amplitude (Figure 4.15). A peak error at a high peak amplitude is the most severe type of error. Peak errors at noise levels are not very severe. A phase error occurs when the time of a peak in the desired and the corresponding peak in the achieved data are off. Phase errors give very high error signals but are normally not very severe. Normally, a phase error is acceptable if the peak values are the same for the desired and achieved signals. The maximum amplitude error of the signal is normally a phase error. Peak errors at low amplitudes are normally due to noise in the system and are very difficult to remove. When displaying the data, we must be aware of automatic scaling. As we zoom in on a section of data, the scale at which the data is displayed can change. If the comparison looks bad, it may be because we are looking at low amplitude data.

A comparison of the auto-spectral density (ASD) of error signals between the desired signal and the current iteration signal can identify the frequencies where divergence occurs (Figures 4.16 and 4.17). The ASD for the filtered error shows the error within a control region. The ASD for the unfiltered error signal shows both the error outside the control region and the error within the region. To calculate the unfiltered error, we use the unfiltered desired response and the achieved response. The cause of the error outside of control region can either be that the desired signal has data outside the control region or that the system creates a lot of high frequency noise in the achieved response. Errors outside the control region do not reduce by performing more iterations. In this case, we must change the size of the control region and then perform more iterations.

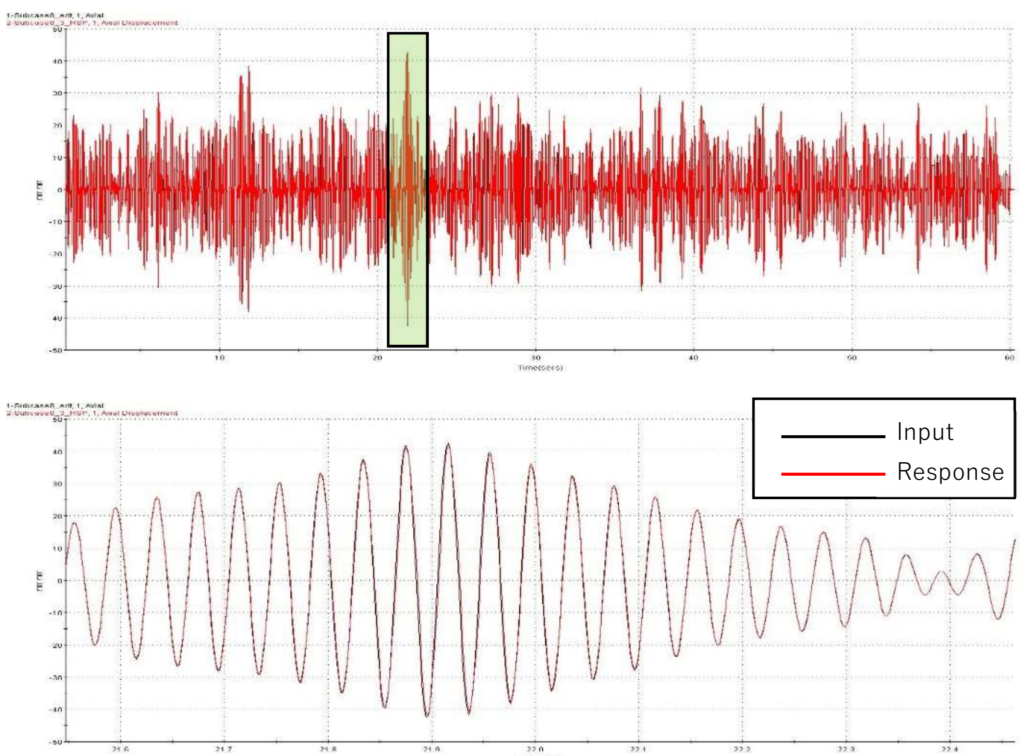


Figure 4.15 Error of the signal (time history signal)

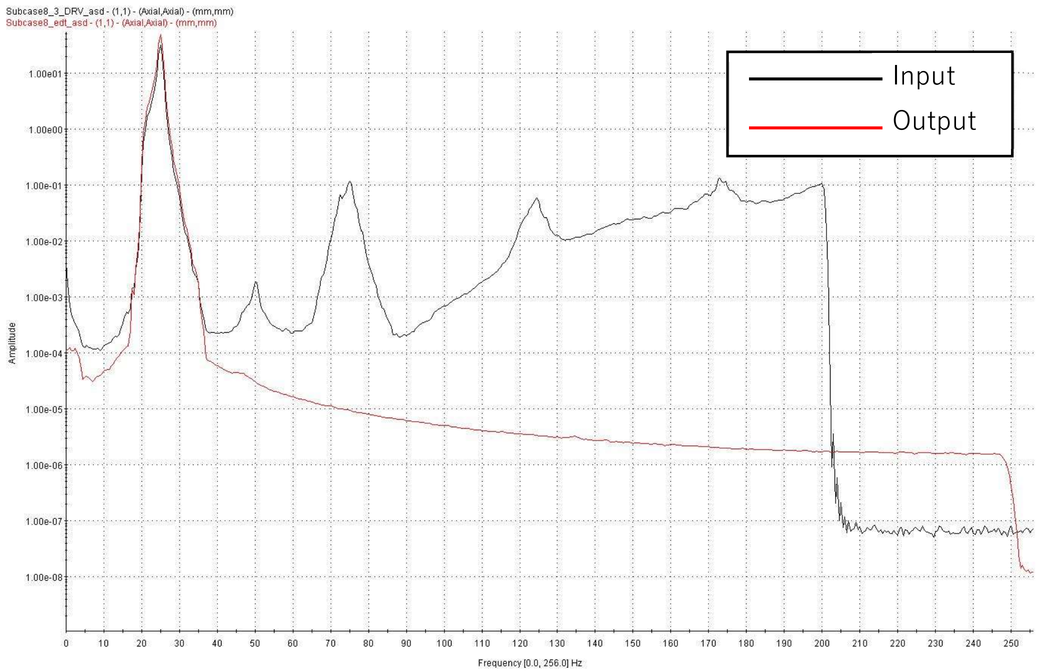


Figure 4.16 Error of the signal PSD (input vs output)

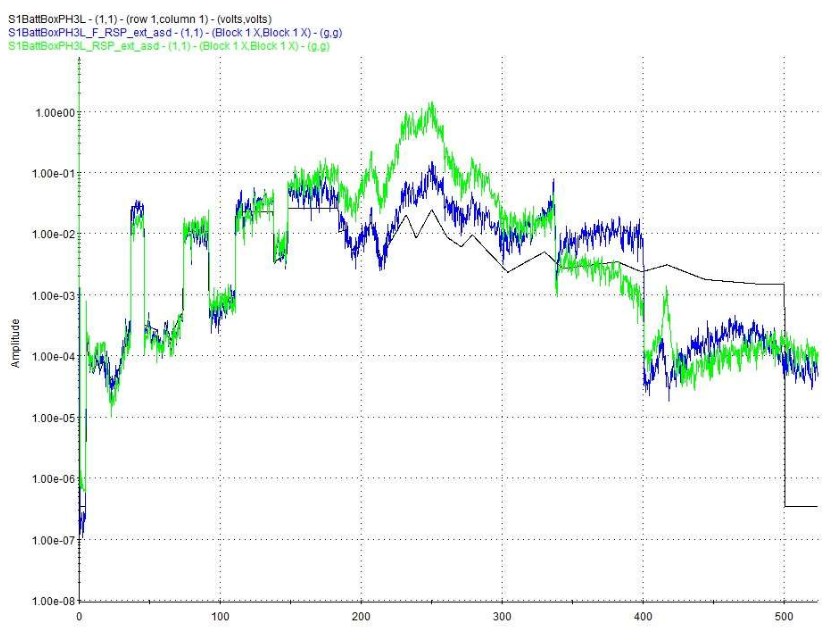


Figure 4.17 Overlaying plot of desired and achieved responses

#### 4.3.2.2 Sources of Implementation Problems

Commonly the transducers can cause problems in several ways since they may have been incorrectly identified. For example, a lateral transducer might be used as a longitudinal transducer providing unrealistic loads to the vehicle. A transducer location may not be optimal if placed for example at a vibrating node or may be susceptible to inputs other than the road (e.g. engine vibration). A transducer can be damaged during iterations and start to drop out. This results in spikes in the response. It should be noted that the transducers should be calibrated to known loads. If they are not calibrated and become damaged, we cannot replace them. A transducer may have problems that are not obvious from an FRF such as hysteresis or nonlinearity issues.

Another set of problems relate to cables which can be damaged during iterations and start providing drop outs. It is important to tie the cables down to make sure that they are not damaged when running the rig. When replacing cables, it is important to check the phase of the new and old cable. If they do not have the same phase, the response signal becomes inverted.

During iterations and durability tests, shock absorbers must be cooled. Otherwise, they overheat. The additional heat damages the shock absorbers, and the damage alters the dynamic behavior of the test specimen. Even if the shock absorbers are not damaged, the higher oil temperature affects the dynamic behavior of the test specimen. Additionally, overheated shock absorbers can explode, spraying hot oil around the rig.

The editing process can also create physically unrealizable data. Normally, to allow the system to finish ringing, some signal is left after a high amplitude event. A symptom of physically unrealizable data can be convergence problems with events very close to the beginning or the end of the file.

# CHAPTER FIVE

# CURRENT DURABILITY TIME REDUCTION METHODS

This Chapter presents a recent methodology adapted and implemented at the US Army's Ground Vehicle Systems Center (GVSC) to compress a test across an entire durability test schedule [64]. The methodology is the current state-of-the-art in the automotive sector (both commercial and military). The aim of this dissertation is to develop a new durability methodology to further improve the accuracy and efficiency of the state-of-the-art method.

## 5.1 Background and Motivation

As the automotive industry and the US Army develops and upgrades its ground vehicle fleet, reliability is a key driver for design and manufacturing processes. Traditionally, reliability metrics are quantified as requirements which the vehicle developer is expected to meet. The Army's Test & Evaluation (T&E) community then tests a set of these vehicles to confirm that the reliability metrics are met [65]. If they are not met, the T&E product team, Program Manager (PM) and contractor enter into a process of test-fix-test commonly referred to as reliability growth [66]. Standard processes usually fall into two categories, Developmental Test (DT) and Operational Test (OT) [65]. This work primarily addresses DT which is focused on confirming that technical requirements are met.

For reliability, a durability schedule is normally derived from the Operational Mode Summary/Mission Profile (OMS/ MP) which specifies the mixture of terrains on which the vehicle is expected to operate. An example of such a specification would be

40% primary roads, 30% secondary roads, 30% trails & cross-country. Additionally, an annual usage in terms of mileage is provided which is then extrapolated to a lifetime estimate that varies from 6,000 miles to 20,000 miles depending on the vehicle. These specifications are normally decomposed by the test community by mapping these terrain types to particular courses at a proving ground at particular speeds. Note that one terrain type may be further represented by multiple proving ground courses.

Both the Ground Vehicle Systems Center (GVSC) and Aberdeen Test Center (ATC) have been investing in laboratory facilities to perform durability and reliability testing in a laboratory environment [66-70]. Figure 5.1 shows the N-post simulator and Figure 5.2 shows the Vehicle Durability Simulator (VDS). Such testing devices are common in the automotive industry [72-79] and they are used to assist in the design validation of new vehicle models. Advantages of laboratory testing are as follows:

1. Ability to test earlier at a subsystem level
2. Ability to precisely control test inputs
3. Ability to instrument, monitor and inspect
4. Ability to compress and/or accelerate the testing
5. Repeatability of test for design iterations
    a. Disadvantages of laboratory testing are as follows:
6. It does not test the full system, only specific subsystems
7. It does not expose the systems to all environmental effects such as dust, mud, rain, sun, temperature, etc.

As listed among the advantages of laboratory testing is the ability to accelerate and/or compress the test. As laboratory-based durability testing becomes more commonplace in the Army T&E process, GVSC is adapting and customizing industry methods, techniques and tools to compress test duration to make lab testing as attractive as possible.

Figure 5.1 N-post simulator

Figure 5.2 Vehicle durability simulator (VDS)

## 5.2 Test Compression Background

Test compression is about test time reduction. For our purposes we will use the following definition:

> Test compression is a process by which a durability test schedule is shortened in duration to the maximum extent possible by removal of time segments while maintaining a desired portion of the original "severity" for the overall test.

Note that "severity" must be distinguished from actual fatigue damage. Often data acquired for test development do not include strain channels for actual fatigue computation. By “severity” we mean the use of other types of channels (i.e. acceleration, load, displacement, etc.) as generic signals which are analyzed using stress life methods. This is normally referred to as Generic Stress Life (GSL). Also, note that compression as defined here shortens test time only by removing portions of the schedule [67, 80, 81] as opposed to acceleration [82-85] which seeks to further shorten test time by disproportionately adding more severe events, amplifying the amplitudes, or shifting the frequency. For tests which are inertially reacted one must be careful about the manipulation of simulator inputs so that they do not excite unnatural dynamics and so that actual dynamics are excited as they would be in the field. It is for this reason that we are considering segment-based compression methods as opposed to peak-valley, frequency-domain or block cycle methods.

Methods of compression range in complexity. The simplest method of compression is to not test on surfaces which simply do not challenge durability of the test area under focus (e.g. removing paved surface miles from a suspension test). The next approach is to perform editing on an event or file basis. Methods commonly used in industry address compression at the file or event level [67]. One standard approach divides a time history into fixed size segments (i.e. 1 to 5 second chunks) and then performs statistics on each segment which could be RMS, max, min or range. This method is used in industry software packages such as Remote Parameter Control (RPC) among others. There it is often referred to as time-history editing. This process is performed for each channel in a file. The “low” regions for the channels are then aggregated using logical operations such as unions or intersections. These aggregate regions are then deleted and retained severity is assessed using fatigue estimation which is typically performed using rainflow cycle counting and stress-life, strain-life or pseudo-damage techniques. Approaches which employ these or similar techniques may be found in the literature [80].

The approach presented in this Chapter takes a few additional steps to look at time editing from a holistic point of view, namely, it evaluates candidate segments based on a severity score and it also evaluates them with respect to the composition of all the events in a test. The Chapter briefly reviews the durability simulation process and presents the test compression approach.

## 5.3 Durability Simulation Process

To develop a durability test in the laboratory, a number of steps must be completed. A rough process for performing a full-vehicle durability test is as follows:

1. Acquire course data in a Road Load Data Acquisition (RLDA)
2. Import, convert and analyze the data.
3. Select surfaces to represent full test schedule and compute repeats for each surface to add up to the required distance.
4. Edit/compress the surfaces to minimize time and retain a pre-determined amount of damage.
5. Execute drive file development (DFD) for each surface and recompute severity retention.
6. Perform additional DFD or modify repeats to achieve a satisfactory road to lab correlation.
7. Run the test and monitor the results.

The focus of this Chapter is on step 4.

The RLDA normally acquires the following minimum suite of instrumentation:

1. Vertical acceleration for each spindle
2. Suspension displacement for each wheel
3. Vehicle speed
4. Accelerometers mounted on the chassis
5. Strain gages mounted on components of interest

During the RLDA, each course or surface is recorded for multiple passes, sometimes at multiple speeds. The events which are chosen to represent the durability schedule are selected to be typical of the passes over a given terrain. If these events are lengthy, the test engineer may extract a shorter portion to represent the whole course. Experience and engineering judgement is required. These representative events comprise the full set of events from which to extract desired responses for drive file development. Implied in this process is the ergodicity of the recorded laps (i.e. all laps on the proving ground course are represented by the data collected in the RLDA). This method of recording field responses has the advantage that it captures the response of the vehicle to the excitation of the terrain, so it automatically encapsulates all of the dynamics of the vehicle system such as resonances.

After the completion of this process, a baseline durability schedule is established consisting of a set of $N_e$ events represented as time history files. Each of these events has $N_c$ channels for which test compression will be employed (i.e. the event may contain more channels). Each varies in length and we denote the length of each event as $L_j$, where $j = 1, \ldots, N_e$ and each event is repeated $R_j$ times in the durability schedule.

## 5.4 Test Compression Approach

### 5.4.1 Damage Calculation

The first step in this approach is to do cycle counting using the rainflow method. The output of the rainflow method consists of a set of stress ranges along with a number of repetitions which may then be used to compute damage. We cycle through the time history using the following basic algorithm.

1. Find the maximum value and cyclically work through the time history wrapping the end to the beginning.
2. Reduce the time history to a series of peaks and valleys.
3. Rainflow cycle count the peaks and valleys, ignoring any cycles $< \sigma_t$ in range. Here we use ASTM E1049-85, ¶ 5.4.5 [86] with the cyclic assumption.
4. Accumulate the damage using Equations (5.2) and (5.3).

This technique is often applied to channels not normally associated with stress or strain such as acceleration and/or displacement. In these cases, we assume that these signals accrue damage using the same exponential law and accumulation method (i.e. the signals are proportional to forces exerted on or in the system). When this is done, the resulting damage values are not correct in an absolute sense. However, it is generally accepted that they can be used to compare the severity between different segments of a time history and between time histories themselves. When used for this purpose, these values are often referred to as pseudo-damage or just simply severity.

The Generic Stress-Life (GSL) method "characterizes" the cumulative effects of proving ground transducer response signal locations in a manner similar to calculating metal fatigue damage, but without regard to actual metal strain levels. It is assumed that these signals are proportional to force and/or stress. Hence the implied "fatigue damage" in this case is referred to only as "pseudo damage" or simply, "severity".

Specifically for the time compression durability method of this Chapter, a pseudo or Generic Stress-Life fatigue (GSL) curve is constructed for each of the selected transducer signal channels. Existing engineering units such as acceleration $(g's)$, load $(N/lb's)$ or displacements $(mm/in's)$ for example are retained in these cases where metal strain is not actually measured nor is stress calculated. These GSL curves then simply become convenient "Amplitude-Life" curves using the engineering units of many different measured signals. They are only used for comparative purposes and not in any absolute sense.

### 5.4.2 Segment Removal Algorithm

Given the set of $N_e$ events, we compute the total length of the unedited test as

$$L = \sum_{j=1}^{N_e} R_j \, L_j \tag{5.1}$$

Since each channel of each event represents a separate severity value, we can denote the severity of a particular channel as $D_{j,i}$ . We assume that a given channel $i$ is computed with its own unique parameters such as slope, $b_i$, y-intercept, $\sigma_{0,i}$, and threshold, $\sigma_{t,i}$. We can therefore, equitably accumulate severity across multiple events for a given channel using the following relation

$$D_i = \sum_{j=1}^{N_e} R_j \, D_{j,i} \tag{5.2}$$

where $D_i$ is the total accumulated severity across all events for the given channel. We can then determine the relative severity of each event for a given channel as

$$D_{j,i}^{r} = \frac{R_j D_{j,i}}{D_i} \tag{5.3}$$

where $D_{j,i}^{r}$ represents the relative severity attributed to event $j$ for channel $i$. We then have $\sum_{j=1}^{N_e} D_{j,i}^{r} = 1$ representing 100% damage. To proceed with editing, we consider each event being composed of discrete slices of time called segments. Typically a segment is a few seconds long. For time histories represented in RPC III file format [87], it is often the frame size, namely the value of the PTS_PER_ FRAME parameter, which must be one of $\{256, 512, 1024, 2048\}$. Given the sampling interval $\Delta t$ and points in a frame yields the segment size. If the segment size is denoted $t_f$ the number of segments in an event is

$$N_j^f = \frac{L_j}{t_f} \tag{5.4}$$

We then desire to identify segments which contribute little to the overall severity and remove them. To keep track of which segments are to be kept or removed we identify a Boolean vector $I_j \in \mathbb{B}^{N_j^f}$ where $\mathbb{B} = \{F, T\}$ denotes the Boolean set. So for example, a vector, $I_j = \{\boldsymbol{TTT} \ldots \boldsymbol{T}\}$ of length $N_j^f$ denotes that all segments are included in the time history. We will use $I_{j,k}$ to index the $k$th element, if we say that $I_{j,2} = F$ then $I_j = [\boldsymbol{TFT} \ldots \boldsymbol{T}]$. If we desire to compute damage or length of an event considering only those segments for which $\boldsymbol{I}_{j,k} = \boldsymbol{T}$ we will denote that as $D_{j,i}(I_j)$ and $\boldsymbol{L}_j(\boldsymbol{I}_j)$ respectively.

Finally, we will denote the set of all Boolean vectors for all events as the set $I = \{I_1, I_2, I_3, \dots, I_{N_e}\}$.

We may now rigorously express the test compression optimization problem as

$$\min_{I} \sum_{j=1}^{N_e} R_j L_j(I_j) \quad , \quad s.t.\ \frac{1}{N_c} \sum_{i=1}^{N_c} \sum_{j=1}^{N_e} \frac{R_j D_{j,i}(I_j)}{D_i} \geq D_{min} \tag{5.5}$$

where $D_{min}$ is the minimum retained average relative damage (i.e. this value would be set to 0.9 to retain 90% average damage). Although this optimization appears linear, the $D_{j,i}$ (•) function depends on highly non-linear computations including rainflow cycle counting, S-N curves, and Miner's Rule.

The solution of the optimization problem (5.5), has two elements, the first is the identification of segments to remove and the second is the computation of the retained damage. While most fatigue editing methods identify non-damaging segments by only considering the data in the segments (i.e. only considering the local 1024 points of the segment), the method employed here uses a subtractive method described as follows. Consider the inclusion set which is all true for the given event j which we will denote as $T_j = [TTT \dots T]$, we will furthermore define a unit Boolean vector $U_{j,k} = [FFF \dots FTF \dots FFF]$ for which the kth element is true and all others are false. Finally, we will denote the logical negation of one of these vectors as an overbar, so for example if $\mathbf{X} = [\boldsymbol{FTF}]$ then $\overline{\mathrm{X}} = [TFT]$. We compute the damage attributed to a given segment as

$$D_{j,i,k} = D_{j,i}(T_i) - D_{j,i}(\overline{U}_{j,k}) \tag{5.6}$$

Namely the damage of the whole time history minus the damage of the time history with that segment removed. These values may be precomputed and even cached for later analyses as the computation of these values can be time consuming.

Based on these segment damage values, we initialize the inclusion vectors to all true, $I_j = T_j$. We then identify a segment to remove based on the following heuristic

$$(j,k) = \underset{\{j,k:\, I_{j,k}=T\}}{\operatorname{argmin}} \frac{1}{N_c}\sum_{i=1}^{N_c} D_{j,i,k} \tag{5.7}$$

Since $D_{j,i,k}$ are all pre-computed, Equation (5.7) is implemented as a simple search for the minimum average damage for each event j and segment $k$. Then if

$$\frac{1}{N_c}\sum_{i=1}^{N_c}\frac{1}{D_i}\sum_{j=1}^{N_e} R_j D_{j,i}\left(I_j \overline{U}_{j,k}\right) \geq D_{min} \tag{4.8}$$

we update $I_j \leftarrow I_j \overline{U}_{j,k}$ and jump to Equation (5.7), otherwise we end the optimization process. This algorithm is summarized in the following steps

1: **precompute** $D_{j,i,k}$ using (Equation 5.6)

2: **initialize** $I_j \leftarrow T_j\,,\ \ j = 1, \dots, N_e$

3: **do**

4: **let** $(j,k) \leftarrow \underset{\{j,k:\, I_{j,k}=T\}}{\operatorname{argmin}} \frac{1}{N_c}\sum_{i=1}^{N_c} D_{j,i,k}$ as in Equation (5.7)

5: **compute** $D_T = \frac{1}{N_c}\sum_{i=1}^{N_c}\frac{1}{D_i}\sum_{j=1}^{N_e} R_j D_{j,i}\left(I_j \overline{U}_{j,k}\right)$ as in Equation (5.8)

6: **if** $D_T < D_{min}$ **break**

7: **let** $I_j \leftarrow I_j \overline{U}_{j,k}$

8: **end do**

9: **output** $I_j, j = 1, \dots, N_e$

Once we are satisfied with the time reduction and damage retention, we remove the segments for which $I_{j,k} = \boldsymbol{D}$. The simplest approach is to stich the retained segments together. However, this creates a discontinuity at the joint, which may cause unrealistic events for the test article or rig. For this reason, we consider two joining approaches which employ a linear fade, one in the deletion region and one in the retention region. These methods are illustrated in Figures 5.3 and 5.4. In Figure 5.3 the blue line on the bottom two segments represents the gain for the transition region. The sum of the two gains is always 1.0. This method does not add time, but may affect amplitudes in the retained regions. Fading in the retained region as shown in Figure 5.3 does not add additional time, but could potentially diminish a peak if it is close to a deleted region. Fading in the deleted region as shown in Figure 5.4 preserves all of the content in the retained regions but adds a small amount of time at each join. In Figure 5.4 the blue line on the bottom two segments represents the gain for the transition region. The sum of the two gains is always 1.0. This method adds time, but will not affect amplitudes in the retained regions.

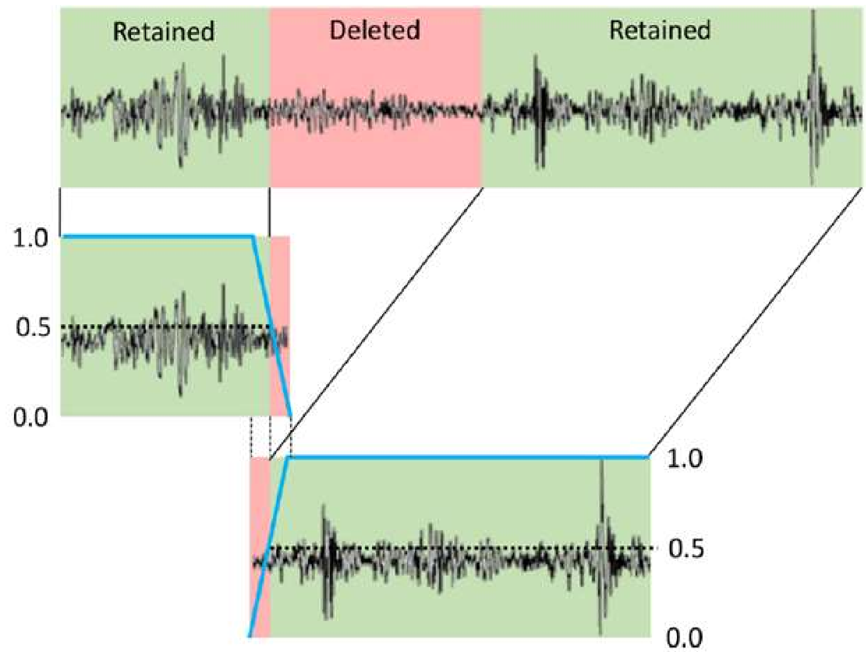


Figure 5.3 Fading technique in retained region

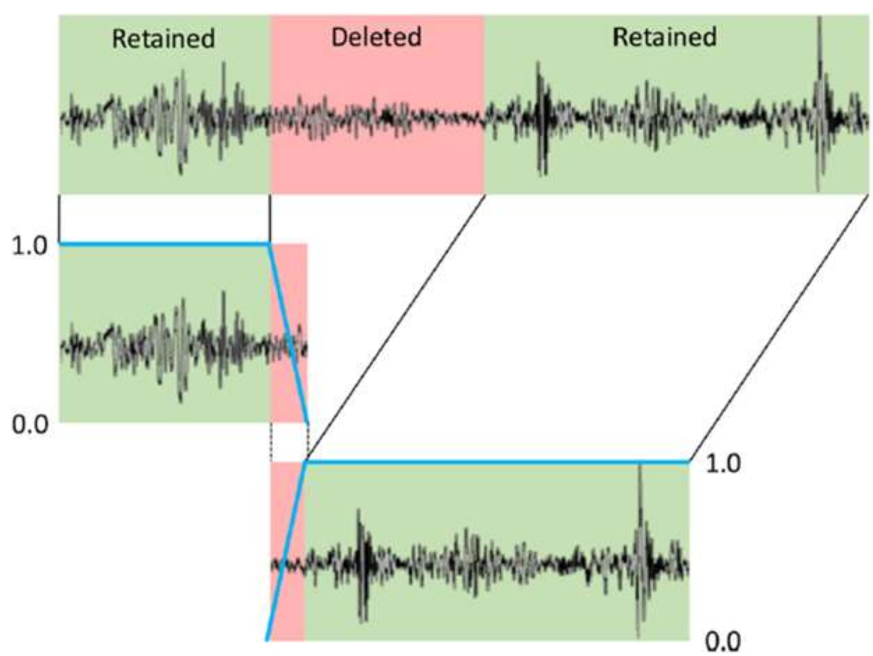


Figure 5.4 Fading technique in deleted region

# CHAPTER SIX

# PROPOSED DURABILITY METHOD AND EXPERIMENTAL VALIDATION

## 6.1 Fatigue Life Estimation Approach

In this research, we implement the life calculation approach of Figure 6.1. In general, the system is excited by a number of random processes. A random process may be viewed as a collection of random variables where the sample points of each random variable are the values of each trajectory of the process at time. The latter varies from zero to a time horizon. Formally, we say a random process $X(t)$ is a mapping of the elements of the sample space into functions of time. Each element of the sample space is associated with a time function as shown in Figure 6.1.

For automotive vehicle applications, a road profile from a proving ground course constitutes the input (excitation) random process. It is expressed as suspension displacement vs time which is calculated using the road elevation in time and vehicle speed. The road elevation is measured for different types of road courses (e.g. gravel, asphalt, off road). The testing equipment (i.e. vehicle or vehicle component) has many random parameters providing a vehicle to vehicle variability. The system output random process is an ensemble of time histories such as suspension displacement, elevation displacement, radial load, strain or stress, shock temperature, etc. Using the recorded (or calculated) output data (trajectories of the output process) we run a fatigue analysis using rainflow counting or Miner's rule for example, to estimate the damage for the system output random process. Using all damage realizations (one for each process trajectory) we can calculate the PDF of fatigue life.

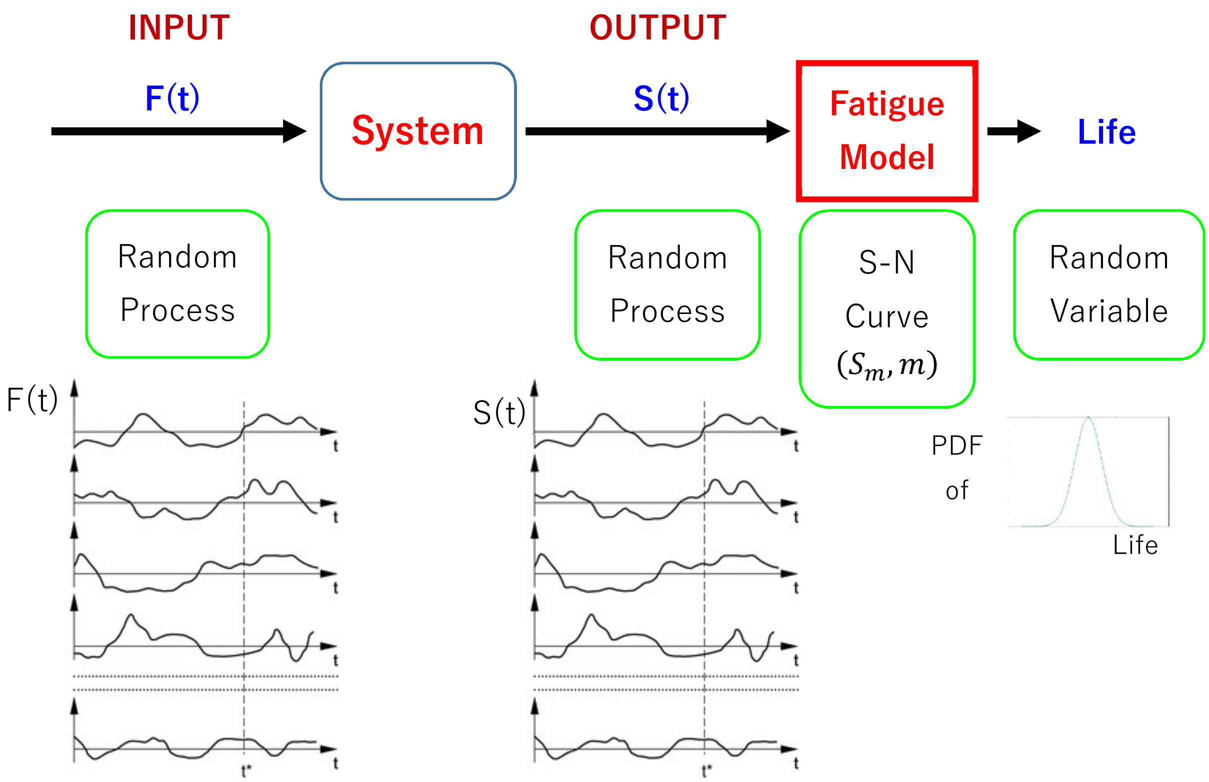


Figure 6.1 Fatigue life estimation approach

## 6.2 Assumptions of Proposed Method

In this research, we consider static problems where the output stress signal is obtained by multiplying the excitation displacement signal (road profile) by a scalar. This is valid if the first natural frequency of the system is much higher than the excitation frequencies of the stress Power Spectral Density (PSD). Therefore, the displacement and stress signals are displaced by a constant amount through time and of course are in phase exhibiting peaks and valleys synchronously. Damage cycle counting can therefore be performed using the input displacement signal instead of the output stress signal (Figure 6.2).

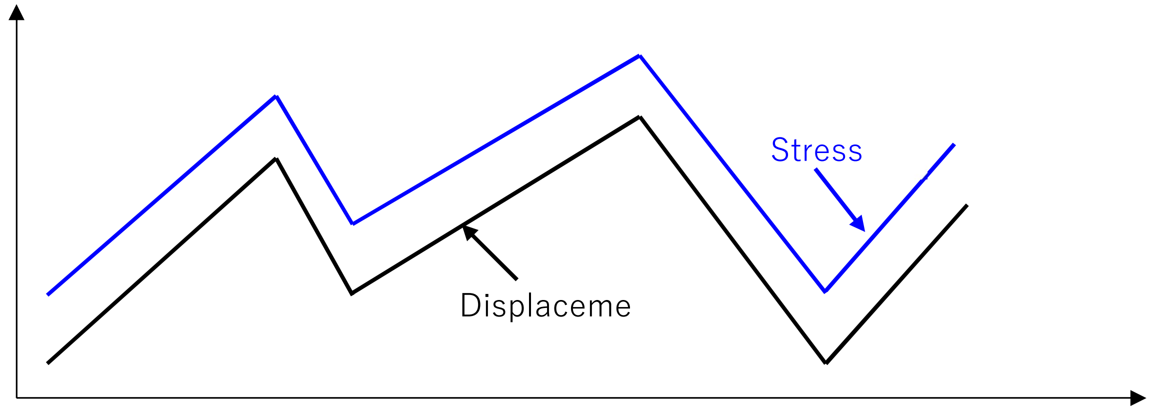


Figure 6.2 Static problem assumption

In the laboratory, strain gauges are placed on a suspension spring and micro-strain is measured at the location of the strain gauges. The strain is then converted to stress using Equation (6.2) and the stress is used in the fatigue life calculation.  Figure 6.3 shows pictorially the conversion of strain to stress.

$$\varepsilon = \frac{\sigma}{E} + \frac{\sigma^{\frac{1}{n\prime}}}{K'} \tag{6.2}$$

where

$\varepsilon = strain$

$\sigma = stress\ (MPa)$

$K' = material\ strength\ coefficient$

$n' = cycle\ strain\ hardening\ exponent$

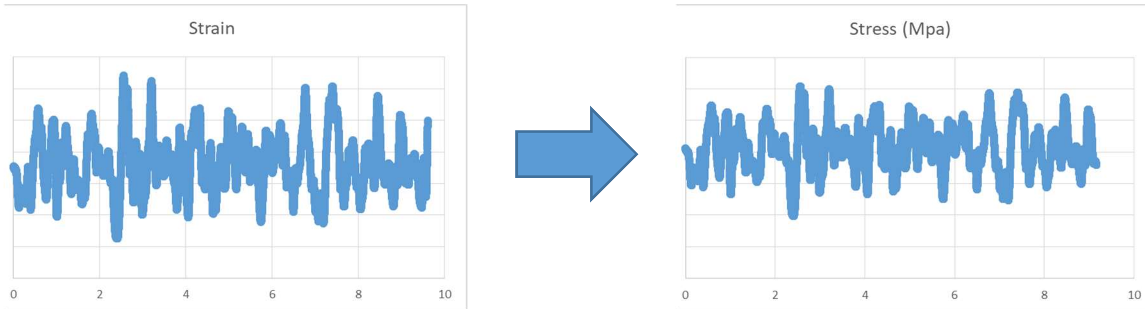


Figure 6.3 Strain to stress conversion

For vibratory problems, the stress signal and the displacement signal are not in phase. In this case, the former can be obtained from the latter for linear systems using a modal model and the concept of modal stresses (stress mode shapes). For that, we need the displacement mode shapes, modal stresses, and the system Frequency Response Function (FRF) for one input-one output system. In this case, cycle counting cannot be performed using the displacement signal instead of the stress signal. Future work will address this case as an extension of the developed static case in this dissertation.

## 6.3 Proposed Durability Test Time Reduction Method

The main steps of the proposed durability testing method are summarized below. First, the experimentally obtained strain signal is converted to a stress signal which is then used to identify all peaks and valleys (local maxima and minima) using a peak picking algorithm. A simplified (synthetic) stress signal connecting peaks to subsequent valleys and valleys to subsequent peaks is then formed and used in the rainflow counting algorithm to calculate all individual damage cycles (i.e. calculate the damage for each identified cycle). Note, that the rainflow algorithm identifies all damage cycles in two phases where the second phase uses a “residue + residue” (double residue) signal. The residue signal is obtained by eliminating all identified cycles in the first phase from the original signal.

The damage values of all cycles are sorted in decreasing order and the $90^{th}$ percentile of the total damage is estimated. Any cycle which does not belong to the estimated $90^{th}$ percentile is removed. After the removal of all “small damage” cycles, a new synthetic signal is formed. We should note that the kept cycles in the synthetic signal are sequenced according to the time they appear in the original signal. This is important because damage accumulation is a nonlinear phenomenon with experimental evidence reported in the literature that it depends on the sequencing of cycles.

The peaks and valleys of the synthetic signal are then <u>equally spaced</u> in the time window of the original signal (e.g. Figure 6.36). This simplifies the synthetic signal reducing the frequency content of its PSD. This step does not affect the damage accumulation of the synthetic signal because the time a cycle occurs does not affect the damage.

The above, equally-spaced synthetic signal is subsequently compressed in time. The time compression reduces the durability test time substantially. The amount of compression is determined so that the PSD of the compressed signal 1) does not exceed the equipment limit PSD provided by the equipment manufacturer, and 2) does not have frequency content exceeding the first natural frequency of the specimen. The second requirement is imposed so that the durability test is static allowing us to determine the stress (output) signal from the excitation displacement signal by multiplication with a scalar.

The compressed signal, called final signal, is used to perform the durability laboratory test. To make sure the durability test is performed until the specimen breaks, the final compressed signal is repeated many times. Figure 6.4 summarizes all steps of the proposed approach to compress the initial signal without substantially altering the total damage.

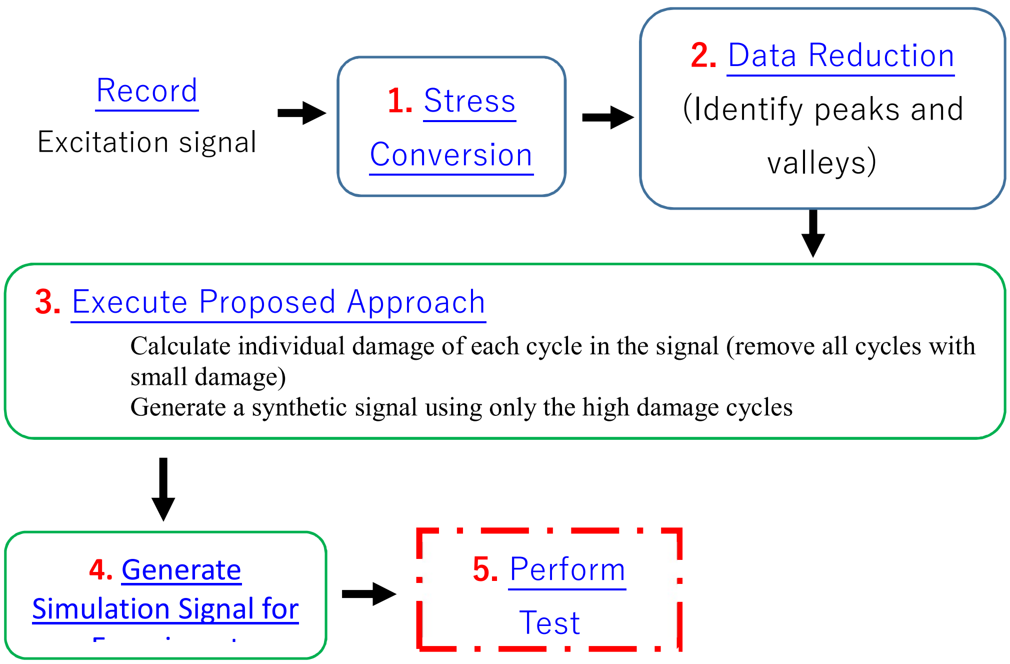


Figure 6.4 Schematic of proposal approach to obtain a compressed signal

We should note, that the estimation of fatigue life depends on the following factors which have the potential to introduce a sizeable variability to the estimation:

1. The fatigue strength coefficient $S_f$ and the fatigue strength exponent $b$ of the used material can alter the fatigue life estimation considerably. Before testing,

we recommend an experimental determination of the probabilistic distribution of both of them.

2. The fatigue model, the proposed life estimation is based on, is the Miner's rule (see Section 3.4). Different models can also be used such as the Smith-Watson-Topper model of Equation (2.13). Of course, the selection of fatigue model will affect the fatigue life estimation.
3. The mean stress correction we use is based on Morrow's criterion. Different criteria will affect the prediction.
4. The accuracy of the rainflow algorithm in estimating the cumulative fatigue damage, may depend on the duration of the terrain excitation signal. We recommend the duration to be at least 50 to 80 times the correlation length of the excitation random process.
5. Finally, the provided terrain signal excitation should be used to characterize the excitation random process and use it to generate many "similar" signals which belong to the excitation process. Each of these signals can be used in our proposed approach to provide a realization of the fatigue life. The average of these estimations can be finally used as the expected prediction.

Two examples are used in Sections 6.5 and 6.6 to demonstrate the effectiveness of the proposed approach.

## 6.4 Example 1: Artificial Signal

In the first example, we use an artificially constructed displacement signal as shown in Figure 6.5. The signal simulates the excitation load of the suspension rig of Figure 4.4. Figure 6.6 shows the associated strain signal. The latter has a 10 second duration and is represented by 101 equally-spaced points (10 Hz sampling frequency). The material in this example is mild steel with a fatigue strength coefficient $S_f = 1295\ MPa$ and a fatigue strength exponent, $b = 5.59$.

Using the strain signal a peak-valley algorithm identified all 19 peaks and valleys (local maxima and minima) (Figure 6.7) which are then used in cycle counting.

Using the signal of Figure 6.7 (after peak picking), the 4-point rainflow algorithm of Section 3.5.1 was executed. Figure 6.8 (a through f) shows the six identified damage cycles.

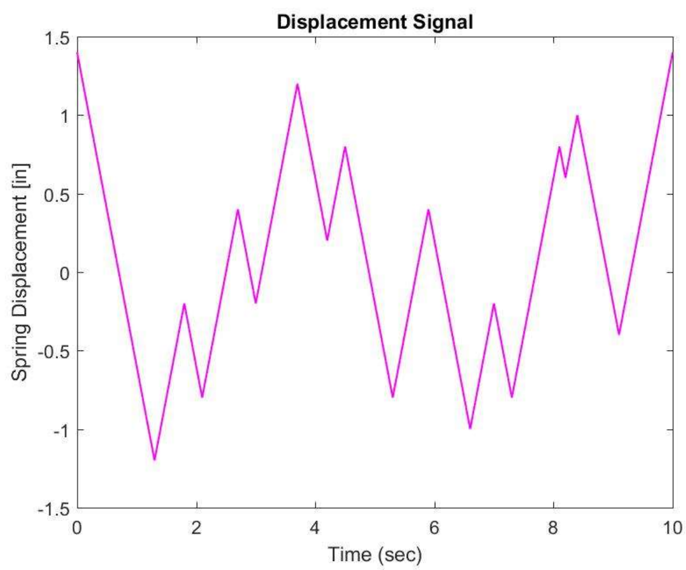


Figure 6.5 Displacement signal for example 1

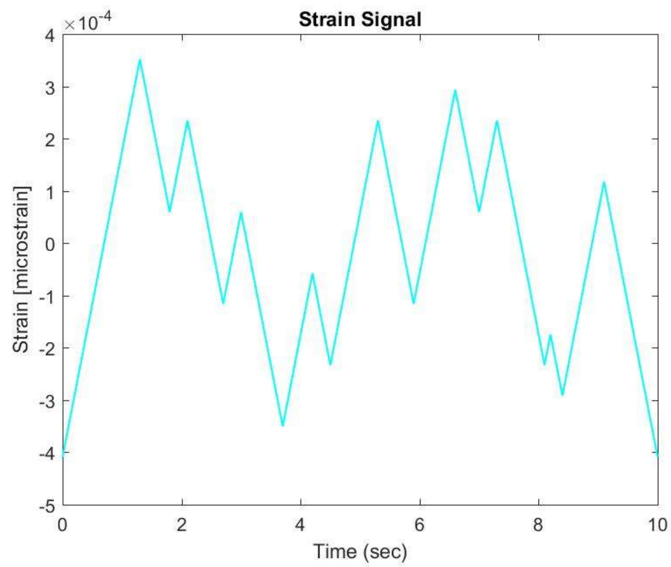


Figure 6.6 Strain signal for example 1

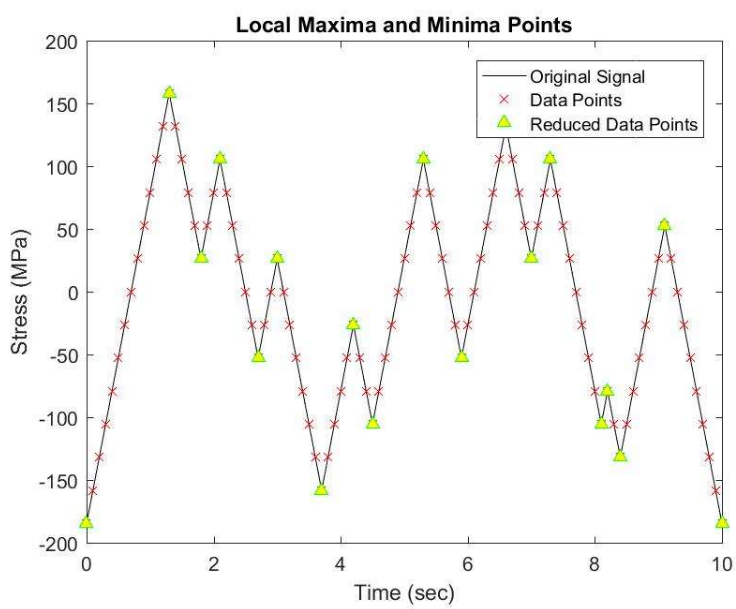


Figure 6.7 Identification of peaks and valleys for example 1

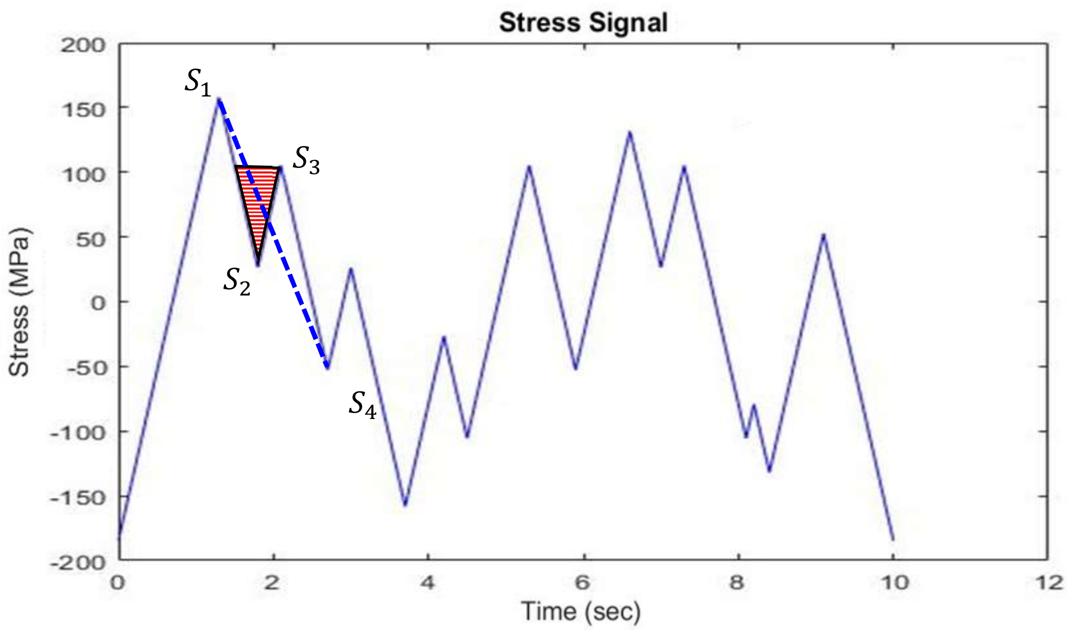


Figure 6.8 (a) 4-point rainflow counting method for example 1

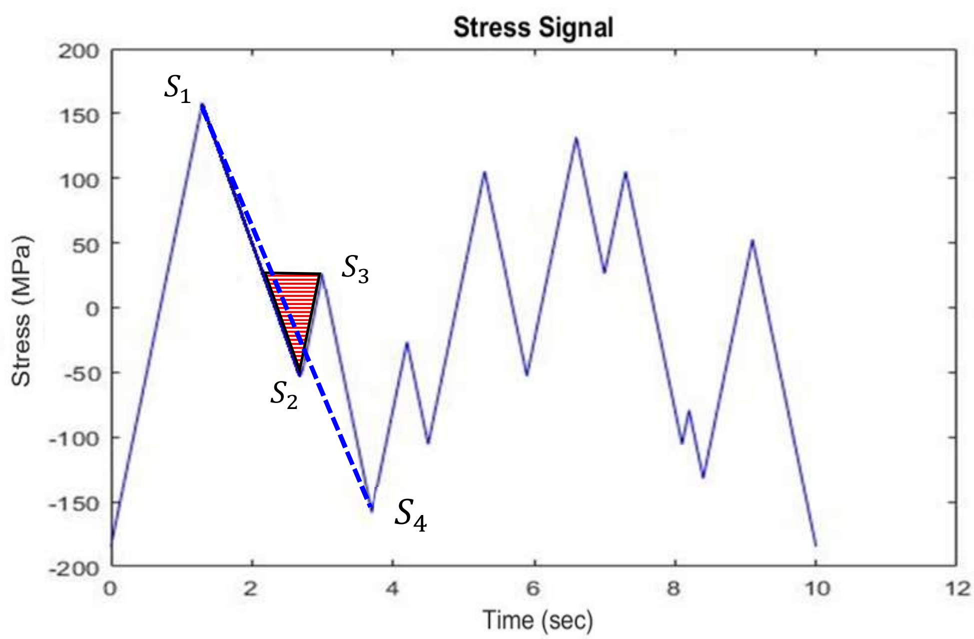


Figure 6.8 (b) 4-point rainflow counting method for example 1

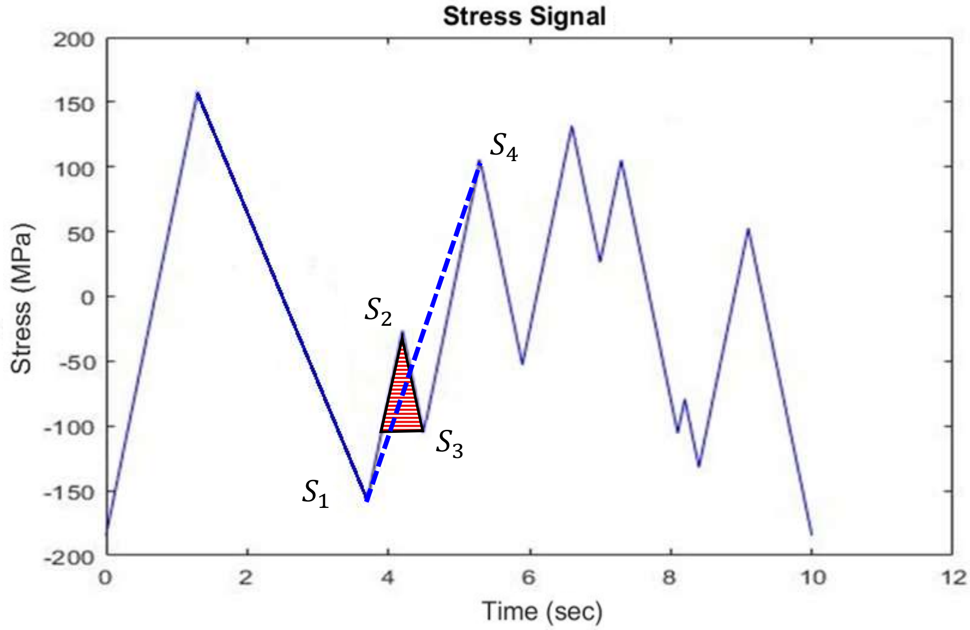


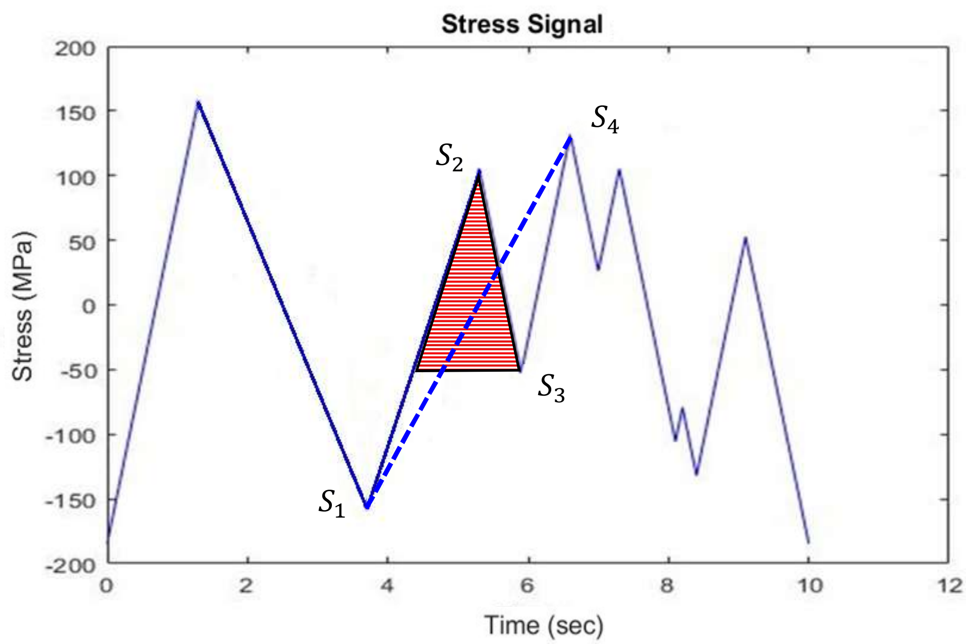


Figure 6.8 (d) 4-point rainflow counting method for example 1

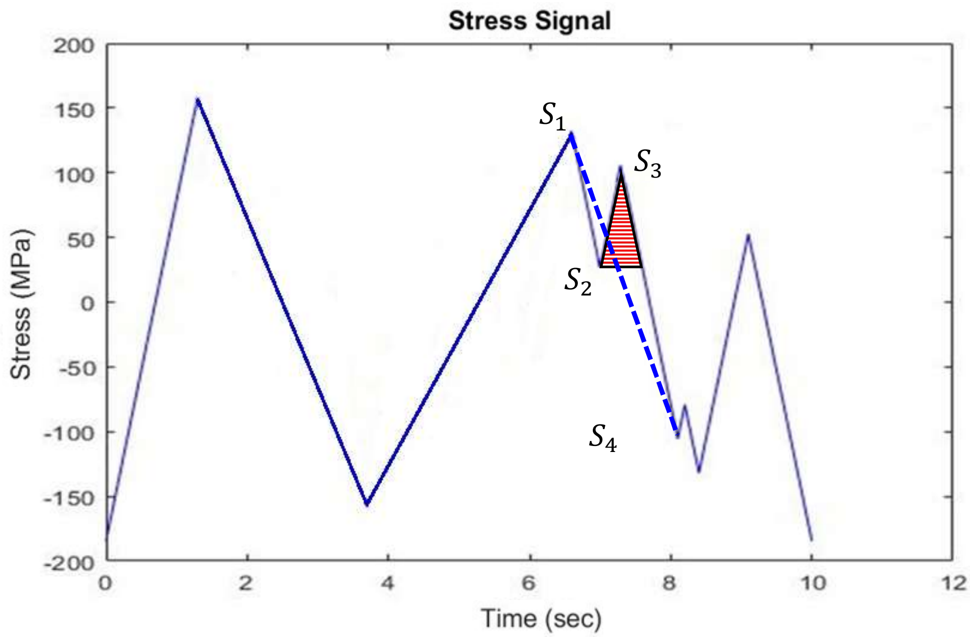


Figure 6.8 (e) 4-point rainflow counting method for example 1

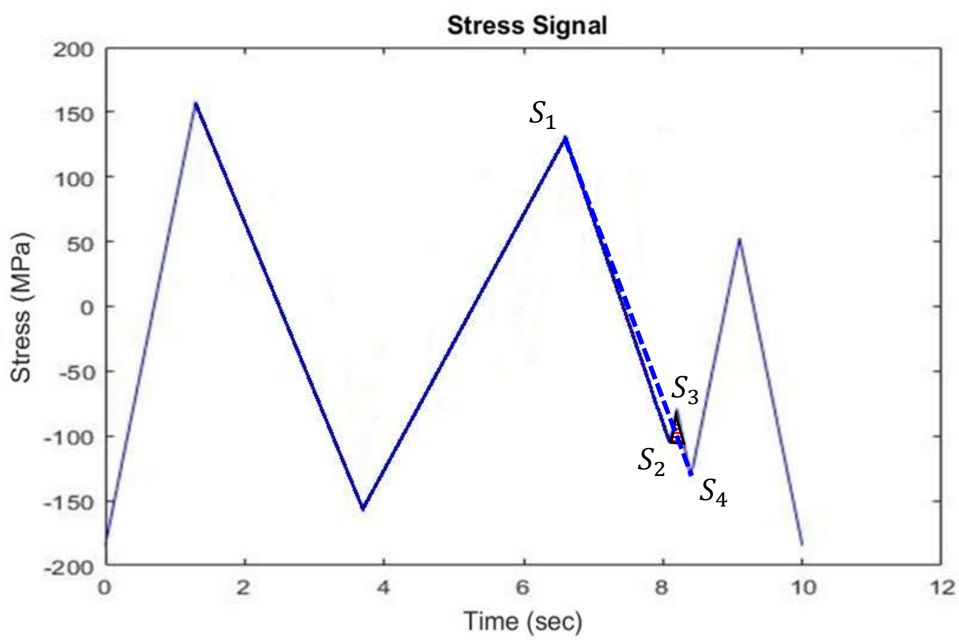


Figure 6.8 (f) 4-point rainflow counting method for example 1

From the six identified damage cycles (Figure 6.9), the damage of only one cycle is within the 90th percentile of the total damage. This is the only kept cycle. Note that Figure 6.9 shows the damage of only 5 cycles because the damage of the 6th cycle is negligible.

After the rainflow algorithm identifies all cycles, it removes them from the original signal. This forms a new signal called residual signal (Figure 6.10) which still includes damage accumulation which is not identified by the first run of the rainflow algorithm. To do so, a double residual signal is formed by repeating the residual signal (see Figure 6.11) and the rainflow algorithm is run again. The second run identifies the remaining damage in the signal by identifying additional damage cycles which usually dominate the overall damage.

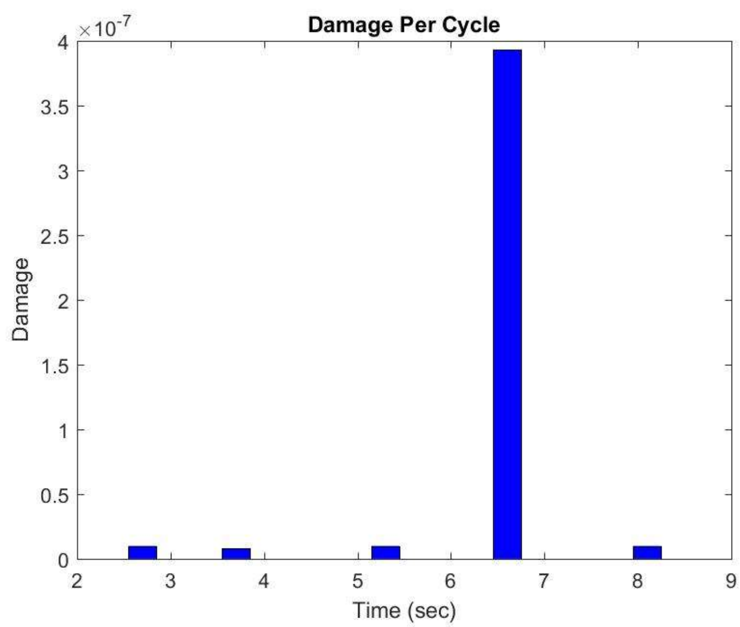

Figure 6.9 Damage per cycle for example 1

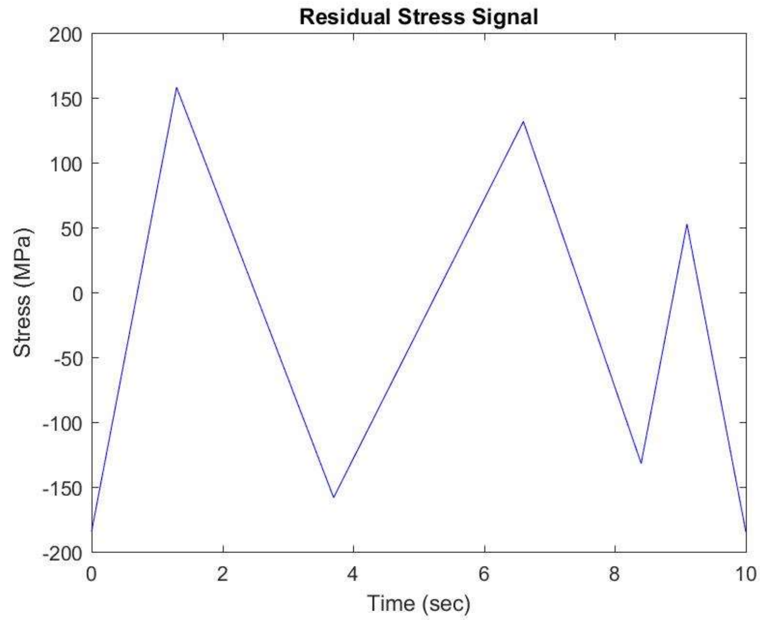


Figure 6.10 Residual stress signal for example 1

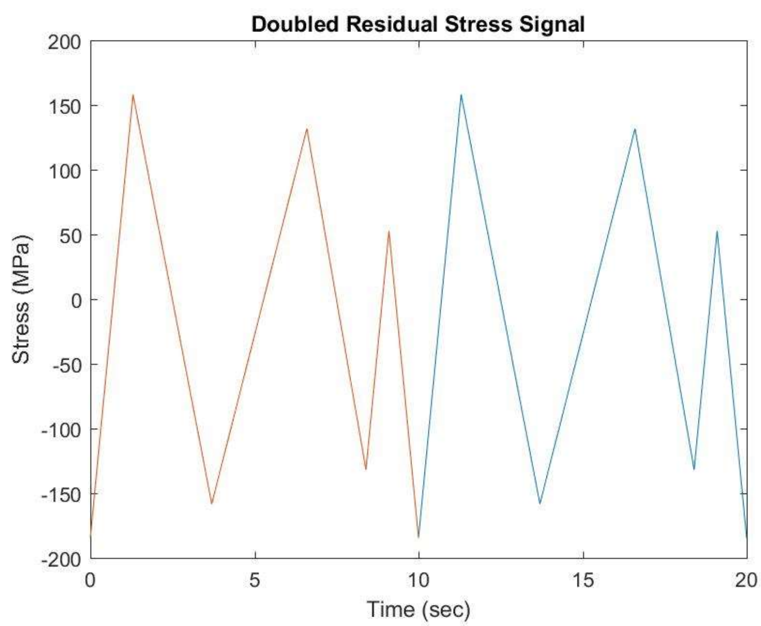


Figure 6.11 Double residual signal for example 1

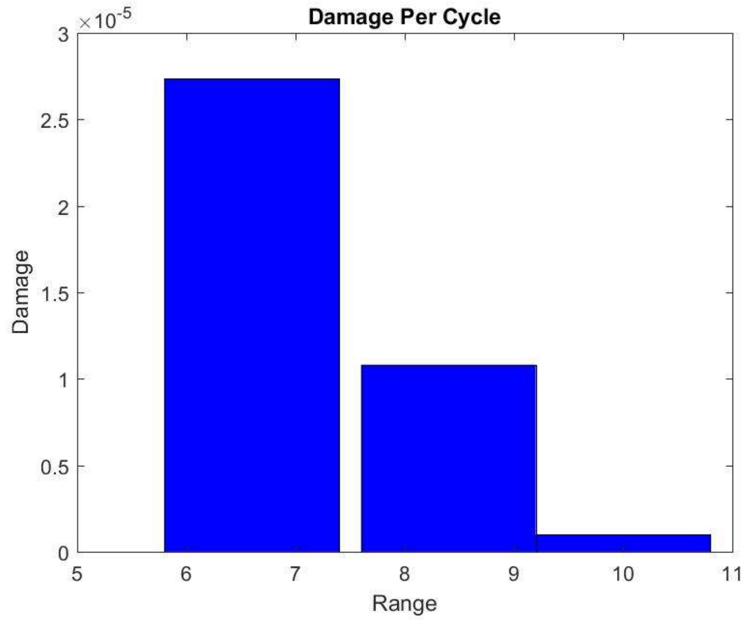


Figure 6.12 Damage per cycle from double residual signal for example 1

Using the double residual signal of Figure 6.11, three damage cycles are identified (Figure 6.12) which are all kept because they are within the 90$^{th}$ percentile of the total damage.

After all dominant damage cycles are identified and removed, a final stress signal is formed. Figure 6.13 compares the final stress signal with the original stress signal and Figure 6.14 shows how the final stress signal is converted to an excitation displacement signal which will drive the test rig of Figure 4.4. The conversion is straightforward because of the static assumption.

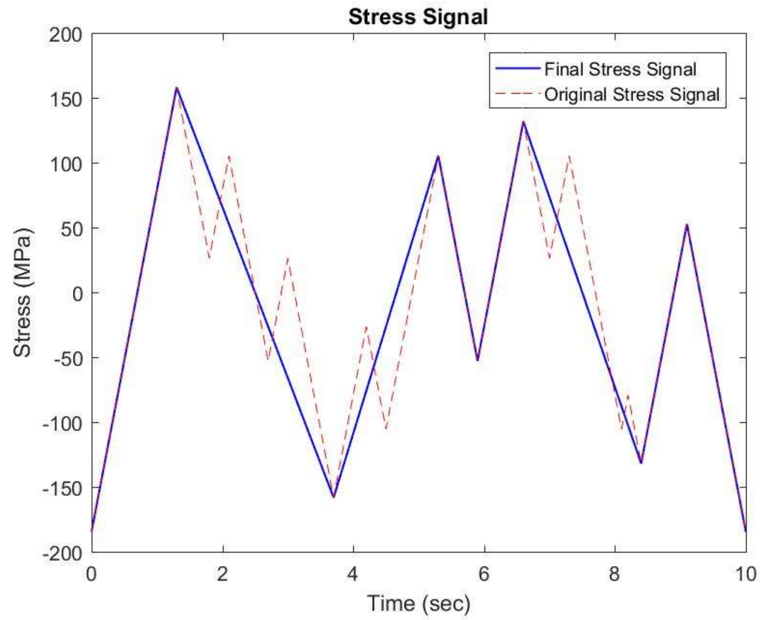


Figure 6.13 Final stress signal for example 1

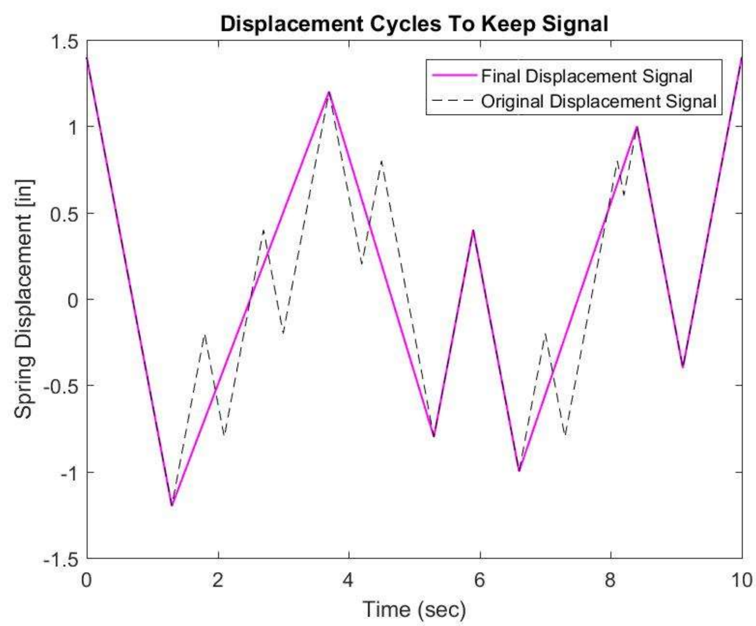


Figure 6.14 Final displacement signal for example 1

It should be noted that the damage of each cycle depends only on the cycle range (peak value minus valley value) and not on the time when the peak and the valley, forming the cycle, occur. This allows us to condense the final displacement signal by reducing its time duration without altering the values of its peaks and valleys. This operation however, will increase the energy in the condensed signal (i.e. increase the magnitude of its Power Spectral Density – PSD -) according to the scaling property of the Fourier transform. The amount of condensation is thus determined by a lab equipment limit which is based on a manufacturer specified PSD upper limit. This is necessary to avoid overheating during the durability test resulting in equipment failure.

The amount of condensation is also limited by the first natural frequency of the tested equipment in order to satisfy the static assumption needed for the validity of the proposed approach. The first natural frequency should be higher than the upper limit of the frequency range of the condensed signal PSD.

Figures 6.15 and 6.16 compare the condensed final stress and corresponding excitation displacement respectively, with the final uncompressed signals.

Figure 6.17 presents the various signals in terms of their PSD including the equipment limit (black line), and the first natural frequency of the tested HMMWV suspension spring (magenta line). As we have mentioned, the amount of signal condensation is limited by both the resulting signal PSD and the component first natural frequency. The blue dash line shows the PSD of the condensed Final Signal. We observe that it almost hits the equipment limit around 60 Hz reaching therefore the testing capabilities of the lab equipment. We also observe that the PSD of the original signal extends only to approximately 8 Hz which is much less than the natural frequency of the test component. This allows us to condense the final signal considerably, up to the upper limit of its PSD reaching the first natural frequency of the tested component.

Figure 6.18 is a zoom in of Figure 6.17. It shows that the PSD of the original and final signals follow the same trend. The condensed signal has lower power at lower frequencies but it maintains a high power at higher frequencies. This is because the signal condensation increases the frequency content of the signal.

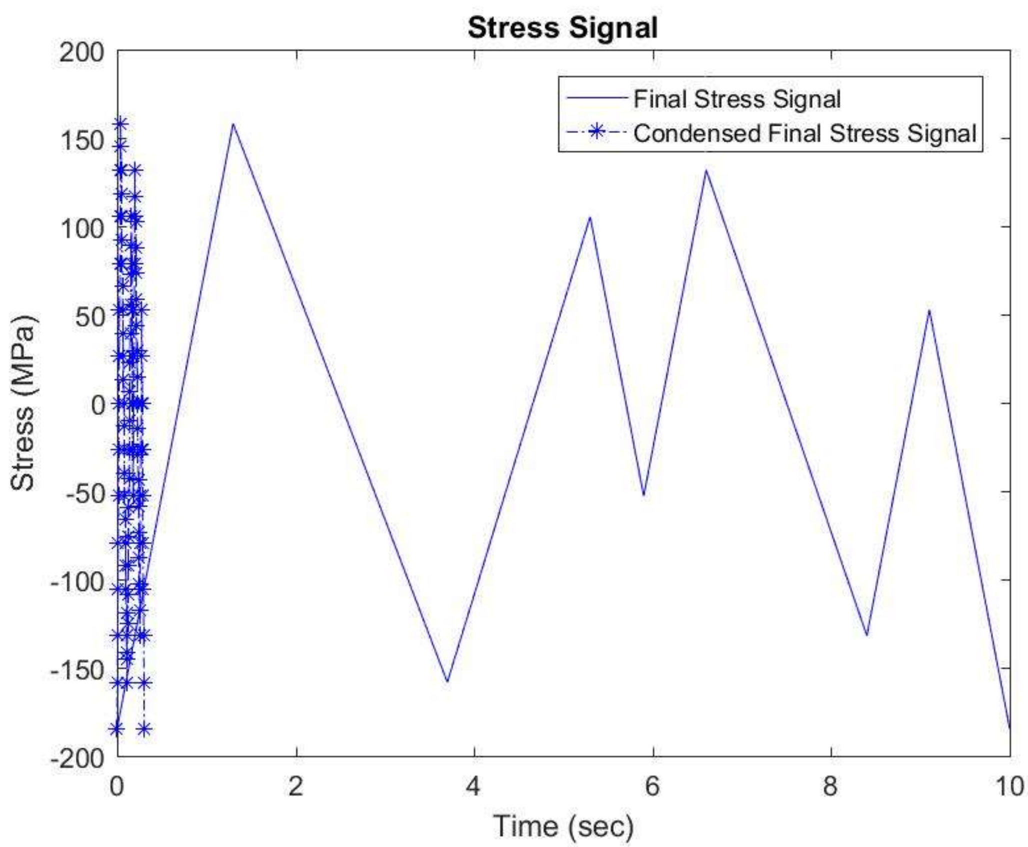


Figure 6.15 Condensed stress signal for example 1

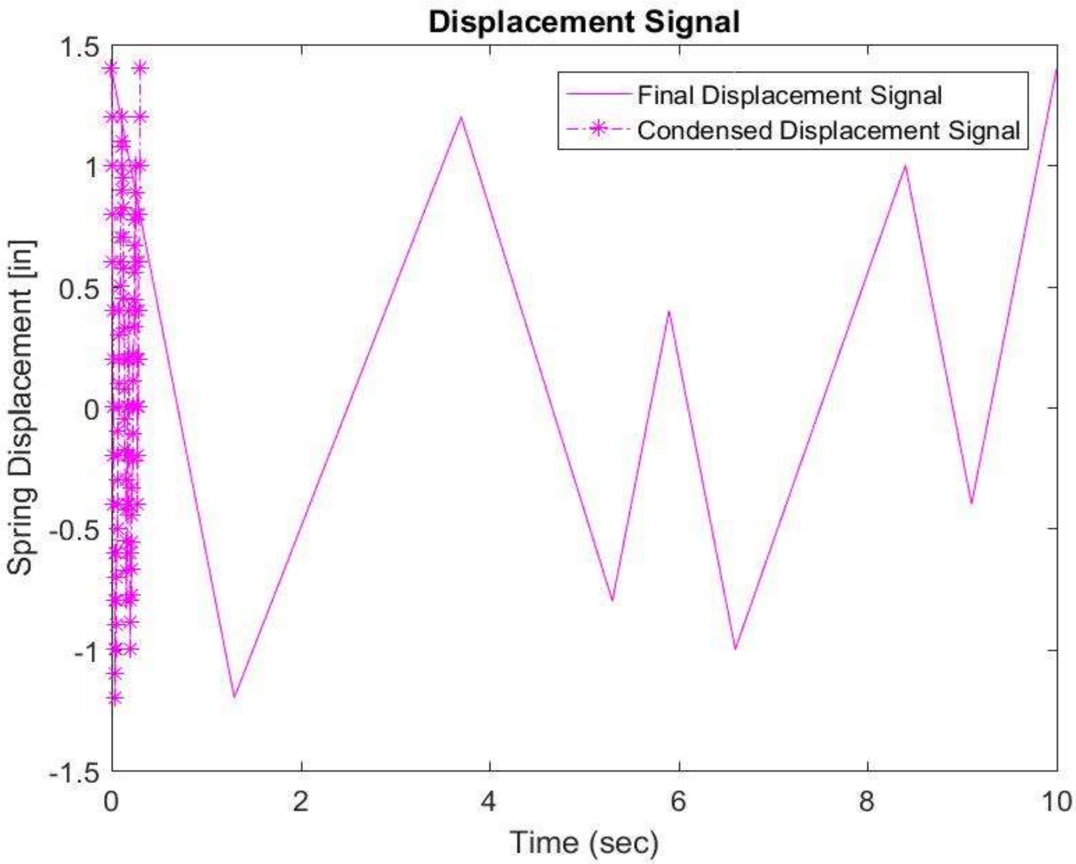


Figure 6.16 Condensed displacement signal for example 1

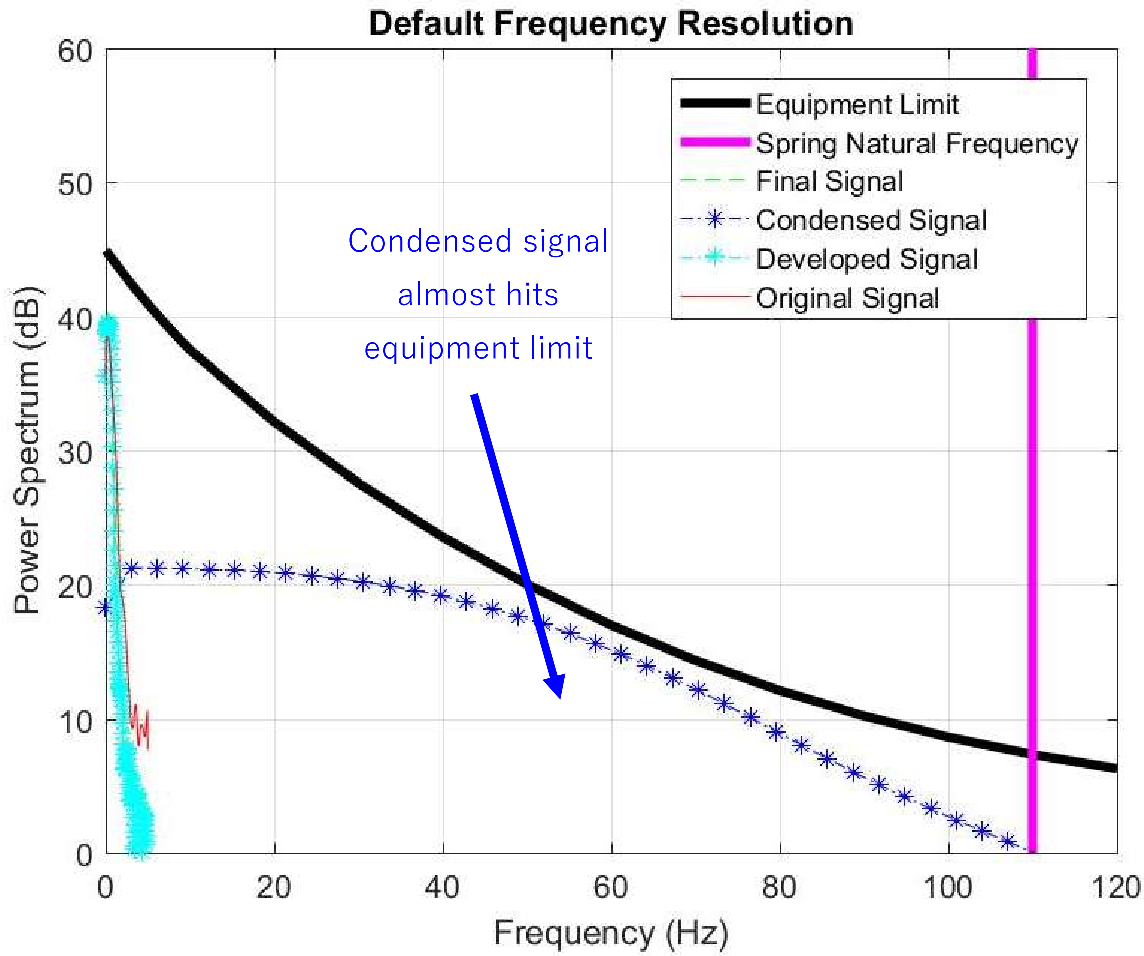


Figure 6.17 Power spectral density of various signals for example 1

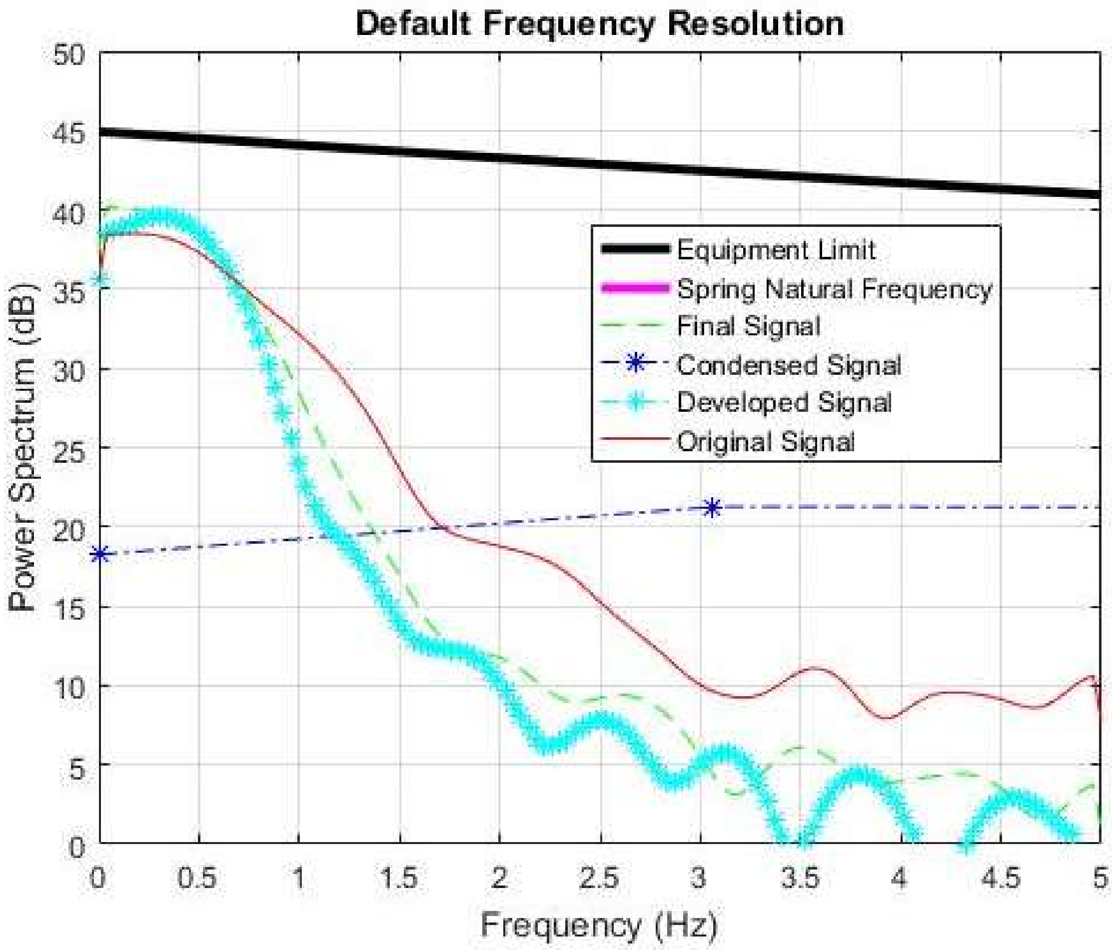


Figure 6.18 Zoom in of power spectral density representation of Figure 6.17

6.4.1 Estimation of Fatigue Life

We have mentioned that the four-point rainflow algorithm estimates the cumulative fatigue damage in two phases. The first one identifies a number of closed fatigue cycles, calculates the damage based on these cycles, and forms a residue signal by removing the portions of the original signal forming the identified cycles. Then, the second phase identifies additional cycles using a “residue + residue” signal.

The signal in this example is assumed to be 10-second long. The first phase of the rainflow algorithm identified 6 closed fatigue cycles with a cumulative damage of 4.3106e-07. Figure 6.9 shows the 5 most dominant cycles out of the 6. Out of the 6 cycles, the damage of only 1 cycle is within the 90th percentile of the total damage. This 1 cycle were kept along with the time each one occurred. The cumulative damage of the 1 kept cycle is 3.9334e-07.

After eliminating the 6 identified cycles from the original signal, a "residue" signal remained. Doubling the "residue" signal to form the "residue + residue" signal, and applying again the rainflow algorithm, we identified 3 additional cycles of cumulative damage of 3.9161e-05 (Figure 6.12). All these cycles were kept because each one is within the 90th percentile of the total damage. Thus, the total damage of the 1 plus 3 kept cycles is 3.9334e-07 + 3.9161e-05= 3.9554e-05. Note that the total damage of the original signal is 4.3106e-07+ 3.9161e-05= 3.9592e-05 which is very close to the damage of 3.9554e-05.

Using the kept cycle damage of 3.9554e-05, the total life in hours of the 40-second signal is

$$Total\ Life\ (Hours) = \frac{1}{\left(\frac{3.9554\text{e} - 05}{10}\right) \times 3600} = 70.2$$

At this point, the peaks and valleys of the 4 kept cycles are <u>equally spaced</u> in the 10-second time window. Finally, the equally-spaced synthetic signal is compressed in time seeking the maximum possible compression without the PSD of the compressed, equally-spaced signal exceeding the PSD limit of the equipment or the first natural frequency of the specimen.

For this example, the maximum compression is by a factor of 32.89 resulting in a duration of 10 / 32.89 = 0.304 seconds. This compressed signal is repeated many times until we reach a cumulative damage of 1 so that the specimen breaks. Using the compressed, equally-spaced signal, the expected duration of the new durability test is 70.2 / 32.89 = **2.134** hours.

## 6.5 Example 2: Belgian Block Terrain

A second example is used in this section to demonstrate the value of the proposed durability approach by running a vehicle with a 25 mph speed over a Belgian block terrain (Figure 6.19a). The resulting displacement excitation signal is shown in Figure (6.19b). The signal has a 40-second duration and it is sampled with a 2024 Hz frequency resulting in over 80,000 data points. Figure 6.20 shows the corresponding measured strain signal on the suspension spring. In this example we use steel P355NL1 with a fatigue strength coefficient, $S_f = 840\ MPa$ and a fatigue strength exponent, $b = -0.0808$.

First, we identify all peaks and valleys (4879 in total) which are the used for cycle counting (Figure 6.21). Using the identified peaks and valleys, the four-point rainflow cycle counting algorithm identified 2425 damage cycles. Out of the 2425 cycles, only the damage of 14 kept cycles is within the 90$^{th}$ percentile of the total damage (Figure 6.22). Figure 6.23 shows the formed signal with only the 14 kept cycles. Figure 6.24 shows the residual signal after the identification of all damage cycles, and Figure 6.25 shows the double residual signal. The latter is used in another run of the rainflow algorithm to identify additional damage cycles the first run did not identify.

Figure 6.19 (a) Belgian block terrain of example 2

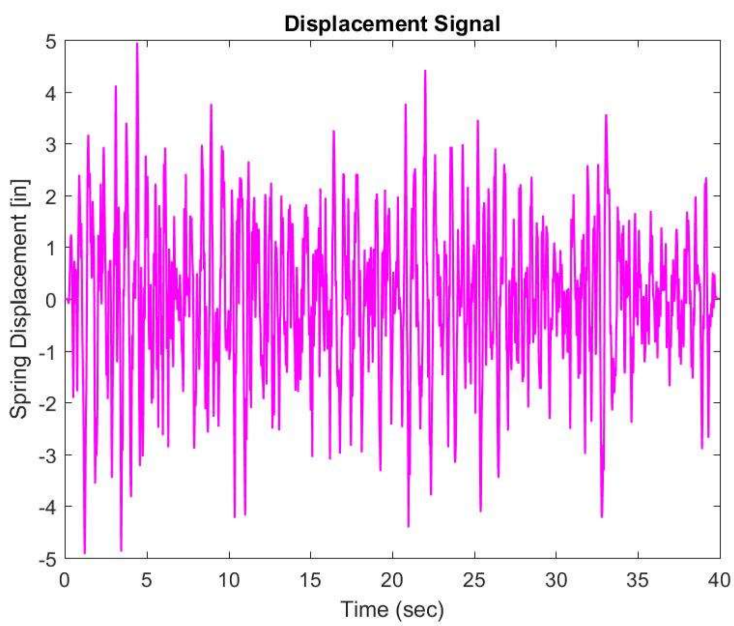


Figure 6.19 (b) Belgian block displacement signal of example 2

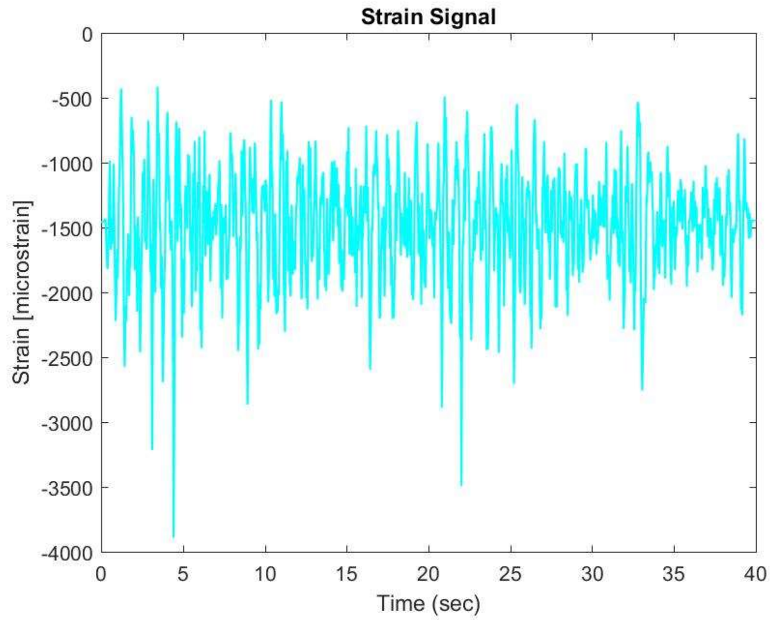


Figure 6.20 Belgian block strain signal of example 2

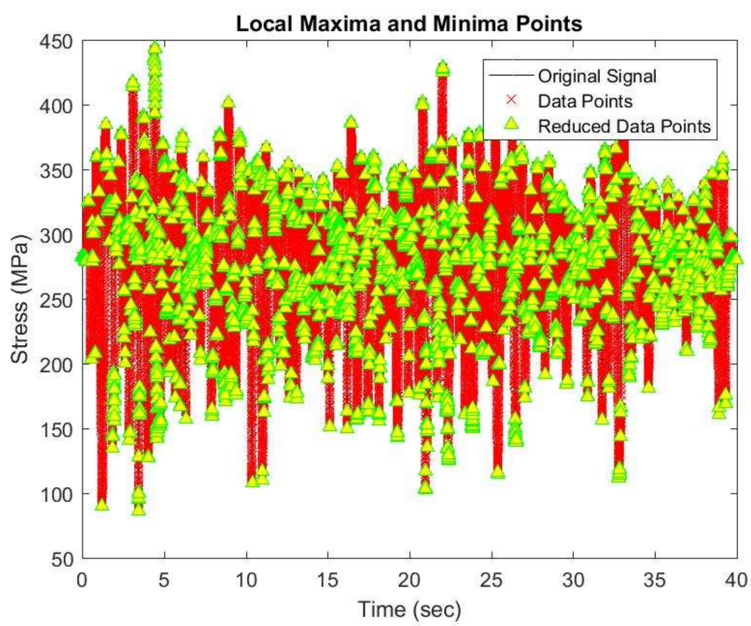


Figure 6.21 Peaks and valleys for Belgian block stress signal of example 2

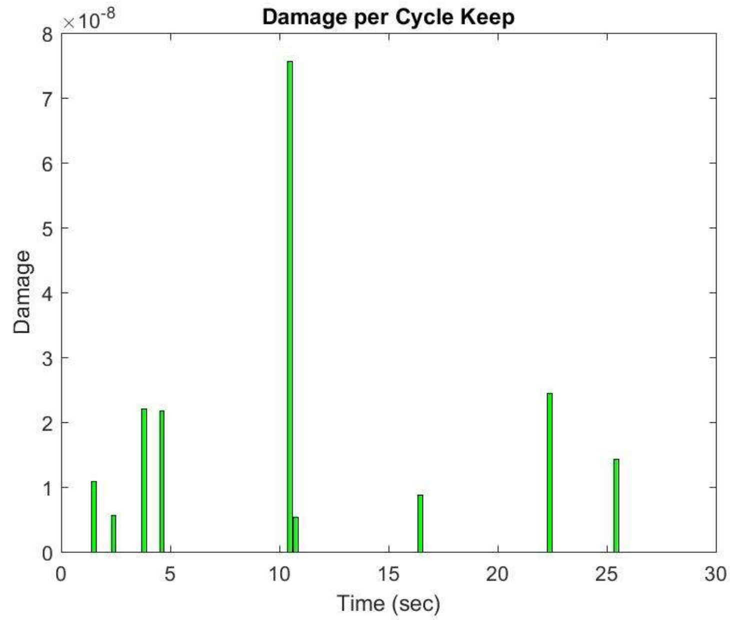


Figure 6.22 Damage per kept cycle for example 2

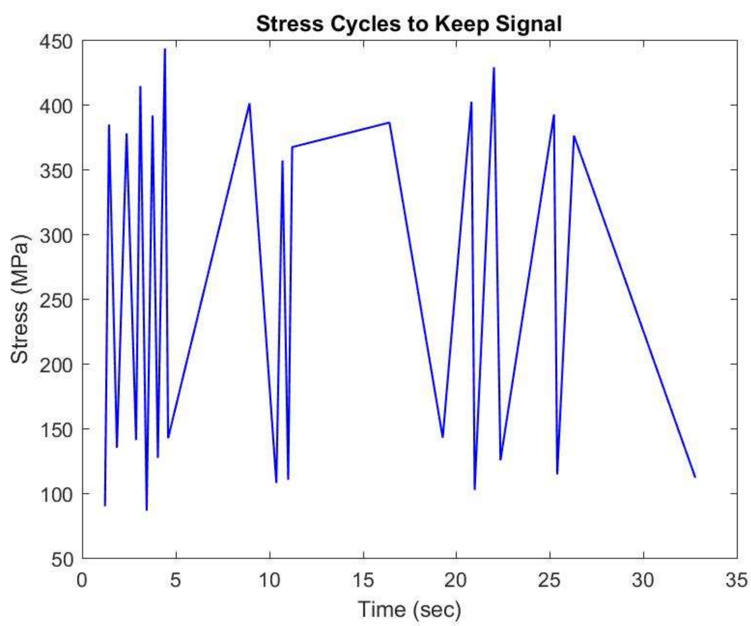


Figure 6.23 Stress signal for the kept cycles of example 2

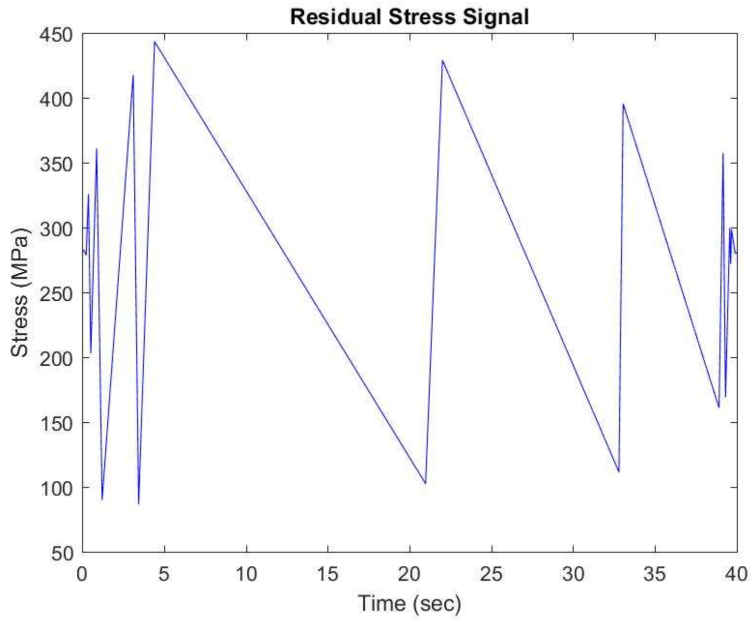


Figure 6.24 Residual stress signal for example 2

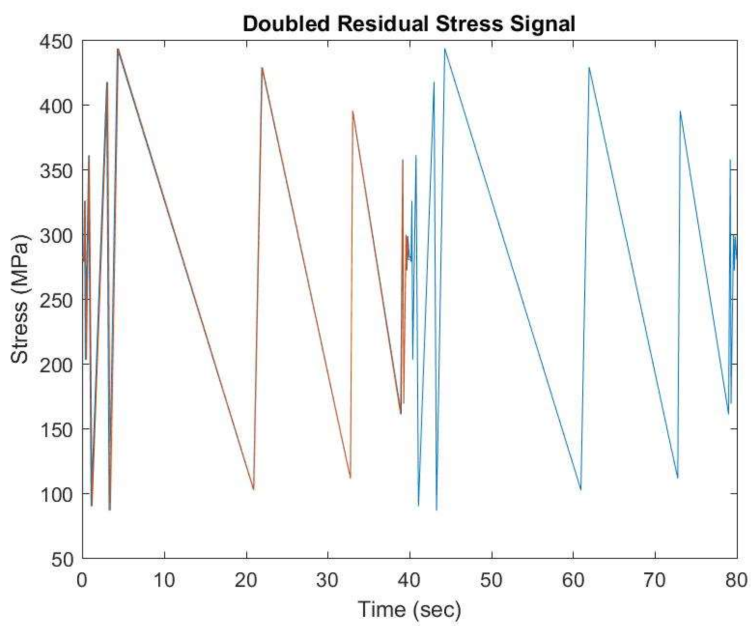


Figure 6.25 Double residual stress signal for example 2

Figure 6.26 shows the four dominant damage cycles identified in the double residual stress signal. Keeping only the dominant damage cycles from the first and second (residual) cycle counts we obtain the final stress signal of Figure 6.27 and the final displacement signal of Figure 6.28. It is clear that many cycles with small damage are removed simplifying the final signal considerably. Figures 6.29 and 6.30 show the condensed stress and displacement signals, respectively. The condensed signals have a much shorter duration reducing the durability test time considerably.

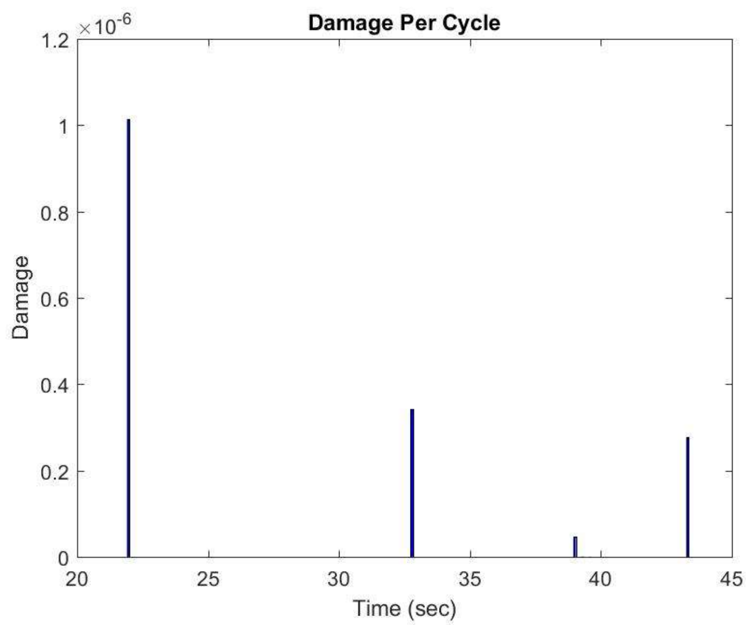


Figure 6.26 Dominant damage cycles from double residual stress signal for example 2

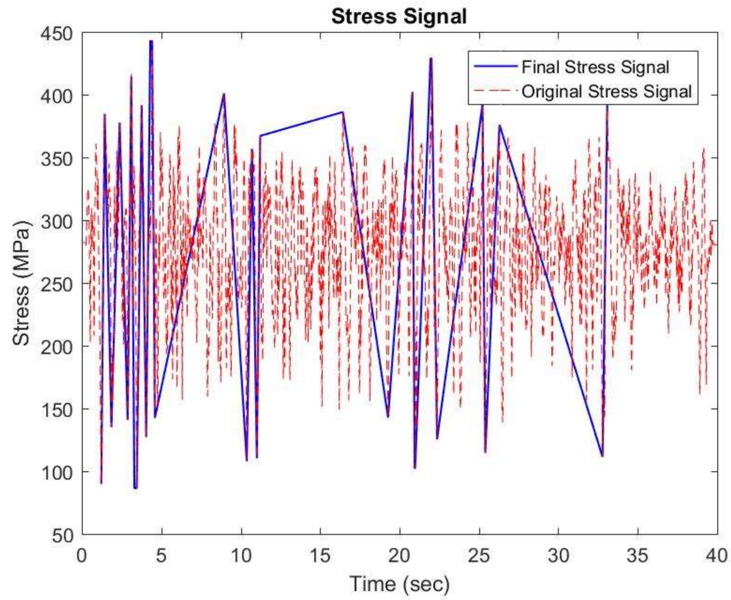


Figure 6.27 Final stress signal for example 2

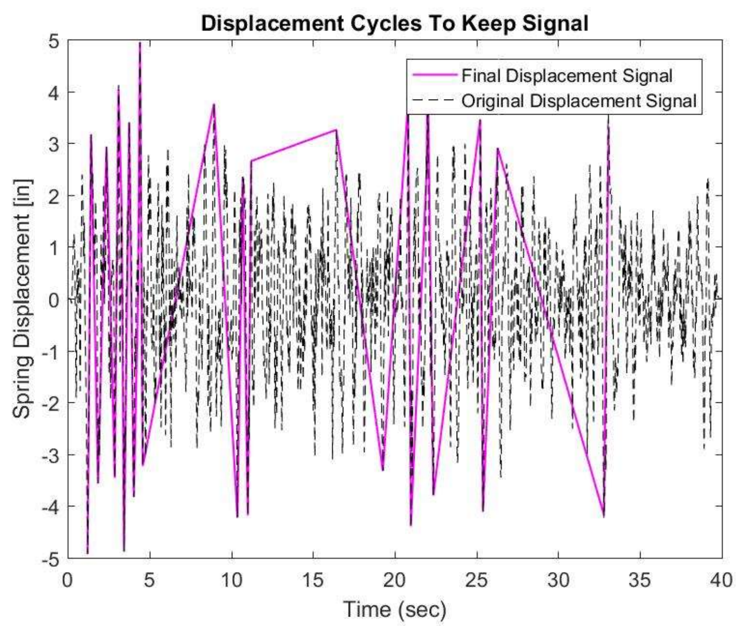


Figure 6.28 Final displacement signal for example 2

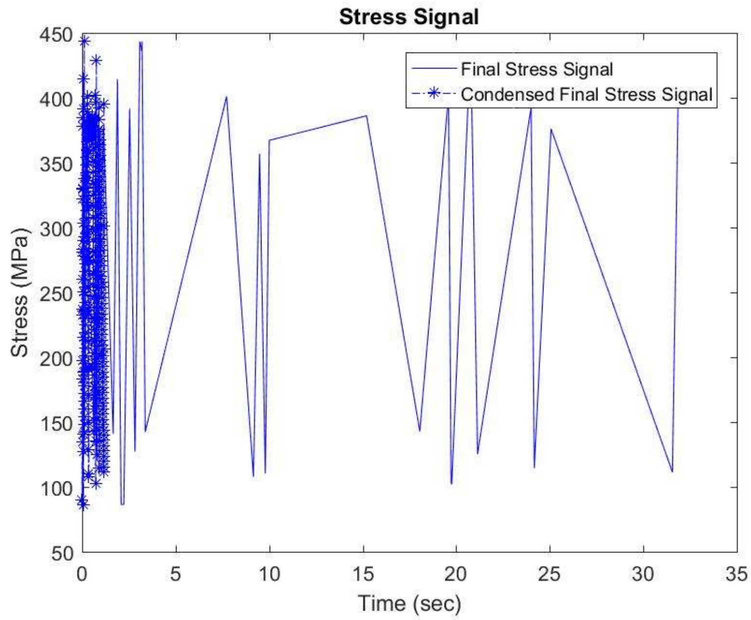


Figure 6.29 Condensed stress signal for example 2

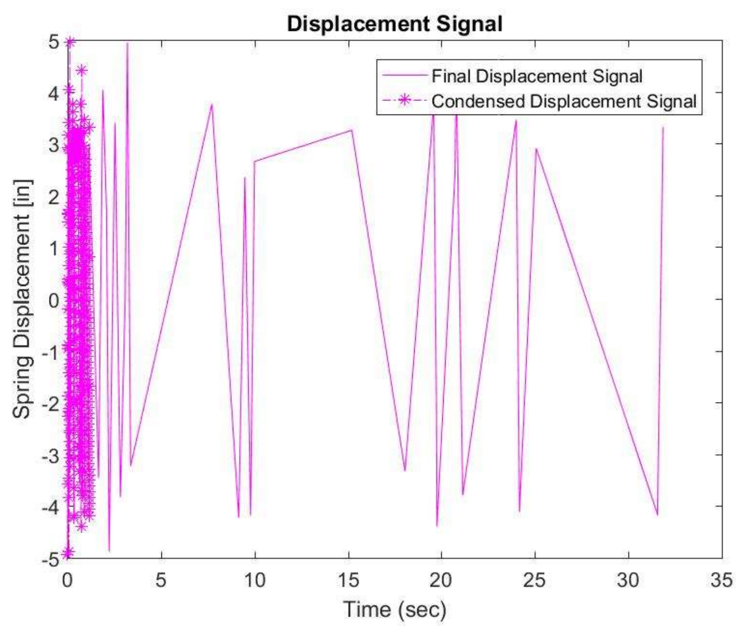


Figure 6.30 Condensed displacement signal for example 2

Figure 6.31 shows the condensed signal using the state-of-the-art "traditional method" which does not eliminate any cycles, and the condensed signal from the proposed new durability time reduction method. Figure 6.32 zooms in Figure 6.31 for the time period between 0.5 and 1 seconds indicating clearly that the condensed signal from the traditional method includes many cycles of minimal damage which make it very difficult to accurately represent on the experimental simulator. In contrast, the condensed signal of the proposed new durability time reduction method is very simple and easy to represent experimentally.

Figure 6.33 shows the power spectral density of various signals for the traditional and proposed methods. The black line represents the equipment limit PSD and the magenta line represents the first natural frequency of the HMMWV suspension spring. As we have mentioned, the condensed (compressed) final signal is determined using these two limits. The blue dash line represents the PSD of the condensed final signal. We observe that for the traditional method it violates the equipment limit around 62 Hz and also exceeds the first natural frequency of the HMMWV suspension spring. In contrast, the condensed final signal of the proposed approach does not violate the two limits.

It should be noted that in Figure 6.33 the original signal is 40 seconds long while the final synthetic signal from the new durability time reduction method is 34.85 seconds long and the condensed final signal is 1.49 second long.

Figure 6.34 shows a zoom in version of Figure 6.33, up to 20 Hz, showing details of the signals for the traditional and proposed approaches.

Figures 6.33 and 6.34 indicate that the PSD of the final and condensed stress signals exhibit high values at low frequencies. Because the cycle counting does not depend on the exact time of the peaks and valleys, Figure 6.35 shows a new developed stress signal created from the final signal with *equal spacing*. For comparison, we also show in this figure the condensed develop stress signal.

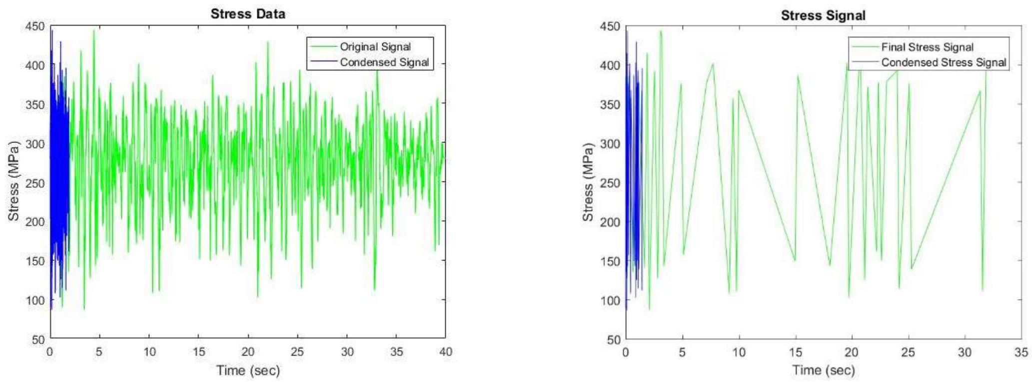


(a) (b)

Figure 6.31 Condensed stress signal from traditional method (a) and proposed method (b)

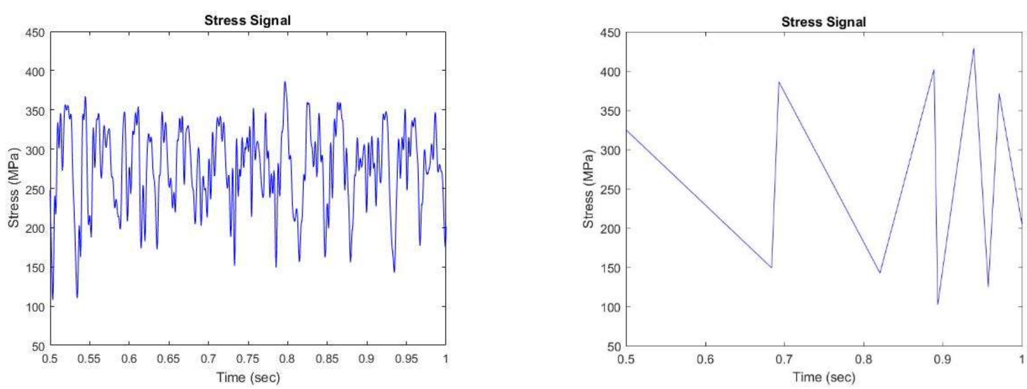


(a) (b)

Figure 6.32 Zoomed in condensed stress signal (0.5 to 1 sec) from traditional method (a) and proposed method (b) for example 2

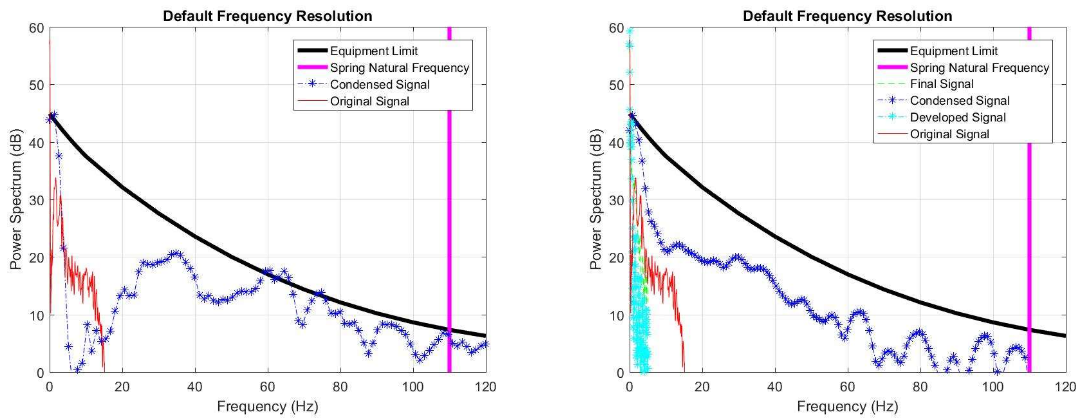


(a) (b)

Figure 6.33 Power spectral density of various signals for traditional method (a) and proposed method (b) for example 2

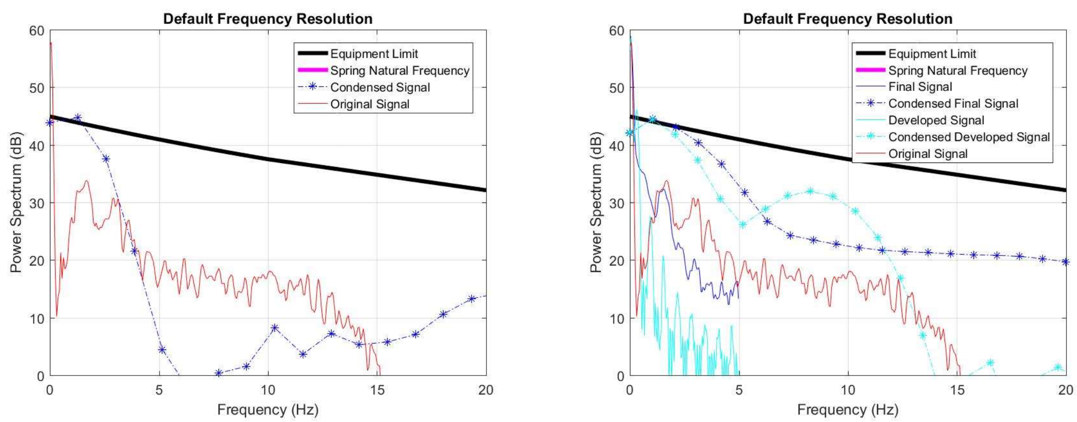


(a) (b)

Figure 6.34 Zoomed in power spectral density of various signals (0 to 20 Hz) for traditional method (a) and proposed method (b) for example 2

The circle regions of Figure 6.35 indicate insignificant change of the stress signal. In this case, we remove all points with insignificant change from the corresponding previous points and create a new signal (Figure 6.36). According to Figure 6.37, the new signal with equal spacing has lower power especially at higher frequencies providing more control over the amount of condensation we can perform. Note that more condensation is desirable in order to reduce the durability test time.

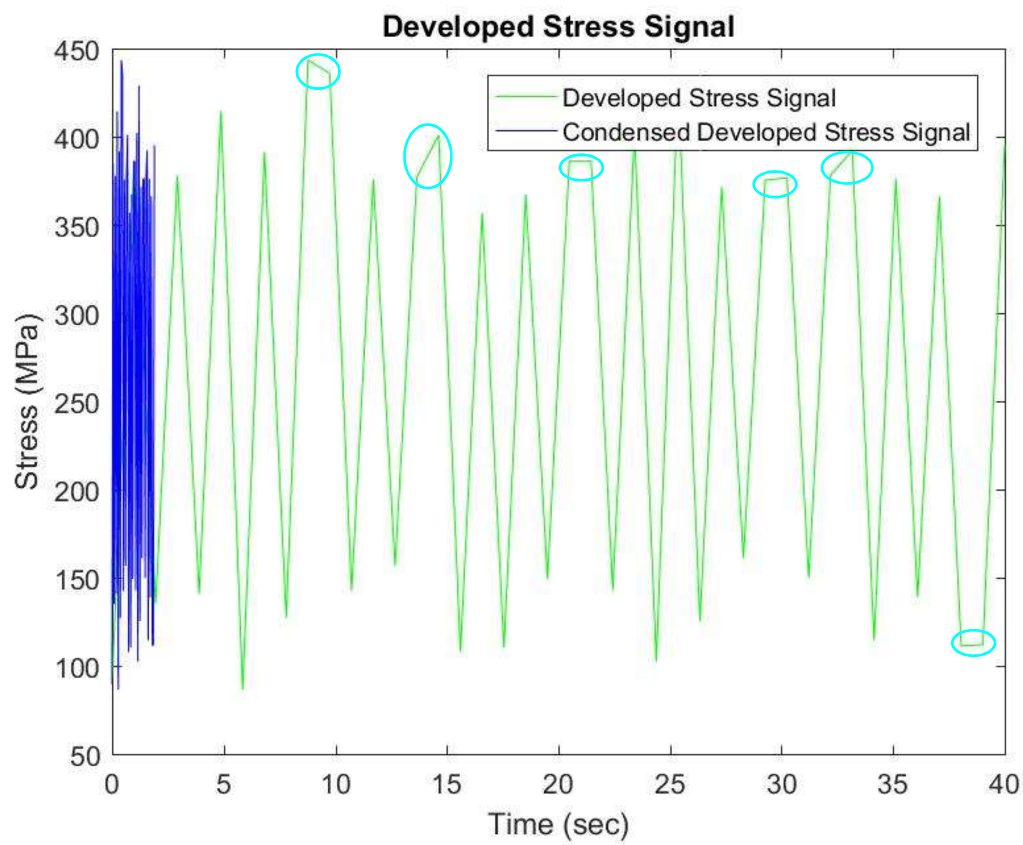


Figure 6.35 Developed stress signal with equal time spacing

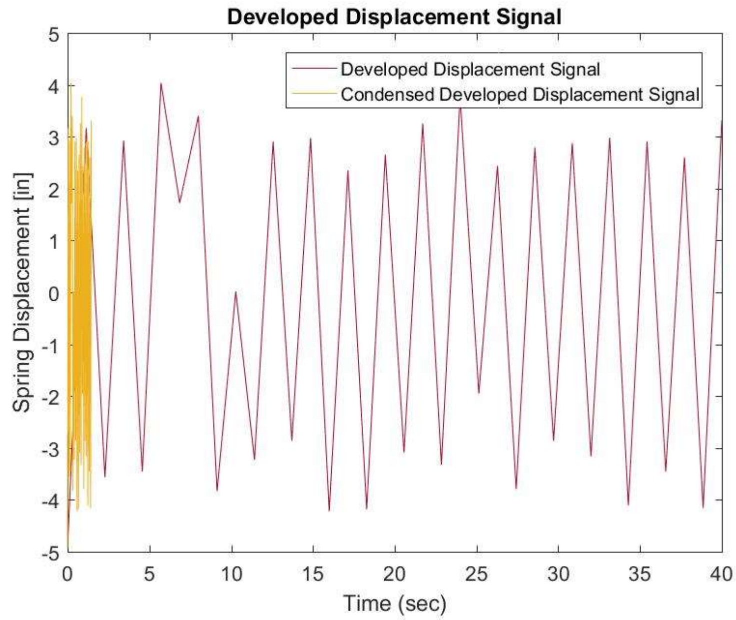


Figure 6.36 Developed displacement signal with equal time spacing

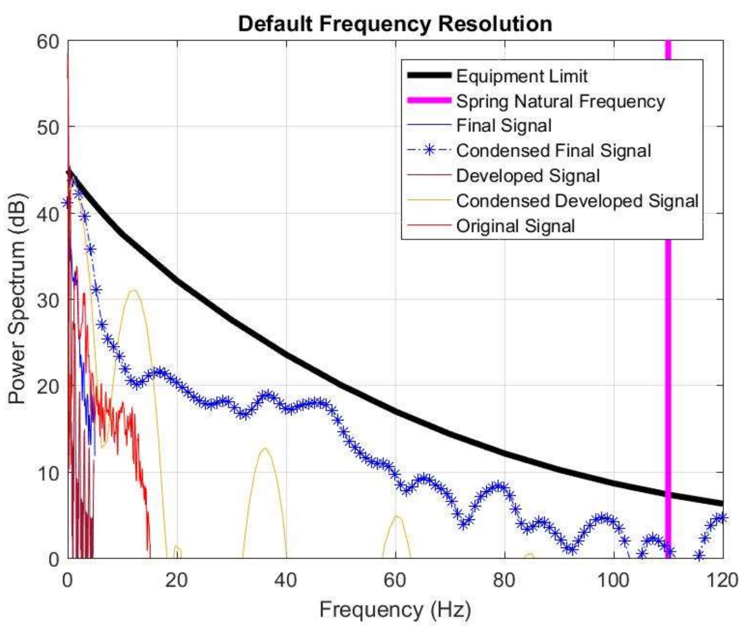


Figure 6.37 Power spectral density of various signals for traditional method including new condensed signal with equal spacing

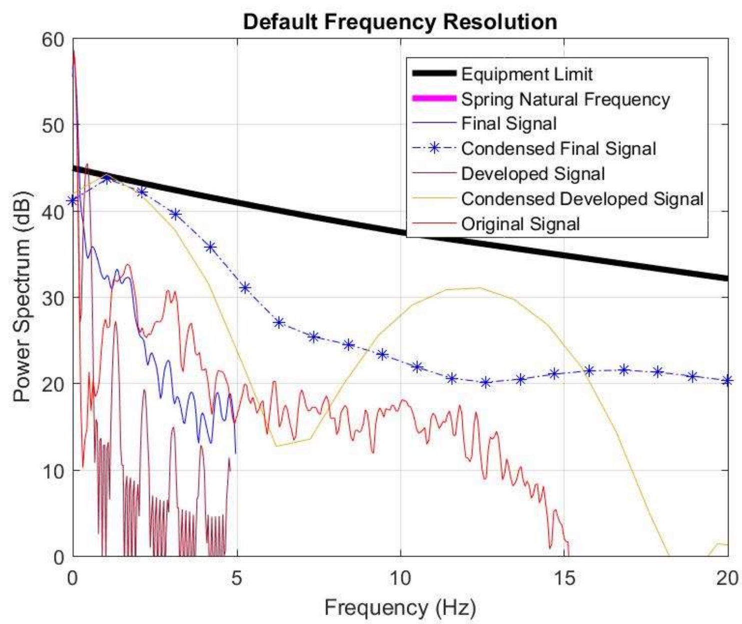


Figure 6.38 Zoomed in power spectral density of various signals (0 to 20 Hz) including new condensed signal with equal spacing

We observe in Figure 6.38 (zoomed in PSD of Figure 6.37 from 0 to 20 Hz) that condensed developed signal with equal spacing is at the equipment limit at 1.4 Hz. However, its power is at frequencies well below the 110 Hz first natural frequency of the tested component (Figure 6.37). We should note that the condensation percentage depends on the equipment's limit (black line in Figure 6.38) and the specimen's first natural frequency.

6.5.1 Estimation of Fatigue Life

In this section, we estimate the expected (average) fatigue life of the HMMVW suspension coil spring under the Belgian block terrain excitation of Figure 6.19 using the proposed durability approach and compare it with the conventional approach. Note that the duration of the Belgian block terrain excitation chosen equal to 40 seconds. The comparison demonstrates clearly the substantially shorter testing time of the proposed approach.

For this example, it was not known if the material of the HMMVW suspension spring was hardened. For this reason, we predicted the fatigue life both for the hardened steel P355NL1 material and the SAE 1038 (not hardened steel). The following fatigue life estimation is based on the coil material being <u>hardened</u> steel P355NL1 with an <u>estimated</u> fatigue strength coefficient, $S_f = 840\ MPa$ and a fatigue strength exponent, $b = -0.0808$.

We have mentioned that the four-point rainflow algorithm estimates the cumulative fatigue damage in two phases. The first one identifies a number of closed fatigue cycles, calculates the damage based on these cycles, and forms a residue signal by removing the portions of the original signal forming the identified cycles. Then, the second phase identifies additional cycles using a "residue + residue" signal.

For this example, using the 40-second long original Belgian block signal, the first phase of the rainflow algorithm identified 2425 closed fatigue cycles with a cumulative damage of 2.121725e-07. Out of the 2425 cycles, the damage of only 14 cycles is within the 90th percentile of the total damage. These 14 cycles were kept along with the time each one occurred. The cumulative damage of the 14 kept cycles is 1.889976e-07. Out of these cycles, Figure 6.22 shows the 9 most dominant.

After eliminating the 2425 identified cycles from the original signal, a "residue" signal remained. Doubling the "residue" signal to form the "residue + residue" signal, and applying again the rainflow algorithm, we identified 4 additional cycles of cumulative damage of 1.680997e-06 (Figure 6.26). All these cycles were kept because each one is within the 90th percentile of the total damage. Thus, the total damage of the 14 plus 4 kept cycles is 1.889976e-07 + 1.680997e-06 = 1.87e-06. Note that the total damage of the original signal is 2.121725e-07 + 1.680997e-06 = 1.893170e-06 which is very close to the damage of 1.87e-06.

Using the kept cycle damage of 1.87e-06, the total life in hours of the 40-second signal is

$$Total\ Life\ (Hours) = \frac{1}{\left(\frac{1.87e-06}{40}\right) \times 3600} = 5941$$

At this point, the peaks and valleys of the 18 kept cycles are <u>equally spaced</u> in the 40-second time window (Figure 6.36). Finally, the equally-spaced synthetic signal is compressed in time seeking the maximum possible compression without the PSD of the compressed, equally-spaced signal exceeding the PSD limit of the equipment or the first natural frequency of the specimen (Figure 6.37).

For this example, the maximum compression is by a <u>factor of 34</u> resulting in a duration of 40 / 34 = 1.176 seconds. This compressed signal is repeated many times until we reach a cumulative damage of 1 so that the specimen breaks. Using the compressed, equally-spaced signal, the expected duration of the new durability test is

5941 / 34 = **174.7** hours.

Assuming that the coil material is SAE 1038 (<u>not hardened</u> steel) with an <u>estimated</u> fatigue strength coefficient, $S_f = 1039\ MPa$ and a fatigue strength exponent, $b = -0.132$, and repeating the above steps of the proposed approach, the expected duration of the new durability test is

103.89 / 36.45 = **2.85** hours.

## 6.6 Experimental Validation of Proposed Approach

In this section, we present an experimental validation of the proposed durability test time reduction approach using the coil spring of the right rear HMMWV suspension. The specimen is a part of a HMMWV quarter-car subsystem (Figure 4.4). The HMMWV suspension is excited by a Belgian block terrain at 25 mph.

Before the test is executed, the PID controller of the test machine must be calibrated (i.e. establish the three gains for the PID control) so that the actuation provides the desired input signal as excitation to the specimen. The calibration is performed iteratively, as explained in Section 4.2, Step #5 due to potential inherent nonlinearities of the system.

As mentioned in Section 4.2, the number of iterations required for calibration and the RMS error between the achieved actuation and the desired input signal, are important to ensure the quality of the input signal of the Belgian block terrain at 25 mph and the developed synthetic and equally-spaced condensed signal.

Figure 6.39 shows the RMS error of a Belgian block signal after 5 iterations and Figure 6.40 shows a subsection of the desired and response displacement signal. The RMS error is reduced substantially after 5 iterations resulting in an actuation signal which is very close to the desired one (Figure 6.40).

Similarly, a high quality signal is observed for the synthetic, equally-spaced developed signal (after elimination of all low-damage cycles) after 5 iterations as shown in Figure 6.41.

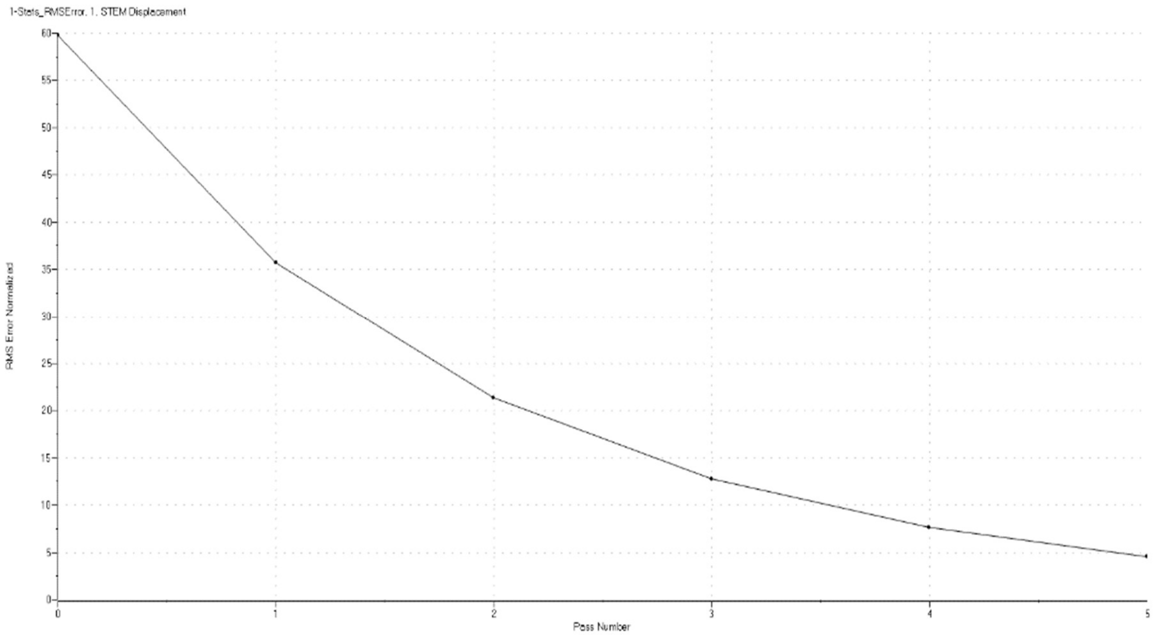


Figure 6.39 RMS error of Belgian block signal after 5 iterations

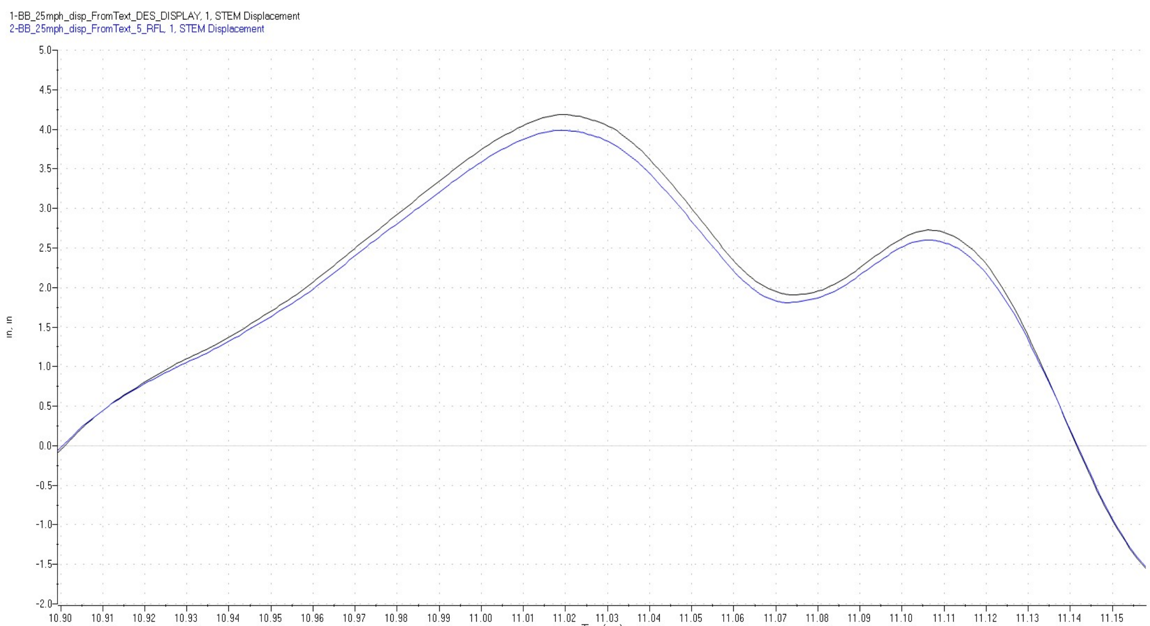


Figure 6.40 Desired vs response displacement signal for Belgian block

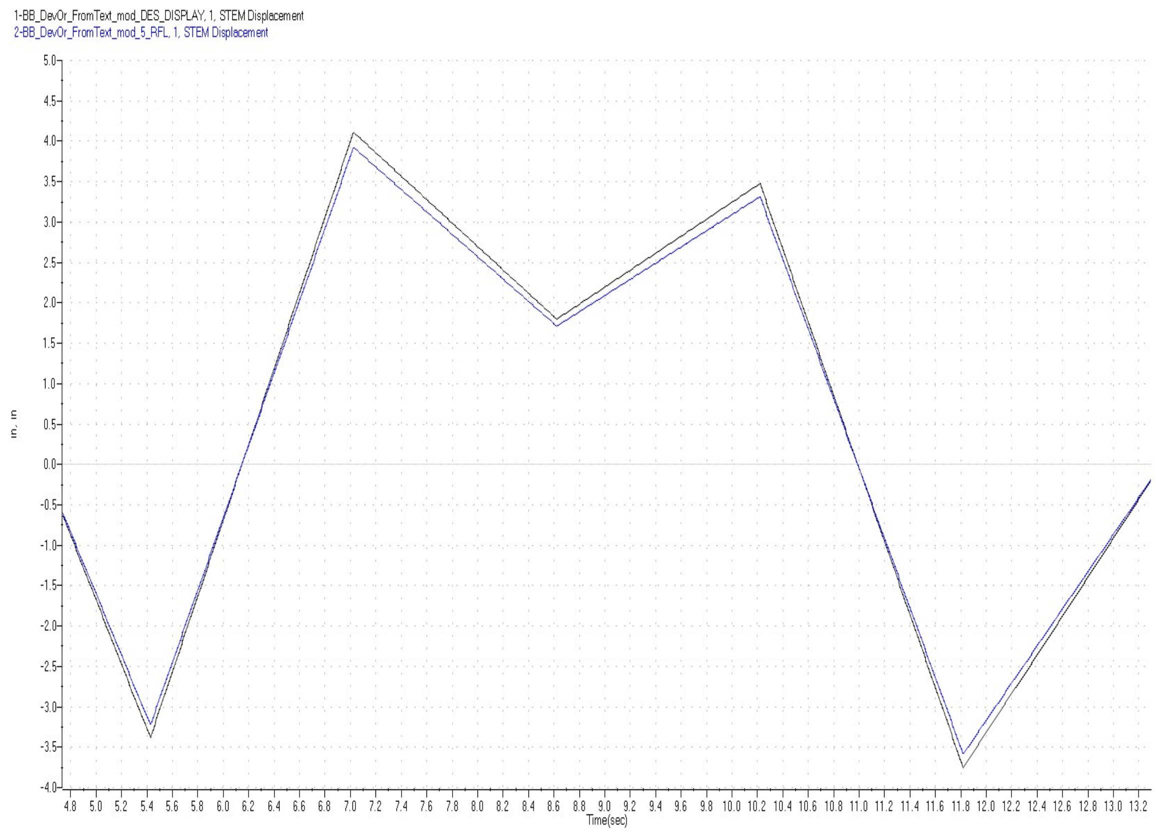


Figure 6.41 Desired vs response displacement equally-spaced developed signal

Figure 6.42 shows a subsection of the desired and response displacement of the developed, equally-spaced condensed signal which is used to execute the proposed durability test. Again, the agreement between the desired signal and the achieved one after 5 iteration is excellent. The achieved high accuracy after a low number of iterations is very important because we achieve a high-quality signal quickly reducing therefore, the test setup time.

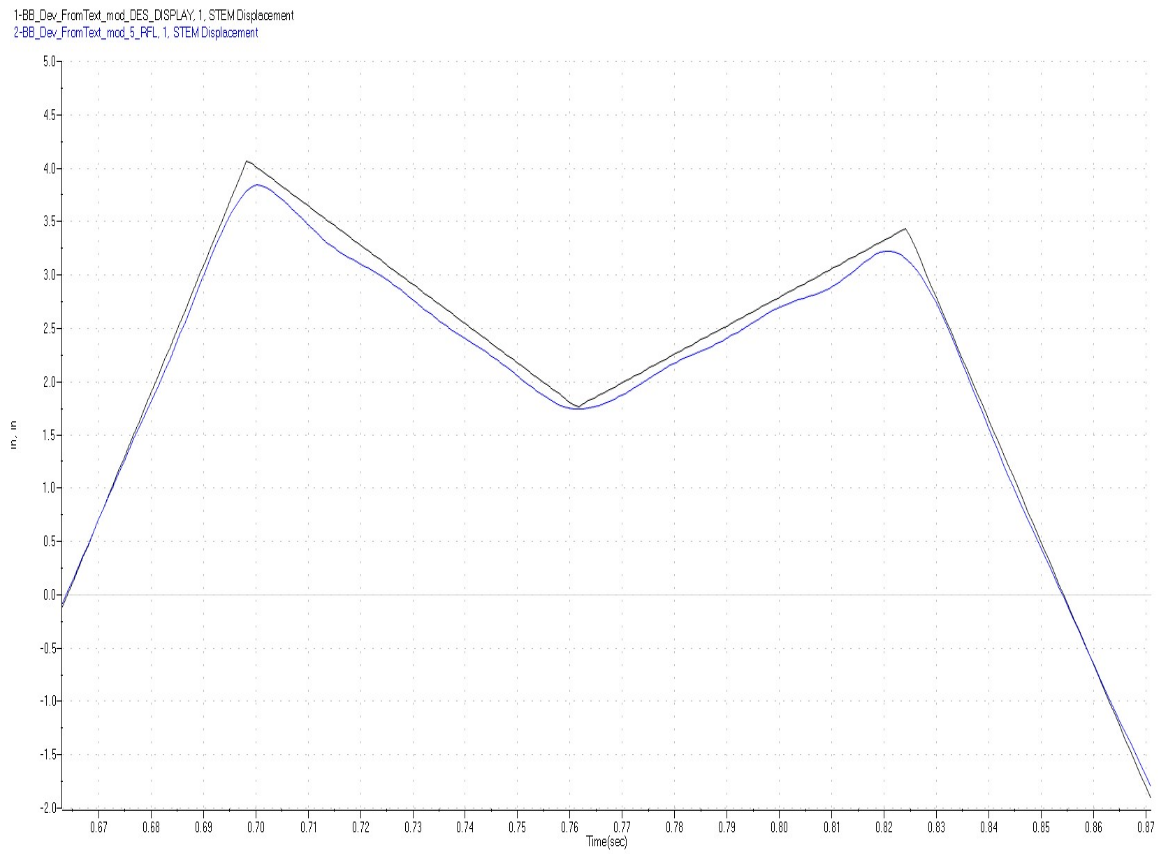


Figure 6.42 Desired vs response displacement equally-spaced condensed signal

Figure 6.43 shows the Power Spectrum Density (PSD) of the drive (excitation) signal for the Belgian block terrain, the PSD of the synthetic developed signal with equal spacing, and the PSD of the synthetic developed condensed signal. As expected the latter has a higher power compared to the other two signals because of the compression in time. Most of the energy however, is at low frequencies away for the 110 Hz natural frequency of the coil. This supports the static assumption used to develop the proposed durability method. The test was setup to execute until failure by repeating the developed synthetic condensed signal.

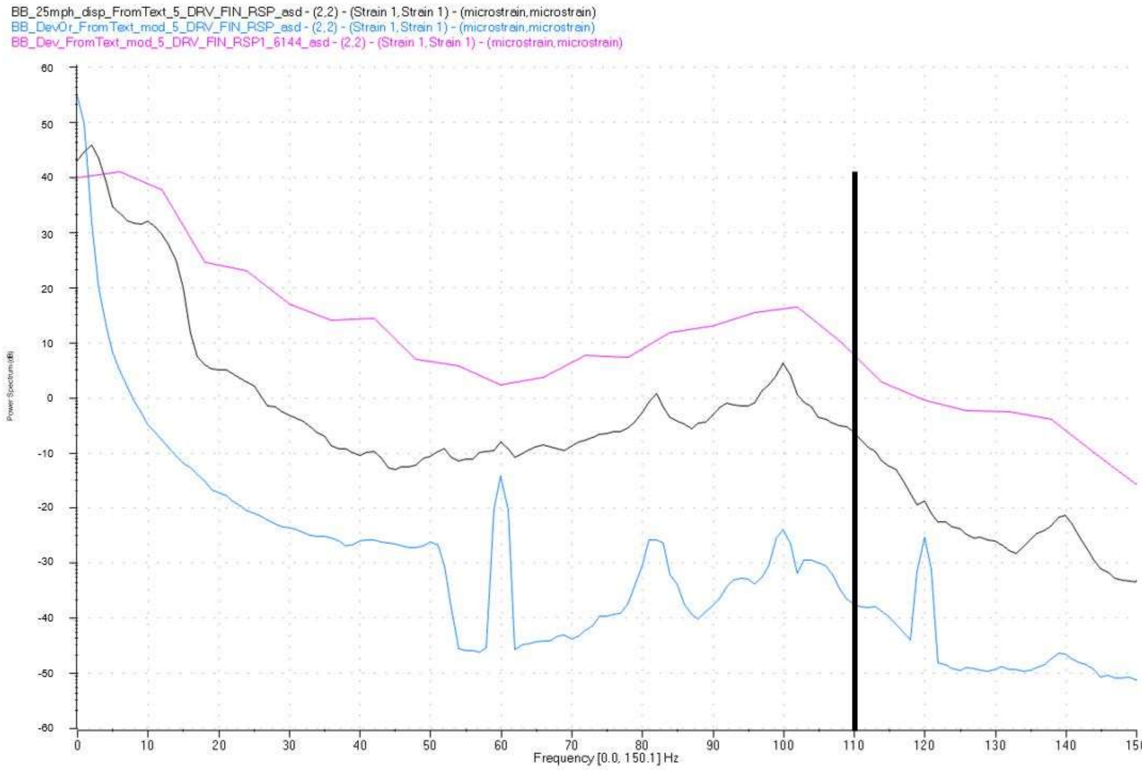


Figure 6.43 PSD of evaluated signals for Belgian block excitation

As the test progresses, the testing apparatus records the microstrain at the location of expected failure. It is expected that the microstrain will increase substantially just before failure of the specimen due to material softening from excessive repeated loading. Figure 6.44 shows the measured microstrain on the HMMVW suspension spring during a period of 2 seconds after 5 minutes, 1 hour, 2 hours and 2.5 hours from the start of the durability test. As expected, the microstrain pattern follows that of the excitation displacement according to a static behavior. However, as time progresses (see the zoom in version of Figure 6.45) the average microstrain increases (e.g. from the pink line of 2 hours of operation to the green line of 2.5 hours of operation) softening the material before the inevitable failure.

Figure 6.46 shows the measured microstrain for almost a second before failure at **2.66 hours** or 2 hours, 39 minutes and 36 seconds (pink line). At that instant, the material has softened considerably, the microstrain has increased substantially without following the static assumption anymore, and failure occurred (see Figure 6.46). To validate this result, the test was repeated with a different coil of the same material and failure was imminent at approximately 2.7 hours before the load cell on the test equipment failed and the test was terminated.

The failure at 2.66 hours compares very favorably with the expected failure of 2.85 hours for the SAE 1038 (not hardened steel) material.

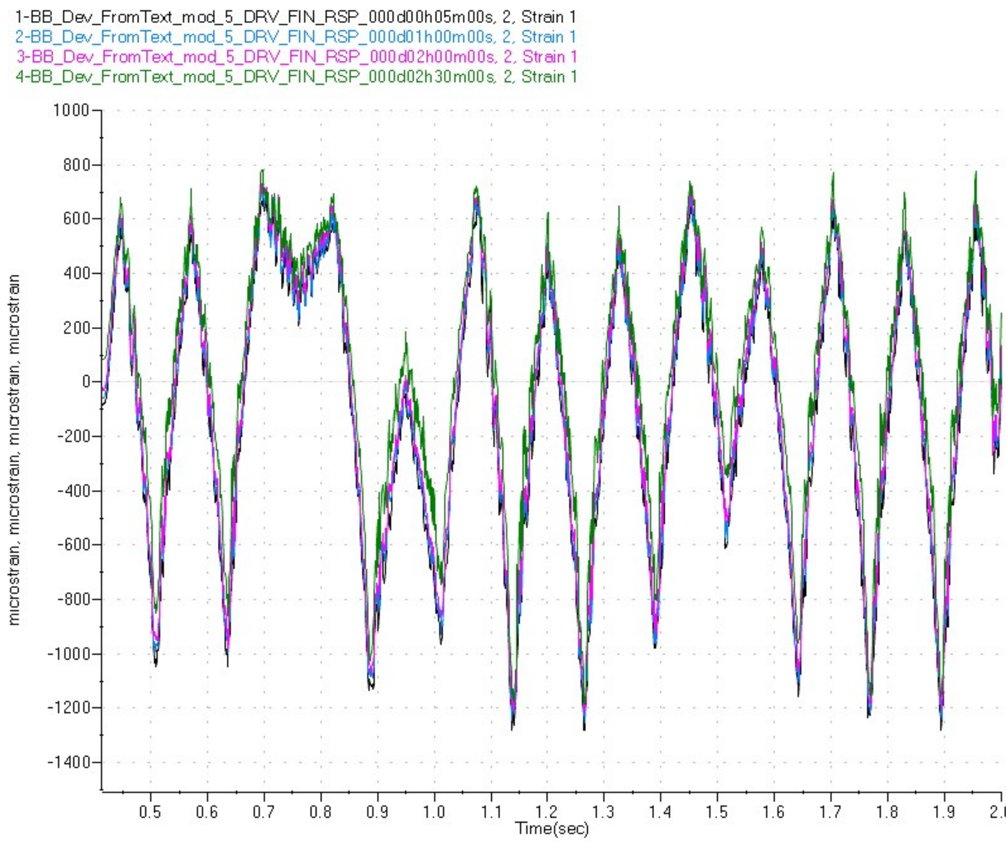


Figure 6.44 Measured microstrain after 5 minutes, 1 hour, 2 hours and 2:30 hours

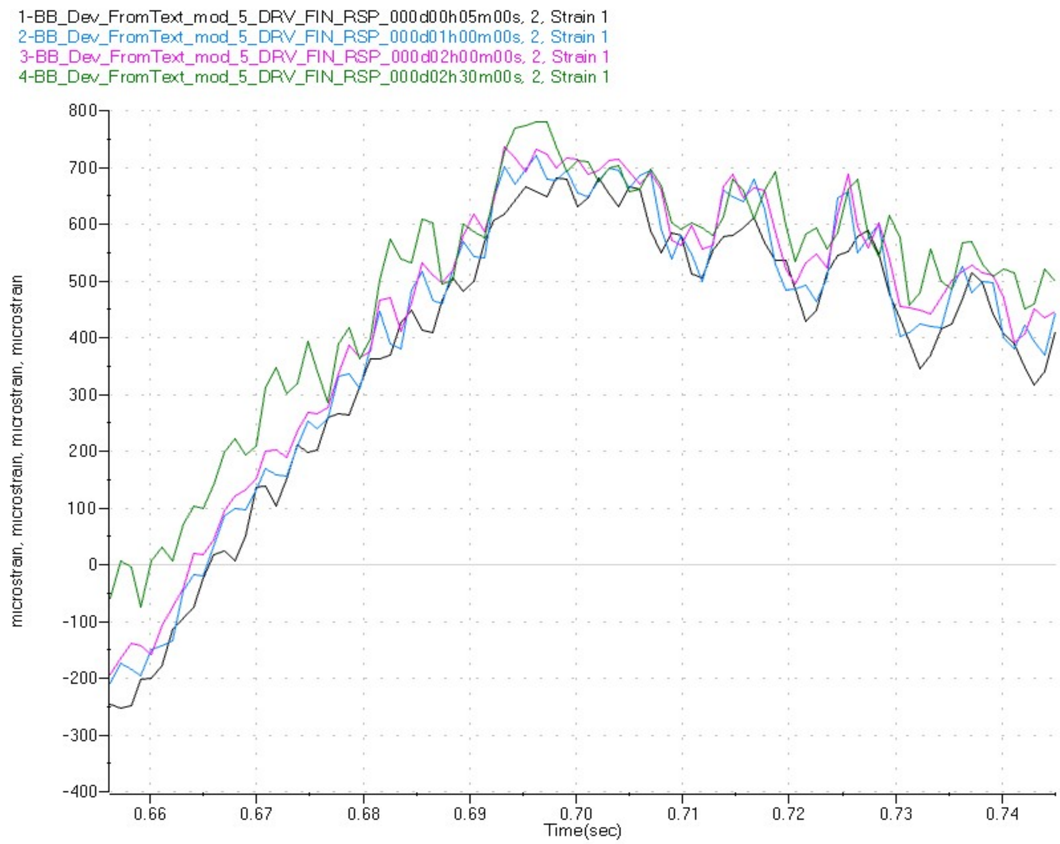


Figure 6.45 Zoom in of measured microstrain after 5 minutes, 1 hour, 2 hours and 2:30 hours

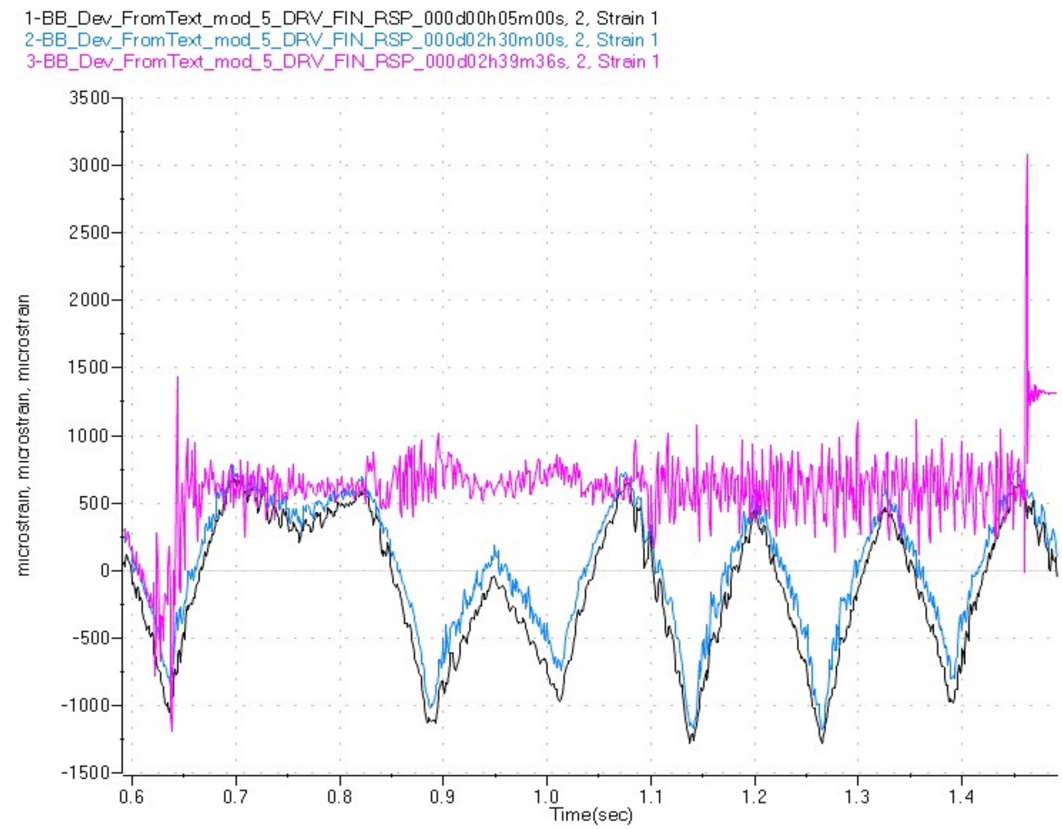


Figure 6.46 Measured microstrain after 5 minutes, 1 hour, 2:30 hours, and 2:39:36 hours

Figure 6.47 Specimen after failure

# CHAPTER SEVEN

# CONTRIBUTIONS AND FUTURE WORK

## 7.1 Dissertation Contributions

There are two main contributions in this dissertation. The first one is the development of a new durability test method with a much shorter duration compared to the current state-of-the-art method. It is based on computing the fatigue damage of each individual fatigue cycle in the signal and keeping only the dominant cycles contributing ninety percent of the overall damage. The number of the dominant cycles is a very small percentage of the overall number. Then, the proposed method forms a synthetic signal composed only of the dominant cycles reducing therefore, the duration of the durability test. At the same time, the synthetic signal is much easier to reproduce on the testing equipment reducing the test preparation time and improving the reliability of results.

The second main contribution is the experimental validation of the proposed durability test method using the state-of-the-art durability equipment of the US Army's Ground Vehicle Systems Center (GVSC).

The developed approach has wide practical applications in structural reliability, accelerated life testing, design for lifecycle cost, preventive maintenance strategies and fatigue reliability, among others.

## 7.2 Recommendations for Future Work

1. Expand the proposed approach for vibratory (not static) problems where the input displacement signal and the output stress signal are not scaled linearly (i.e. the output stress signal cannot be obtained by multiplying the input displacement

signal by a scalar). A possible approach is to develop a nonlinear transformation between the excitation displacement signal and the output stress signal using advanced neural networks and a Nonlinear Auto-Regressive model with Exogenous inputs (NARX). The latter has excellent capabilities in providing an accurate metamodel of time-dependent functions (signals).

2. Develop a fatigue “hot spot” analysis to determine the location on the specimen with the highest propensity for fatigue failure. The current approach assumes that the specimen will fail at a known location.
3. Use the proposed durability method to develop a new accelerated testing method to account for the uncertainty and variability in fatigue life prediction from various sources such as fatigue model, material properties, and numerical issues due to discretization and assumed finite duration of signals.

REFERENCES


1. http://www.matweb.com/

2. https://www.bts.gov/content/us-vehicle-miles

3. Albert, W. A. J., 1837, “Uber Treibseile am Harz. Archiv ffir Mineralogie, Georgnosie”, Bergbau und Hiittenkunde 10, 215-234.

4. Rankine, W. J. M., 1842, On the causes of the unexpected breakage of the journals of railway axles, and on the means of preventing such accidents by observing the law of continuity in their construction, Institution of Civil Engineers, Minutes of Proceedings, London, Vol. 2, pp. 105-108.

5. Morin, A., 1853, “Lemons de mecanique practique---resistance des materiaux”, Librairie de L. Hachette et Cie, Paris, p. 456.

6. Braithwaite, F., 1854, On the fatigue and consequent fracture of metals, Institution of Civil Engineers, Minutes of Proceedings, London, Vol. XlI1, pp. 463-474.

7. Wohler, A., 1860, “Versuche zur Ermittlung der auf die Eisenbahnwagenachsen einwirkenden Kr/i.fte und die Widerstandsf'~ihigkeit der Wagen”, Zeitschrift fiir Bauwesen. Acheen, X, 583-616.

8. Schultz, W., 1996, “A History of Fatigue”, *Engineering Fracture Mechanics*, 54(2), pp. 263-300.

9. Palmgren, A., 1924, “Die Lebensdauer von Kugellagern”, VDI-Zeitschrift 68, 339-341.

10. Basquin, O., H., 1901, “The exponential law of endurance tests”, *Proc. Annual Meeting, American Society for Testing Materials*, 10, pp. 625-630.

11. Ewing, J. A., Humfrey, J. C. W., 1903, “The fracture of metals under repeated alternations of stress”, *Phil. Trans. Royal Society*, London, Vol. CC, pp. 241 - 250.

12. Polanyi, 1943, Zeitschriftfiir Physik 89, 660.

13. Orowan, E., 1939, “Theory of the fatigue of metals” *Proc. Royal Society*, Set. A, Vol. 171, pp. 79-105.

14. Heyn, E. E., 1914, “Die kerbwirkung und ihre bedeutung ffir den konstrukteur”, ZVDI 58, 383-391 (1914).

15. Langer, B. F., 1937, “Fatigue failure from stress cycles of varying amplitude”, *Trans. ASME J. Appl. Mech.*, 59, A160-A162.

16. Serensen, S. V., 1940, “Theory of strength under variable loading”, Akademici Nauk Ukrainskoc, SSR, Stahl und Eisen 60, 285.

17. Miner, M. A., 1945, “Cumulative damage in fatigue” *Trans. ASME J. Appl. Mech.*, 12, AI59-A164.

18. Matsuishi, M., Endo, T., 1968, “Fatigue of metals subjected to varying stress”, Presented to Kyushu District Meeting, Jap. Soc. Mech. Engineering.

19. DeJonge, J., B., 1969, “Fatigue load monitoring of tactical aircraft”, NLR Report TR 69 0330.

20. Weibull, W., 1939, “A Statistical Theory of the Strength of Materials”, Ingeniers Vetenskaps Akademiens Handlingar, No. 151, Generalstabens Litografisky Anstalts Ferlag, Stockholm.

21. Gasner, E., 1941, “Auswirkung betriebsfihnlicher Belastungsfolgen auf die Festigkeit von Flugzeugbauteilen”, Kurzfassung der Dissertation gleichen Titels. Jahrbuch 1941 der deutschen, Luftfahrtforschung, S. 1472-1483.

22. Coffin, L. F., 1954, “A study of the effects of cyclic thermal stresses in ductile metals”, *Trans ASME*, 76, 931–950.

23. Manson, S. S., 1960, “Thermal stresses in design”, Cyclic Life of Ductile Materials, Pt. 19, pp. 139–144

24. Neuber, H., 1946, “Theory of notch stress”, Ann Arbor, MI: J. W. Edwards.

25. Topper, T. H., Wtzel, R. M. and Morrow J, 1969, “Neuber’s rule applied to fatigue of notch specimens”, *Journal of Materials*, 4(1), 200-209.

26. Molsky, K and Glinka, G., 1981, “A method for elastic-plastic stress and strain calculation at a notch root”, *Materials Science and Engineering*, 50, 93-100.

27. Smith, R. N., Watson, P. P., and Topper, T. H., 1970, “A stress-strain function for the fatigue of metals”, *Journal of Materials*, 5(4), pp. 767-778

28. Liu, K. C., 1993, “A method based on virtual strain-energy parameters for multiaxial fatigue life prediction,” *Advances in Multiaxial Fatigue*, ASTM STP 1191, pp. 67-84.

29. Bannantine, J. A. and Socie, D. F., 1991a, “A variable amplitude multiaxial fatigue life prediction model”, Fatigue under Biaxial and Multiaxial Loading, European Structural Integrity Society, ESIS Publication 10, Mechanical Engineering Publications, London, pp. 35-51.

30. Dang Van, K., 2003, "Unified Fatigue Modeling for Structural Applications Based on a Multiscale Approach and Shakedown Hypothesis," Workshop: Optimal Design, Laboratorie de Mecanique des Solides Ecole Polytechnique Palaiseau, France, November 26-28, 2003.

31. Erker, A., 1958, "Sicherheit und Bruchwahrscheinlichkeit", MAN-Forschungsheft.

32. Head, A. K. and Hooke, F. H, 1956, "Fatigue of metals under random loads", *Nature*, London, Volume 177, no. 4521, pp. 1176-1177

33. Sankararaman, S., Ling, Y., Mahadevan, S., 2011, "Uncertainty quantification and model validation of fatigue crack growth prediction", *Engineering Fracture Mechanics*, 78(7), pp. 1487-1504.

34. Ling, Y., Shantz, C., Mahadevan, S., Sankararaman, S., 2011, "Stochastic prediction of fatigue loading using real-time monitoring data", *International Journal of Fatigue*, 33(7), pp. 868-879.

35. Hu Z., Mahadevan S., 2015, "Accelerated Life Testing (ALT) Design Based on Computational Reliability Analysis", *Quality and Reliability Engineering International,*32(7), 2217-2232.

36. Zhang R, Mahadevan G., 2001, "Integration of computation and testing for reliability estimation", *Reliability Engineering & System Safety,* 74(1), 13-21.

37. Van Dorp, J.R., and Mazzuchi, T.A., 2004, "A General Bayes Exponential Inference Model for Accelerated Life Testing," *Journal of Statistical Planning and Inference*, 119(1), 55–74.

38. Van Dorp, J.R., and Mazzuchi, T.A., 2005, "A General Bayes Weibull Inference Model for Accelerated Life Testing, *Reliability Engineering & System Safety*, 90(2), 140–147.

39. Elsayed, E.A., and Zhang, H., 2007, "Design of PH-based Accelerated Life Testing Plans Under Multiple Stress Types, *Reliability Engineering & System Safety*, 92(3), 286–292.

40. Zhang, Y, and Meeker, W.Q., 2006, "Bayesian Methods for Planning Accelerated Life Tests, *Technometrics*, 48(1), 49–60.

41. Lee, J., and Pan, R., 2010, "Analyzing Step-Stress Accelerated Life Testing Data Using Generalized Linear Models", *IIE Transactions*, 42(8), 589–598.

42. Voiculescu, S. et al., 2009, "Bayesian Estimation in Accelerated Life Testing," *International Journal of Product Development*, 7(3), 246–260.

43. Lee, Y.-L., Barkey, M. E., Kang, H.T., 2011, *Metal Fatigue Analysis Handbook,* Elsevier, Oxford

44. Masing, G., 1926, "Self-stretching and hardening for brass", *Proc. 2nd Int. Cong. Applied Mechanics*, pp. 332-335

45. Chiang, D.-Y., 1999, "The Generalized Masing Models for Deteriorating Hysteresis and cyclic Plasticity", *Applied Mathematical Modeling,* Elsevier, Oxford, Volume 23, Issue 11, pp. 847-863.

46. Bauschinger, J., 1886, "On the change of position of the elastic limit of iron and steel under cyclic variations of stress", *Mitt. Mech. Tech. Lab*, Munchen, 13, pp. 1-115.

47. Ramberg, W., Osgood, W. R., 1943, "Description of stress–strain curves by three parameters", *Technical Note No. 902*, Washington DC, National Advisory Committee for Aeronautics.

48. Basquin, O. H., 1910, "The exponential law of endurance tests", *Proceedings of American Society for Testing and Materials*, 10, 625-630.

49. Manson, S. S., 1960, "Thermal stresses in design", *Cyclic Life of Ductile Materials*, Pt. 19, pp. 139–144.

50. Coffin, L. F., 1954, "A study of the effects of cyclic thermal stresses in ductile metals", *Trans. ASME*, 76, 931–950.

51. Morrow J.D., 1964, "Cyclic plastic strain energy and fatigue of metals. Internal friction, damping, and cyclic plasticity", *American Society for Testing and Materials*, Philadelphia (PA), ASTM STP 37845–87.

52. Socie, D. F., 1987, "Multiaxial fatigue damage models", *Trans. ASME, J. Eng. Mater. Technol.*, 109, 293–298 (1987).

53. Hua, C. T., Socie, D. F., 1984, "Fatigue damage in 1045 steel under constant amplitude biaxial loading", *Fatigue & Fracture of Engineering Materials & Structures*, 7: 165–179.

54. Bannantine, J. A. and Socie, D. F., 1991a, "A variable amplitude multiaxial fatigue life prediction model," *Fatigue under Biaxial and Multiaxial Loading, European Structural Integrity Society*, ESIS Publication 10, Mechanical Engineering Publications, London, pp. 35-51.

55. Bannantine, J. A. and Socie, D. F., 1991b, "Multiaxial fatigue life estimation technique," in: M. Mitchel and R. Landgraf (Eds), *ASTM Symposium on Advances in Fatigue Lifetime Predictive Techniques*, ASTM STP 1122, pp. 249-275.

56. Fatemi, A. and Socie, D. F., 1988, “A critical plane approach to multiaxial fatigue damage including out of phase loading,” *Fatigue Fract. Eng. Mater. Struct.*, 11, 149–165.

57. Liu, K. C., 1993, “A method based on virtual strain-energy parameters for multiaxial fatigue life prediction”, *Advances in Multiaxial Fatigue*, ASTM STP 1191, pp. 67-84.

58. Smith, R. N., Watson, P. P., Topper, T. H., 1970, “A stress-strain function for the fatigue of metals”, *Journal of Materials*, 5(4), pp. 767-778.

59. Findley, W. N., 1959, “A Theory for the Effect of Mean Stress on Fatigue of Metals Under Combined Torsion and Axial Load or Bending”, *ASME J. Eng. Ind*., pp. 301-306.

60. Wirsching, P. H., Paez, T. L., and Ortiz, H., 1995, *Random Vibrations: Theory and Practice*, John Wiley & Sons, New York, NY.

61. Madsen, H.O, Krenk, S. and Lind, N.C., 2006, *Methods of Structural Safety*, Dover Publications.

62. Singh, A., Mourelatos, Z. P., and Li, J., “Design for Lifecycle Cost using Time-dependent Reliability,” *ASME Journal of Mechanical Design*, 132(9), 091008 (11 pages), 2010.

63. Lee, Y.L, Pan, J., Hathaway, R., and Barkey, M., *Fatigue Testing and Analysis: Theory and Practice,* Elsevier Butterworth-Heinemann, 2005.

64. Brudnak, M., Walsh, J., Baseski, I., and LaRose, B., 2017, “Durability Test Time Reduction Methods”, *SAE International Journal of Commercial Vehicles*, 10(1), p. 113-121.

65. Anon., 2006, “Test and Evaluation Policy,” AR 73-1, Department of the Army, Washington, DC.

66. Anon., 2011, “Department of Defense Handbook: Reliability Growth Management,” MIL-HDBK-189C, U.S. Army Materiel System Analysis Activity (AMSAA), Aberdeen, MD.

67. Brudnak, M. and Pozolo, M., 1999, "Using Modeling and Simulation for Failure Analysis," *SAE Technical Paper 1999-01-0605*, doi:10.4271/1999-01-0605.

68. Brudnak, M., 2005, “Support Vector Methods for the Control of Unknown Nonlinear Systems,” Doctoral Dissertation, Oakland University, Rochester, MI, doi:10.13140/RG.2.1.4942.5364.

69. Brudnak, M., 2005, "A Composite Linear and Nonlinear Approach to Full-Vehicle Simulator Control," *SAE Technical Paper 2005-01-0937*, doi:10.4271/2005-01-0937.

70. Zywiol, H.J.Jr.; Brudnak, M.J., 1994, “M149A2/Pintle Motion Base Simulator Validation Final Report”, No. 13622, U.S. Army Tank-Automotive Command, Warren, MI.

71. Zywiol, H., Brudnak, M., and Beck, R., 1995, "Physical Simulation Trailer Testing," *SAE Technical Paper 950414*, doi:10.4271/950414.

72. Cripe, R., 1972, "Making A Road Simulator Simulate," *SAE Technical Paper 720095*, doi:10.4271/720095.

73. Cryer, B., Nawrocki, P., and Lund, R., 1976 "A Road Simulation System for Heavy Duty Vehicles," *SAE Technical Paper 760361*, doi:10.4271/760361.

74. Fash, J., Goode, J., and Brown, R., 1992, "Advanced Simulation Testing Capabilities," *SAE Technical Paper 921066*, doi:10.4271/921066.

75. Leese, G. and Mullin, R., 1991, "The Role of Fatigue Analysis in the Vehicle Test Simulation Laboratory," *SAE Technical Paper 910166*, doi:10.4271/910166.

76. Lund, R. and Donaldson, K., 1982, "Approaches to Vehicle Dynamics and Durability Testing," *SAE Technical Paper 820092*, doi:10.4271/820092.

77. Madden, M., 1970, "Road Simulator Testing of Large Vehicles," *SAE Technical Paper 700455*, doi:10.4271/700455.

78. Nolan, S. and Linden, N., 1987, "Integrating Simulation Technology into Automotive Design Evaluation and Validation Processes," *SAE Technical Paper 871941*, doi:10.4271/871941.

79. White, K.J., 1985, “The Road Simulator – A Practical Laboratory Approach,” Prediction and Simulation of In-Service Environments, I. Mech. E., London.

80. Ledesma, R., Jenaway, L., Wang, Y., and Shih, S., 2005, "Development of Accelerated Durability Tests for Commercial Vehicle Suspension Components," *SAE Technical Paper 2005-01-3565*, doi:10.4271/2005-01-3565.

81. Reubush, D., Paone, J., and Walsh, J., 2005, "Simulation Test Methodology for the Jeep® Grand Cherokee Dynamic Handling System," *SAE Technical Paper 2005-01-1496*, doi:10.4271/2005-01-1496.

82. Ashmore, S.C., Piersol, A.G., Witte, J.J., 1992, “Accelerated Service Life Testing of Automotive Vehicles on a Test Course,” *Vehicle System Dynamics*, 21, pp. 89–108, doi:10.1080/00423119208969004.

83. Lin, K-Y, Hwang, J-R, Chang, J-M, 2010, “Accelerated durability assessment of motorcycle components in real-time simulation testing,” *Proceedings of the Institution of Mechanical Engineers, Part D: Journal of Automobile Engineering*, 224(2245–259), doi:10 .1243/09544070JAUTO1059.

84. Madane, V., Swami, A., Shah, M., and Sane, S., 2013, "Creation and Evaluation of Mini-Truck Accelerated Endurance Test Cycle," *SAE Technical Paper 2013-26-0154*, doi:10.4271/2013-26-0154.

85. Mattettia, M., Molaria, G., Vertuab, A., 2015, “New Methodology for Accelerating the Four-post Testing of Tractors Using Wheel Hub Displacements,” *Biosystems Engineering*, Elsevier, 129, p. 307–314.

86. Anon., 2011, “Standard Practices for Cycle Counting in Fatigue Analysis,” E1049-85 (Reapproved 2011), ASTM, West Conshohocken, PA.

87. Anon., 2016, “RPC® File Formats, Reference Manual,” https://www.mts.com/cs/groups/public/documents/library/mts_007569.pdf, MTS Systems Corporation, Eden Prairie, MN.

RELATED PUBLICATIONS

**Journal Papers**


1. Tsianika, V., Geroulas, V., Mourelatos, Z. P., and Baseski, P., 2017, "A Methodology for Fatigue Life Estimation of Linear Vibratory Systems under Non-Gaussian Loads", *2017 SAE Journal of Materials and Manufacturing,* 2017-01-0197, 2017.

2. Brudnak, M., Walsh, J., Baseski, I., and LaRose, B., 2017, "Durability Test Time Reduction Methods", *SAE International Journal of Commercial Vehicles*, 10(1), p. 113-121.

3. Moustafa, K., Hu, Z., Mourelatos, Z. P., Baseski, I., and Majcher, M., 2020, "Resource Allocation for System Reliability Analysis using Accelerated Life Testing," *ASME Journal of Mechanical Design*, 142(3), 031119 (15 pages), 2020. Also, *Proceedings ASME 2019 Design Engineering Technical Conferences*, Paper DETC2019-97616, Anaheim, CA, Aug. 18-21, 2019.


**Conference Papers**


1. K. Moustafa, Z. Hu, Z.P. Mourelatos, I. Baseski, and M. Majcher, "Multi-level Accelerated Life Tests for System Reliability Analysis Using Extended Hazard Models with Shared Frailty," AIAA SciTech Forum, 2021.